Investigation into Rotor Blade Aerodynamics

Analysis of the stationary measurements on the UAE phase-VI rotor in the NASA-Ames wind tunnel

C. Lindenburg

Preface

In the spring of 2000 NREL has been testing their 10m test turbine in the 24m x 36m wind tunnel of NASA-Ames. This test turbine was referred to as "Unsteady Aerodynamics Experiment" phase-VI. In the fall of 2000 a 'Blind Comparison' was organised by NREL in which wind turbine research institutes worldwide were invited to calculate some of the stationary operational conditions without knowing the measured results. Partly based on the scatter in the calculated aerodynamic loads, further research was started within the scope of the IEA Annex-XX project. This report contains well-defined reference data and calculations such that it can serve as basis for future investigations in the IEA Annex-XX project.

The work reported here was supported by the Netherlands Society for Energy and the Environment, NOVEM. Contract number 0224-01-57-21-0018, ECN project number 74112.

Publication of this report was completed within the IEA Annex-XX project, ECN number 74189.

Acknowledgement

The author wants to thank Mr Scott Schreck of the National Renewable Energy Laboratory for providing the opportunity to carry-out part of the work at NREL, and for providing the data measured in the NASA-Ames wind tunnel.

The author wants to thank Mr James L. Tangler of NREL for providing results from the LSWT code, and Mr Jeppe Johansen of Risø for providing results calculated with the EllipSys3D code. These data allowed comparison of the rotating aerodynamic coefficients.

Abstract

During 2000 NREL (Colorado) performed an exhaustive series of measurements on their UAE phase-VI wind turbine in the 24m x 36m wind tunnel of NASA-Ames (California). In the fall of 2000 NREL organised a 'Blind Comparison' for wind-turbine research institutes. ECN participated in this benchmark with the program PHATAS. The stationary aerodynamic coefficients calculated by the participants of this 'Blind Comparison' showed large differences, in particular in stall. Based on the aerodynamic models used in the different design codes it was concluded that these differences depend among others on the airfoil coefficients-tables used and on the correction models used for rotational effects.

In the winter of 2002 the aerodynamic coefficients in stall were investigated in more detail, partly based on the measured data for the S809 airfoil. These investigations resulted in an improved model for the coefficients in stall, and in suggestions for improving the models for rotational augmentation. In the program PHATAS the implementation of e.g. the tip loss factor was improved for large distances between the trailing vortices. At the moment of finishing this work, still some discrepancies remain between the measured and the calculated properties in stall. An onset is given for further research (starting with code-comparison) within the IEA Annex-XX project.

Based on the discrepancies between the predicted and the calculated aerodynamic properties the needs for future developments on the existing wind turbine design codes were described.

Keywords

Airfoil coefficients, Deep stall, Rotational augmentation,
Rotor aerodynamics, Tip-loss models, Wind turbine.

CONTENTS

LIST OF SYMBOLS

AR		Aspect ratio of a flat plate or a rotor blade: $AR = R^2/Area$.
B		Number of rotor blades.
c	[m]	Blade chord.
$c_\mathrm{l}, c_\mathrm{d}, c_\mathrm{m}$		Dimensionless coefficients for aerodynamic lift, drag, and pitching moment (nose-up) of the airfoils.
$c_\mathrm{n}, c_\mathrm{t}$		Dimensionless coefficients for normal and tangential aerodynamic force.
D	[m]	Diameter of a cylinder.
e_root	[m]	Spanwise location of the blade root, along the coned blade axis.
F		'Tip-loss factor' for the average induced flow between vortex sheets.
f_flap, f_lead	[N/m]	Aerodynamic force distribution in flap- and lead direction.
f_l, f_d	[N/m]	Aerodynamic lift and drag loading per unit span.
f_n, f_t	[N/m]	Aerodynamic normal and tangential loading per unit span.
J_gen	[kgm^2]	Inertia of the generator and the parts aft of the flexible shaft.
J_hub	[kgm^2]	Hub-inertia, including the drive train parts in front of the flexible shaft.
k_sh	[Nm/rad]	Torsional stiffness of the rotor shaft.
L	[m]	Total length of the blade, measured along its (curved!) axis.
$M_\mathrm{x}, M_\mathrm{y}, M_\mathrm{z}$	[Nm]	Blade leadwise, flapwise, and torsional moment.
m_aero	[Nm/m]	Aerodynamic moment, nose-up positive.
$m(\mathrm{s})$	[kg/m]	Spanwise blade mass distribution.
N		Number of blade elements, used in Appendix B.
Q_gen	[Nm]	Generator torque, expressed with respect to the rotor shaft.
R	[m]	Rotor radius, or radial co-ordinate of the tip.
r	[m]	Radial co-ordinate in the rotor system.
S		Strouhal number: $S = \nu\, D/V$.
s	[m]	Spanwise co-ordinate along the blade axis.
t	[s]	Time.
U_i, V_i	[m/s]	Axial and tangential induced velocity at the location of the blade.
$\bar{U}_\mathrm{i.an}$, $\bar{V}_\mathrm{i.an}$	[m/s]	Annulus-average axial and tangential induced velocity.
U_tr	[m/s]	Transport velocity: $U_\mathrm{tr} = \sqrt{(U_\mathrm{wind}\,\cos\chi - F\,U_\mathrm{i})^2 + (U_\mathrm{wind}\,\sin\chi)^2}$.
U_wind	[m/s]	Undisturbed wind velocity.
V_eff	[m/s]	Effective wind velocity on a blade section, perpendicular to its axis.
x, y, z	[m]	Flapwise (downwind), lagwise, and spanwise co-ordinates (see G.Ll.).
$x_\mathrm{ac}, y_\mathrm{ac}$	[m]	Flatwise (x) and chordwise (y) location of the aerodynamic centre.
α	[rad]	Aerodynamic angle-of-attack.
α_c	[rad]	Cone angle of the rotor blades.
χ	[rad]	Misalignment angle of the wind w.r.t. the normal on the rotor plane.
ϕ_inf	[rad]	Inflow angle of the airflow on the blade w.r.t. the rotor plane.
ϕ_z	[rad]	Elastic torsional deformation of a blade section, nose-down positive.
λ		Tip speed ratio: $\lambda = \Omega \cdot R \cdot \cos(\alpha_\mathrm{c})/U_\mathrm{wind}$.
ν	[rad/s]	Frequency.
π		Trigonometric constant: $\pi = 3.1415926536$ (= value in the code).
ρ	[kg/m^3]	Air density.
σ		Solidity of an annulus: $\sigma = (B\,c)/(2\,\pi\,r)$.
θ_eff	[rad]	Sum of blade twist, pitch and elastic torsion: $\theta_\mathrm{eff} = \theta_\mathrm{tw} + \theta_\mathrm{p} - \phi_\mathrm{z}$.
θ_p	[rad]	Blade pitch angle.
θ_tw	[rad]	Blade twist angle.
τ	[s]	Time constant in the generator torque-speed relation.
Ω	[rad/s]	Rotor speed, positive for clockwise rotation.

1. INTRODUCTION

In April 2000, the 2-bladed UAE phase-VI test turbine of NREL was placed in the 24m x 36m wind tunnel of NASA Ames in California, U.S.A., see Figure 1.1. Measurements have been performed for a period of three weeks. Because of their reproducibility, the measurements were found to be of high quality. On the basis of these measurements, NREL organised a 'Blind Comparison' in the fall of 2000. For this Blind Comparison wind turbine research institutes worldwide were asked to calculate the response for 20 conditions, without knowledge of the measured results. The 10.058m diameter UAE phase-VI rotor blades have the 20.95% thick S809 airfoils, of which a description is given in appendix A. The blades are twisted and have a linear taper with an aspect ratio of 7.2 which is less than half the value for modern large wind turbines. For the 2-bladed rotor, this gives an aerodynamic solidity of 5.8%. The UAE turbine can be used upwind as well as downwind, and was mainly operated at 72rpm. For most of the measurements that were that were done, the rotor-average axial induction factor was 0.12 or smaller, which is a result from the relatively small tip-speed ratios, see also chapter 6. Together with the small ratio between rotor swept-area and tunnel cross-section (0.09) this low axial induction factor gives a blockage (restrained wake expansion) of less than 1%.

This document reports on the results from the NOVEM project '*NASA-Ames Rotorblad Aerodynamica*', contract number 224.721.0013. This project included participation in the 'Blind Comparison' organised by NREL in the fall of 2000, see also chapter 6, and exploration of the measurements in order to improve the knowledge of wind turbine aerodynamics. The resulting knowledge was implemented in the existing design tools at ECN based on BEM theory.

Within the IEA framework project 'Annex-XX' further investigations were planned into the measurements in the NASA-Ames wind tunnel. Anticipating on this work, special effort is paid to the description of the UAE phase-VI rotor, the assessment of the S809 airfoil coefficients and the development of the analysis tool *inflow*.

Approach

To deal with the large amount of aspects of aerodynamics of wind turbine rotors, the investigations started with the assessment of the stationary aerodynamic coefficients of the S809 airfoil. Next the effects of rotation were investigated after which the implementation within the BEM-based design codes (such as BLADMODE and PHATAS) were investigated.

During the work within this project, the joint European IEA Annex-XX framework project was formulated on basis of the NASA-Ames measurements. Because the 'Blind Comparison' showed a large discrepancy between the analysis methods, and also because the IEA Annex-XX work would be performed some years later and over a longer period, the investigations in the underlying NOVEM project were focussed more on the fundamental aspects of the stationary aerodynamic coefficients of the S809 airfoil, and on an accurate model description of the UAE phase-VI rotor. It was anticipated that the topics related with instationary blade loading associated with oblique inflow will be subject of the investigations within the IEA Annex-XX framework roject.

Dominant aerodynamic aspects of rotor blades are the effects of rotation. Several models (mainly empirical) have been developed for the estimation of rotating aerodynamic coefficients. Because most of these models are formulated as correction on the non-rotating aerodynamic coefficients, and because for most airfoils the aerodynamic coefficients are measured up to angles-of-attack of about 20deg, the investigations started with an improvement of the empirical model for dynamic stall, implemented in the program *StC* , see chapter 2. Emphasis was laid on the influence of the finite span and on the tangential (suction-) force coefficients. The tool *StC* can be used to extend tables with 2D coefficients to the angle-of-attack range from -180deg to 180deg.

Next the aerodynamic characteristics of the S809 airfoil were investigated, starting with the non-rotating coefficients. These investigations include publications of numerical analyses, publications of 2D coefficients from wind tunnel tests and analyses of the non-rotating measurements in the NASA-Ames windtunnel, see chapter 3. For the latter analyses, the program '*inflow*' was developed to obtain the distribution of angle-of-attack, see Appendix B.

After assessing the non-rotating aerodynamic properties of the UAE phase-VI rotor blades, an investigation was done into the influence of rotational effects ('Himmelskamp effect', or centrifugal pumping effect) see chapter 4. This investigation started with a short historical overview of former work, trying to give some clarity on the rotational effects (while making a distinction between laminar separation bubbles, leading edge stall, and trailing edge stall). Chapter 4 also contains a description of 3 different kind of correction models, where it must be noted that the '3D-correction' method of Snel et al. [71] was slightly modified/improved. Finally the aerodynamic coefficients predicted with these models were compared with the blade loads of the rotating measurements in the NASA-Ames windtunnel. Most of the empirical models predict an enhanced aerodynamic lift, although none of these models fit with all conditions that have been measured.

Chapter 5 contains descriptions some aspects of the BEM approach, with emphasis on the effects of oblique inflow and the formulation and implementation of the so-called 'tip loss factor'. Together with the modified '3D-correction' method described in chapter 4 these new insights in the BEM approach were implemented in the codes BLADMODE release "APR-2002" [45] and PHATAS release "OCT-2002" [46, 47]. In the remainder of this report these versions will simply be referred to as BLADMODE and PHATAS.

The results of the ECN-participation in the 'Blind Comparison' in the fall of 2000 together with an evaluation of the improved BEM-based codes BLADMODE and PHATAS are reported in chapter 6. The measurements used in the 'Blind Comparison' were all for a pitch angle of 3deg, a rotor speed of about 72rpm, and wind speed values of 7m/s through 25m/s. For a wind speed of 15m/s and a rotor speed of 72rpm, the tip speed ratio is 2.53. As a consequence of the low tip speed ratio the rotor is nearly always in stall for pitch angles near 3deg, except at low wind and/or strong misalignment. This small tip-speed ratio gives a relative low rotor disk loading, despite the somewhat high aerodynamic solidity. The evaluation of the improved programs BLADMODE and PHATAS focussed on the non-yawed stationary upwind conditions and included sensitivity studies into the different 'correction' models for the rotational effects, and into numerical aspects. As reference for investigations by other IEA Annex-XX participants, the stationary aerodynamic rotor characteristics calculated with the improved PHATAS release "OCT-2002" are included.

The conclusions resulting from the work reported in the chapters 2 through 6 are written in chapter 7. Although a lot of questions still remain, the aerodynamic modelling of design tools BLADMODE and PHATAS has been improved. Based on the insight and remaining questions, some recommendations for future investigations (such as in Annex-XX) are given. Also a proposal is given of a rotor aerodynamics model with the models that are needed to improve the current wind turbine design programs.

Appendix A contains a description of the 2-bladed UAE phase-VI turbine as was relevant for modelling in the ECN codes PHATAS [46] and in BLADMODE [45]. To form a basis of reference for the work within the IEA Annex-XX project, appendix A also contains the S809 airfoil coefficients used for the analyses with PHATAS and the stationary aerodynamic characteristics of the UAE phase-VI rotor calculated with PHATAS for some idealised conditions.

Appendix B contains a description of the analysis tool '*inflow*' which was developed to obtained the tables with aerodynamic coefficients on basis of the measured blade-load distribution. In the tool *inflow* the influence of the induced velocity in the rotor wake was solved with a vortex-description. The influence of the induced velocity on the wake structure was partly included.

Effort was spent on the proper functioning and validation of this tool *inflow* because it was foreseen that it may/will also be used in the following IEA Annex-XX work or in the E.C. project MEXICO. For comparison and evaluation of the results obtained with *inflow*, a similar tool *beminf* was developed on basis of the BEM theory, including an option to account for the tip-losses by the Prandtl factor.

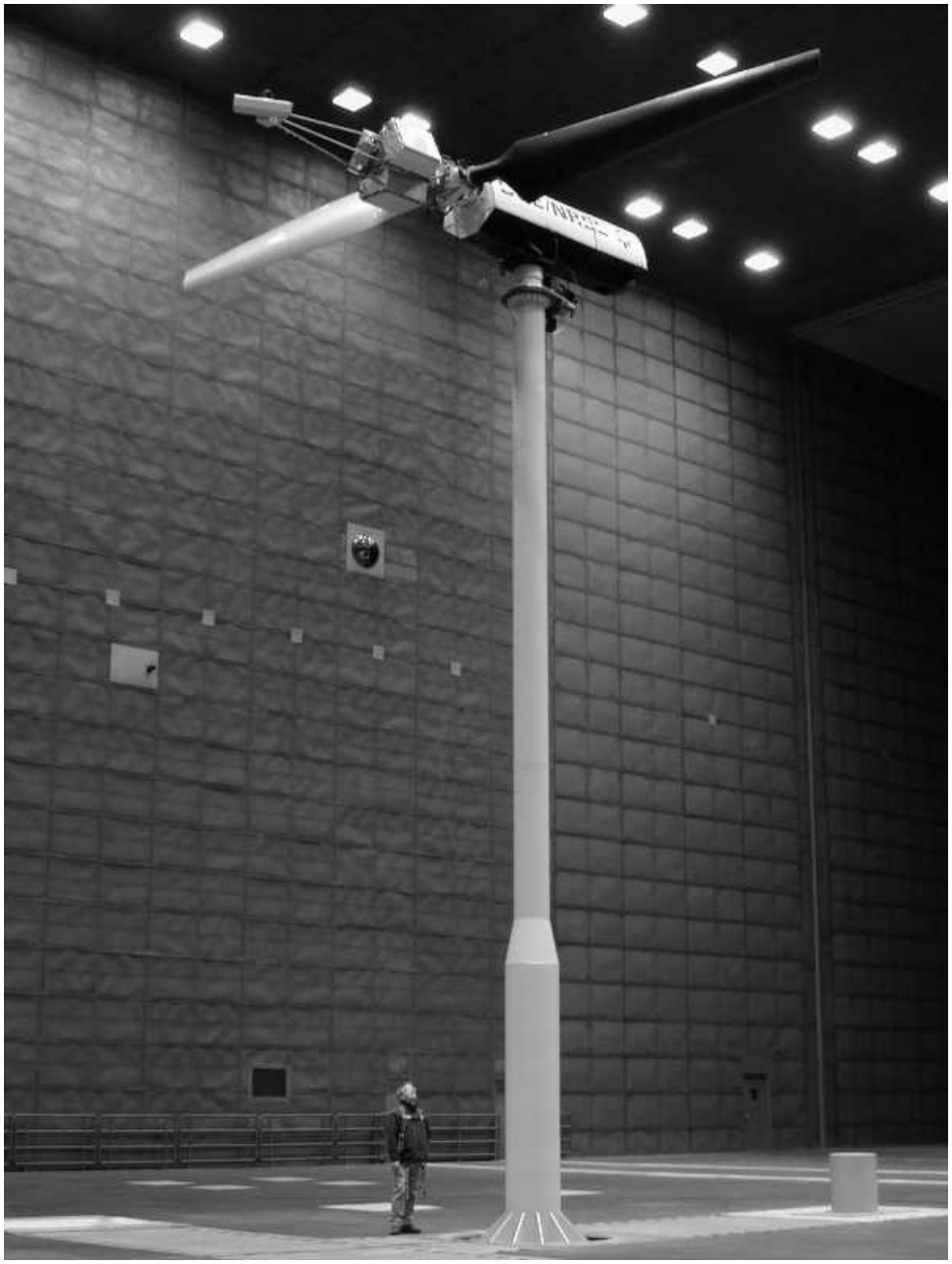

Figure 1.1 *UAE phase-VI rotor in the NASA-Ames wind tunnel (from the NREL website)*

2. AERODYNAMIC COEFFICIENTS IN DEEP STALL

2.1 Introduction

For the S809 airfoil most measured data were available for angles-of-attack up to stall, while many of the measurements on the UAE phase-VI rotor in the NASA-Ames wind tunnel were carried out with the blades in stall. This means that the aerodynamic coefficients in deep-stall also have to be known/verified, for which purpose the empirical tool *StC* has been developed at ECN. This tool *StC* was investigated and improved slightly in order to have a good basis for analysis of the UAE phase-VI rotor, and the analysis of wind turbines in general.

History

In [56] Björn Montgomerie described a method to estimate the aerodynamic coefficients of rotor blades 90 degrees to the wind. In this method empirical expressions were formulated for the drag coefficient, based on the drag of a flat plate including reductions from e.g. the leading edge radius and the airfoil thickness. Montgomerie also formulated a model for the distribution of the drag coefficient over the blade span as function of the aspect ratio of the blade, assuming that this distribution is similar to the height of a soap bubble.

In 2000 Lindenburg formulated an empirical model for the deep-stall coefficients at various angles of attack [44], based on the geometry of the airfoil cross section in a similar way as Montgomerie [56]. However, the reduction in drag due to the finite length (aspect ratio) was described as a constant factor for the complete span, which is based on a formulation of the normal force coefficient only. The resulting program was called *StC* : 'Stall Coefficients'.
In 2001 the program *StC* was extended with expressions for the aerodynamic moment coefficient.

Comparison of the deep-stall coefficients of *StC* with measured coefficients still showed differences. These differences can be characterised with a 'skewness' of the normal force coefficient such that the maximum occurs at angles just below 90deg, and a characteristic distribution of the tangential force coefficient. Most of these deep-stall measurements were addressed to vertical axis wind turbines. A description is given of the program *StC* that has an improved model for the normal-force and tangential-force coefficient. These improvements were mainly based on coefficients published by Bloy & Roberts [8], Sharpe [66], and Sheldahl et al. [67]

2.2 Drag Coefficient at 90 deg to the Wind

For the aerodynamic coefficients in deep stall, empirical relations were derived from (measured) coefficients of various sources. The different steps in the derivation are explained here. Because it was shown that for flat plates the deep-stall loads are dominated by a normal force, the derivation presented here starts with the drag coefficient of an airfoil perpendicular to the flow.

2.2.1 Neglect the shape of the downwind side

In "Fluid-Dynamic Drag" of Hoerner [34], Figure 33 on p.3-17 and Figure 36 on p.3-18 give the drag coefficients of 2D objects with several elementary shapes, see Figure 2.1. By comparison of objects with similar upwind shape in these figures, it was concluded that if the downwind side does not extend deep into the wake, the shape of the downwind side has little or no effect on the flow and neither on the value of the drag coefficient.

2.2.2 Influence of the ”wedge angles”

For a flat plate perpendicular to the flow, the drag coefficient is given in several references:
Hoerner [34]: 1.98, Ostowari & Naik [57]: 2.06, Viterna [83]: 2.01.
For simplicity the drag coefficient in *StC* is chosen as $C_{\rm d}({\rm flat}, 90) = 2$.

For 2D objects with sharp edges the flow leaves the object in the direction of these edges, which results in a lower drag compared to a long flat plate. From Hoerner, "Fluid-Dynamic Drag" [34, p.3-18, Fig.34], the drag of triangles with their edge upwind is fitted with:
$C_{\rm d} = 1.98 - 0.4\,\phi - 0.16\,\phi^2$, see also Figure 2.2.
Here ϕ is one of the ”wedge angles”, which equals $\phi = 90^\circ - \varepsilon$ in Figure 2.2.
For airfoils the following expression was fitted for *StC* :
$C_{\rm d} = 2 - 0.2\,(\phi_{\rm nose} + \phi_{\rm tail}) - 0.08\,(\phi_{\rm nose}^{\,2} + \phi_{\rm tail}^{\,2})$.

In "Fluid-Dynamic Drag" [34, p.3-17, Fig.33] Hoerner gives for the drag of a plate $C_{\rm d}$ = 1.98 and for the drag of a 45deg triangle $C_{\rm d}$ = 1.55. This reduction of 0.43 matches reasonably with the reduction of 0.413 following the expression given above.

2.2.3 Influence of the nose (and trailing) radius

For the trailing edge the direction in which the flow leaves the airfoil is well defined. The leading edge has a non-zero radius that may give some suction and lead the flow more downwind, while it reduces the drag. For an ’oval-type’ of edge-radius with a circular shape the drag is given by:

- Hoerner, "Fluid-Dynamic DRAG" [34, p.3-9, Fig.13] ($Re_{\rm subcrit}$):
  $C_{\rm d}({\rm cylinder}) \;\; = 1.11$;
  $C_{\rm d}({\rm triangle,\ flat\ side\ upwind,\ r_{edge}/h} = 0.25) = 1.32$;
  $C_{\rm d}({\rm square,\ r_{edge}/h} = \ 0.02) \; = 1.55$.
- Hoerner; "Fluid-Dynamic Drag" [34, p.3-17, Fig.33],
  $C_{\rm d}({\rm flat\ plate}) \; = 1.98$;
  $C_{\rm d}({\rm oval}\ 1:2) \; = 1.60$;
  $C_{\rm d}({\rm cylinder}) \; = 1.17$;
  $C_{\rm d}({\rm half-cylinder,\ upwind}) = 1.16$;
  $C_{\rm d}({\rm half-tube,\ upwind}) \; = 1.20$.

For the ”oval-type” of edge radius, the drag coefficient fits more or less:
$C_{\rm d} = 1.98\,(1 - 0.4(r_{\rm nose} + r_{\rm tail})/c)$.

- ESDU 79026 [24, Figure 6] gives drag coefficients of rounded triangles for $Re_{\rm subcrit} = 1.5 \cdot 10^5$:

$r_{\rm nose}/c = r_{\rm tail}/c$	$C_{\rm d}$
0.03139	1.94
0.0515	1.905
0.07578	1.785
0.10566	1.64

Probably because the rear-body of these triangles has an influence on the flow in the wake, these drag coefficients deviate from the linearised relation, see Figure 2.3.

The nose-radius of an airfoil approaches more an elliptical shape, for which ESDU 79026 [24, Figure 8] gives the drag coefficients of ellipses at $Re_{\text{subcrit}} = 1.5 \cdot 10^5$:

t/c	$r_{\text{nose}}/c = r_{\text{tail}}/c$	C_{d}
1/10	0.005	1.83
1/5	0.02	1.77
1/4	0.03125	1.74
1/3	0.05556	1.70
1/2	0.125	1.60
1/1.8	0.15432	1.56
1/1.6	0.19531	1.51
1/1.4	0.2551	1.45
1/1.2	0.34722	1.35
1/1.0	0.5	1.2

For relatively flat ellipses the reduction in drag coefficient is stronger than for the "oval-type" of nose (and tail) radius and can be approached (a bit conservative) with $C_{\text{d}} = 2 - 1.08\sqrt{r_{\text{edge}}/c}$, see also Figure 2.3. Assuming a sharp trailing edge, the following expression is used in *StC* :

$$C_{\text{d}} = 1.7 + (0.3 - \phi_{\text{nose}}\,(0.2 + 0.08\,\phi_{\text{nose}})) \cdot (1 - 1.8\,\sqrt{r_{\text{nose}}/c}) - \phi_{\text{tail}}(0.2 + 0.08\,\phi_{\text{tail}})\,.$$

This formulation for the combined effect of nose radius and angle of the nose camber was chosen such that the influence of the nose camber decreases to zero if the nose radius approaches 0.31*c*. For such a large nose radius, the shape of the leading edge is roughly cylindrical.
Also the influence of the nose-radius reduces to zero if the nose camber ϕ_{nose} exceeds 60.4 deg, which is close to the separation point of a cylinder at $Re = 10^5$.

2.2.4 Influence of aspect ratio

Figure 28 on page 3-16 of Hoerner [34] and the figure on page 3-4 of Hageman [30] show that for an aspect ratio up to 5 the drag coefficient of a rectangular flat plate perpendicular to the flow is nearly constant, 1.17 to 1.2, which is the same value as for a round flat plate. Only for very large values of the aspect ratio the drag coefficient increases to about 2.0. Hoerner already mentioned [34, p.3-15 and 3-16] that the difference between the drag coefficients of 2D plates compared to 3D plates is caused by a difference in the negative rear-side pressure, or 'base-drag'.

Vortex shedding
Measurements on bluff bodies (which have a significant wake of separated flow) show that, depending on the flow-structure of the boundary layer, vortex shedding takes place. Here the flow-structure of the boundary layer depends on the Reynolds number, surface roughness, flow turbulence etc. It has been discussed by Riberio [60] that the average drag of the blunt body is proportional to the vortex shedding frequency ν, which is expressed with the dimensionless property called Strouhal number: $S = \nu\, D/V$.

By measurements on flat-plate and airfoil sections in a wind tunnel the influence of the end-plate diameter on the drag at 90deg angle of attack has been investigated by Kubo et al. [41] and by Farell & Fedeniuk [25]. The conclusion of Kubo's investigation is that for end-plate diameters larger than 8 times the chord, the drag coefficients appear to have a stationary (2D) value. Flow visualisations with smoke show that for large end plate diameters the wake contains at least one well-defined shed vortex while for smaller end-plate diameters the shed vortices break up early because 'air is sucked into the core of the vortex'. The minimum end-plate radius of 4 times the chord has some relation with the Strouhal number for 2D flat plates, which is 0.22 - 0.28. This breaking up of shed vorticity is the mechanism by which a rectangular flat plate at 90deg to the flow has already the "lower" drag coefficient of 1.2 for an aspect ratio of 5 or less.

Navier Stokes calculations by Zhang et al. [89] for the stationary conditions show a maximum 2D

drag coefficient for the S809 airfoil of about 1.2, see also section 3.2. Zhang et al. also concluded that this lower value was due to the absence of vortex shedding.

Vortex shedding of non-rotating stalled rotor blades
It was concluded that an infinitely long flat plate perpendicular to the wind has the higher drag coefficient of 2.0 compared to the lower drag of 1.2 for a rectangular flat plate with aspect ratio less than 5 because an infinite long plate has a structured vortex shedding in the wake.
A modern large rotor blade differs from an infinitely long flat plate by:

- An aspect ratio in the order of 14 to 20, which is "between 5 and infinite". This wake may have a partially organised vortex structure. (The UAE phase-VI rotor has an aspect ratio of 7.2).
- A tapered geometry, which may give a span-wise variation of the Strouhal number.

The NASA-Ames measurements for the non-rotating state may reveal information to what extent the wake in deep stall has a periodic vortex shedding structure with the higher drag, or have a more 'chaotic' wake with the lower drag. It must be expected that large rotor blades with an aspect ratio around 15 to 17 may show a more organised wake structure than the UAE phase-VI rotor with an aspect ratio of 7.2.

Modelling in the StC program
In Hoerner "Fluid-Dynamic Drag" [34, p.3-16, Fig.28] the drag coefficient is given as a function of aspect ratio $AR = R^2/Area$. This has been fitted by several authors:

Larry Viterna $(AR < 50)$: $C_{\mathrm{d\,3D}} = 1.11 + 0.018\,AR$;
Björn Montgomerie : $C_{\mathrm{d\,3D}} = 1.98 - 0.81\,(1 - \exp(-20./AR))$;
Hibbs and Radkey (PROP) : $C_{\mathrm{d\,3D}} = 1.98 - 0.81\,\tanh(12.22/AR)$.

Compared to the measured values published by Hoerner, Fig. 2.4, the expression of Hibbs and Radkey shows a good trend for very large aspect ratios but gives a small under-prediction for an aspect ratio less than 10. For *StC* a good and slightly conservative fit was found similar to the relation of Montgomerie: $C_{\mathrm{d\,3D}} = 2.0 \; - 0.82\,(1 - \exp(-17./AR))$.

Based on a "soap bubble" analogy Björn Montgomerie [56] gave a description of the decay of aerodynamic drag towards the tip. Because the tapered geometry of a rotor blade already differs from a rectangular flat plate and because the drag distribution on the and the down-wind side are different, it was found premature to use such a formulation.

In fact the nose radius and the wedge angles give a decrease in drag near the leading and trailing edges while the ends of the plate (or rotor blade) are still considered straight. Based on the fact that an angle of attack unequal to 90deg also gives a reduction of the normal force, the so-called "effective aspect ratio" is introduced as $AR_{\mathrm{eff}} = AR \cdot 2.0/C_{\mathrm{n}}(\alpha)$. The factor 2.0 is the drag coefficient of a long flat plate at 90deg to the flow. The expression for the 3D drag coefficient thus becomes $C_{\mathrm{d\,3D}} = C_{\mathrm{d\,2D}}\,(\,1 - 0.41\,(1 - \exp(-17./AR_{\mathrm{eff}}))\,)$.

2.3 Aerodynamic Coefficients as Function of Angle of Attack

In the previous sections the 2D drag coefficient is described for cross sections that are perpendicular to the flow, for an angle of attack of 90deg. In the following this coefficient is named $C_{\mathrm{d}}(90)$.

2.3.1 Normal force coefficient for flat plates

In "Fluid-Dynamic Lift" [35, p.21-1], Hoerner mentions that according to theory the normal force on the forward side of the plate is given by $C_{\mathrm{n}} = 2\,\pi\,\sin\alpha/(4 + \pi\sin\alpha)$.
Following Hoerner, this is without the negative pressure on the rear side. Including this negative rear-side pressure in a similar way gives $C_{\mathrm{n}} = C_{\mathrm{d}}(90)\,\sin\alpha/(0.56 + 0.44\,\sin\alpha)$.

Aspect ratio effects for various angles of attack

For the effect of aspect ratio at various angles of attack an investigation was done into several formulations to combine the aspect-ratio effect and the distribution as a function of angle of attack. An expression that fits well with measured data is found to be

$$C_n = C_d(90)\,[1/(0.56 + 0.44\,\sin\alpha) - 0.41\,(1 - \exp(-17./AR_{eff}))]\,\sin\alpha\ .$$

Effects of leading-edge radius

Measurements for the symmetrical NACA0009, NACA0012, NACA0015, and NACA0018 airfoils [67] show that the normal force coefficient has its maximum value at an angle of attack near 85deg. This shift in maximum value is caused by the smaller influence of the leading-edge radius at angles of attack below 90deg. This 'skewness' is approximated with a second-order sinusoidal function of the angle-of-attack, that depends on the dimensionless leading-edge radius r_{nose}/c :

$$C_n = C_d(90)\,[1/(0.56{+}0.44\sin\alpha) - 0.41(1{-}\exp(-17./AR_{eff}))]\cdot[\sin\alpha{+}0.1\sqrt{r_{nose}/c}\,\sin(2\alpha)]\ .$$

2.3.2 Tangential force coefficient

Empirical fit to measured coefficients

For the research into the self-starting capabilities of vertical axis wind turbines the tangential force coefficients have been measured for angles-of-attack ranging from 0deg to 180deg. These measurements show that at 90deg angle-of-attack the tangential force is slightly positive (towards the leading-edge) while it may become negative for angles-of-attack between 20deg and 60deg.

An empirical fit was derived for the tangential force coefficient based on the fact that the tangential-force is the result of a varying orientation of the resultant force, and thus expressed as fraction of the normal force coefficient. This empirical fit was formulated as function of the leading-edge radius only: $C_t = |C_n|\,\sqrt{r_{nose}/c}\,(0.3 - 0.55\,\cos\alpha)$.

Viscous drag

Although it is a small contribution, the viscous tangential force coefficient is added considering that it acts only on the upwind side of the airfoil. The value of this tangential force is thus minus half the drag coefficient in laminar flow: $C_{t\,viscous} = -1/2 \cdot 0.0075\,\cos\alpha$.
For various angles of attack the tangential force is fitted with measurements which resulted in the relation: $C_t = -1/2 \cdot 0.0075\,\cos\alpha + |C_n|\,\sqrt{r_{nose}/c}\,(0.3 - 0.55\,\cos\alpha)$.
Here the factor 0.3 changes sign for negative angles of attack.

The lift- and drag coefficients finally apply to:

$$C_l = C_n \cdot \cos\alpha + C_t \cdot \sin\alpha \quad \text{and} \quad C_d = C_n \cdot \sin\alpha - C_t \cdot \cos\alpha\ .$$

For small values of r_{nose}/c the angle-of-attack for zero-lift can be approximated with
$90deg + 180deg/\pi\ (0.3\,\sqrt{r_{nose}/c})/(1 - 0.55\,\sqrt{r_{nose}/c})$.

The empirical expressions for the normal- and tangential force coefficients in *StC* were derived by fitting with measured 2D aerodynamic coefficients for some 15 airfoils. For the NACA0012 airfoil, a comparison of the 2D deep-stall coefficients from *StC* and the measurements published by D.J. Sharpe [66] are shown in Figure 2.5 for a Reynolds number $2{\cdot}01^6$. As follows from Figure 2.5, the tangential-force coefficients match well while the normal-force coefficients have their improved 'skewness'. The normal-force coefficients for a 90deg angle-of-attack shows an under-estimation compared to the data from Sharpe [66]. However, compared to the measurements from other sources or the measurements for other airfoils, the normal-force coefficients of *StC* show an over-estimation.

2.3.3 Moment coefficient

For a flat plate perpendicular to the flow the resultant of the normal force acts at the 50% chord location. For a curved plate (such as the up-wind side of an airfoil perpendicular to the flow) this location depends on the nose-radius and the angles of the leading and trailing edge. Here a positive tail angle will shift the location $x_{\rm cp}$ to the leading edge while a positive nose radius and a positive nose-angle shift this location $x_{\rm cp}$ to the trailing edge. With this dependency and using similar expressions as for the drag at 90deg angle of attack, see 2.2.3, the following expression was obtained for $x_{\rm cp}$, measured from the leading edge:

$$x_{\rm cp}(90) = 0.5 \; - \; 0.35 \cdot [\, \phi_{\rm tail}(0.2 + 0.08\,\phi_{\rm tail}) + (0.3 - \phi_{\rm nose}\,(0.2 + 0.08\,\phi_{\rm nose})) \cdot (1 - 1.8\,\sqrt{r_{\rm nose}/c}) \; - \; 0.3\,] \; .$$

The factor 0.35 was obtained by fitting with measurements. For negative angles of attack, the same expression is used but then with the tail-angle of the upper surface and with different signs where necessary. For various angles of attack the expression for the moment coefficient becomes:

$$C_{\rm m}(\alpha) = -C_{\rm n}(\alpha) \cdot [\, x_{\rm cp}(90) - 0.16 \cdot (1 - \alpha/90) \; - 0.25\,] .$$

Here the factor 0.16 was also obtained by fitting with measurements.

2.4 Reversed Flow

For wind turbines that are parked (downwind) with the blades pitched to vane position, the flow over the airfoils has an 180 degrees angle of attack. Because most turbines are parked during strong winds, the static aerodynamic loads may be design driving for the blade. Although the sharp trailing edge and the rounded leading edge of airfoils make it hard to describe the state of reversed flow, a very rough attempt is made to assess the aerodynamic coefficients for angles of attack from 170deg up to 190deg. These are mainly based on the properties of an ellipsis.

Lift coefficient

Although airfoils are not symmetrical with respect to the chord line it is still considered that for reversed flow the zero-lift angle of attack is 180deg. In section 2.2.1 it was mentioned that Miley [53] gives for the NACA0015 section a maximum reversed lift coefficient of $C_{\rm l}(171) = -0.80$. For a 12% thick airfoil section in reversed flow ($Re = 2 \cdot 10^6$) Hoerner gives a graph [35, p.2-8, Fig. 14] that shows a maximum reversed lift coefficient of 0.8 at an angle of attack of 188deg. Based on these references it was concluded that for thin airfoils the maximum lift coefficient in reversed flow is about (+/-)0.8. For simplicity this maximum lift coefficient occurs at angles of attack of 190deg and 170deg, where in the latter case the lift coefficient is in fact -0.8. Based on the nose radius of the airfoil, the slope of the lift curve is fitted to the characteristics of an ellipsis in Fig.13 on p.2-7 in Hoerner [35] (with α in degrees): $\partial C_{\rm l}/\partial\alpha = 0.108 - 1.5\,r_{\rm nose}/c$.
If this slope of the lift curve is too small to give a maximum lift coefficient of 0.8 at 190deg then the maximum "reversed lift coefficient" $C_{\rm l}(190) = 10\,(0.108 - 1.5\,r_{\rm nose}/c)$ is used.

Drag coefficient

The sharp trailing edge will probably cause a turbulent reversed flow. For an ellipsis in turbulent flow Hoerner [35, p.6-9] gives an expression for the drag coefficient as function of thickness ratio. Re-writing this expression as function of nose-radius gives:

$$C_{\rm d}(180) = 0.005\,(\,2 + \sqrt{2\,r_{\rm nose}/c}\,(4 + 240\,r_{\rm nose}/c)\,) \; .$$

For other angles of attack in reversed flow, the drag coefficient is calculated with

$$C_{\rm d}(\alpha) = C_{\rm d}(180) + 0.0003\,(\alpha[{\rm deg}] - 180)^2 \; .$$

Moment coefficient

For the moment coefficient in reversed flow the lift and drag are assumed at the 75% chord location.

2.5 Comparison with Measured Coefficients

Infinite Aspect Ratio

Aerodynamic coefficients for large angles of attack were found in several publications.
For 2D airfoil sections comparison of measured and calculated coefficients gives:

		$C_d(90)$		$\alpha(C_l = 0)$		$C_{l,max}$		$\alpha(C_{l,max})$	
Airfoil	Ref.	meas.	*StC*	meas.	*StC*	meas.	*StC*	meas.	*StC*
NACA0012	[76]	2.09	1.902	92.54	92.05	1.11146	1.143	40.0	40.3
Idem, TDT tunnel		2.09	1.902	92.0	92.05	1.118	1.143	41.0	40.3
NACA0015	[53]	1.7	1.878	92.9	92.59	0.933	1.137	50.0	40.4
NACA0015	[67]	1.81	1.878	94.0	92.59	1.05	1.137	42.0	40.4
NACA0018	[79]	1.81	1.853	95.5	93.14	1.07	1.143	50.0	40.3
NACA4409	[57]	2.10	1.985	91.356	91.43	1.22	1.182	41.0	39.8
NACA4412	[57]	2.06	1.959	92.23	91.87	1.21	1.174	41.0	40.1
NACA4415	[57]	2.068	1.933	92.785	92.30	1.2	1.166	40.0	40.4
NACA4418	[57]	2.06	1.906	92.097	92.73	1.17	1.157	40.0	40.5
NACA0012	[51]	2.05	1.902	92.63	92.05	1.171	1.143	42.0	40.3
NACA23012	[51]	2.082	1.948	92.33	91.78	1.217	1.166	40.0	40.1
NACA23017	[51]	2.078	1.902	92.55	92.40	1.152	1.149	45.0	40.4
FX 84-W-127	[51]	2.00	1.964	93.3	91.64	1.232	1.173	45.0	40.0
FX 84-W-218	[51]	2.04	1.939	96.4	92.63	1.152	1.175	45.0	40.5
LS-421 mod.	[51]	2.02	2.010	96.5	91.80	1.195	1.205	47.0	41.0
NACA63-215	[8]	1.98	1.959	92.0	91.97	1.094	1.176	45.0	40.2
GA(W)-1	[62]	1.83	2.032	90...	91.58	1.094	1.213	45.0	40.0
Idem. upside down		1.72	1.794	90...	91.56	1.094	1.082	45.0	-40.4

Finite Aspect Ratio

For airfoil sections with finite aspect ratio, comparison of measured and calculated coefficients gives:

		Asp.	$C_d(90)$		$\alpha(C_l = 0)$		$C_{l,max}$		$\alpha(C_{l,max})$	
Airfoil	Ref.	ratio	meas.	*StC*	meas.	*StC*	meas.	*StC*	meas.	*StC*
NACA0015	[4]	5.536	- - -	1.151	- - -	92.59	0.79	0.769	42.0	37.3
NACA4409	[58]	12	1.75	1.370	93.5	91.43	1.048	0.876	45.0	37.5
NACA4409	[58]	9	1.59	1.296	92.3	91.43	0.937	0.839	35.0	37.1
NACA4409	[58]	6	1.45	1.220	93.5	91.43	0.835	0.802	35.0	36.6
NACA4412	[58]	12	1.69	1.356	92.5	91.87	0.991	0.871	35.0	37.7
NACA4412	[58]	9	1.64	1.282	91.7	91.87	0.886	0.834	35.0	37.4
NACA4412	[58]	6	1.45	1.206	93.3	91.87	not	0.797		37.0
NACA4418	[58]	12	1.68	1.327	94.2	92.73	1.002	0.861	35.0	38.3
NACA4418	[58]	9	1.48	1.254	94.2	92.73	0.814	0.824	45.0	37.6
NACA4418	[58]	6	1.32	1.177	92.7	92.73	not	0.786		37.4
ClarkY	[59]	8	1.47	1.251	88.5	91.30	0.978	0.812	38.0	37.0
ClarkY	[53]	6	1.36	1.201	89.5	91.30	0.89	0.788	33.0	36.6

For the ClarkY airfoil the angle of attack for zero lift does not match well. A possible reason for this misfit can be that for the measurements the angle of attack is the angle with respect to the (nearly flat) pressure side of the ClarkY airfoil. The chord-line from trailing to leading edge of the Clark-Y airfoil makes an angle of about 2deg with respect to the nearly flat pressure side, which is just the difference for $\alpha_{Cl=0}$.

Comparison of the moment coefficients

The expression for the aerodynamic moment coefficients is in fact the product of the normal force coefficient c_n and the location of its resultant force x_{cp}.
Since the normal force coefficient is evaluated in the previous sections, the following table compares the measured and predicted locations of this normal force coefficient for 90deg angle of attack.

		$x_{cp}(90)$		$x_{cp}(-90)$	
Airfoil	Ref.	meas.	*StC*	meas.	*StC*
NACA0012	[52]	0.2355	0.2635	- - -	0.2635
NACA4415	[57]	0.2569	0.2677	- - -	0.2664
NACA63215	[8]	0.2576	0.2731	- - -	0.2696
NACA0012	[51]	0.2573	0.2635	0.2620	0.2635
NACA23012	[51]	0.2696	0.2511	0.2893	0.2797
NACA23017	[51]	0.2717	0.2583	0.2854	0.2828
FX84W127	[51]	0.2644	0.2733	0.2829	0.2635
FX84W218	[51]	0.280	0.2798	0.2965	0.2901
NASALS421	[51]	0.2738	0.2694	0.2839	0.2866

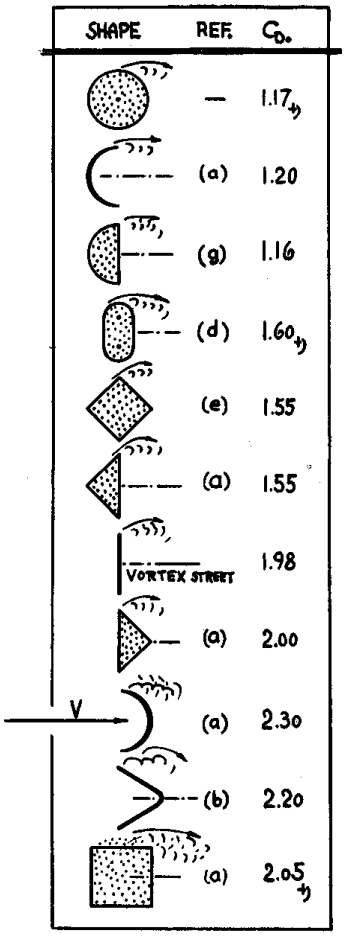

Figure 2.1 *Drag coefficients of various 2D objects, $Re = 10^4 \ldots 10^6$ (from Hoerner, [34])*

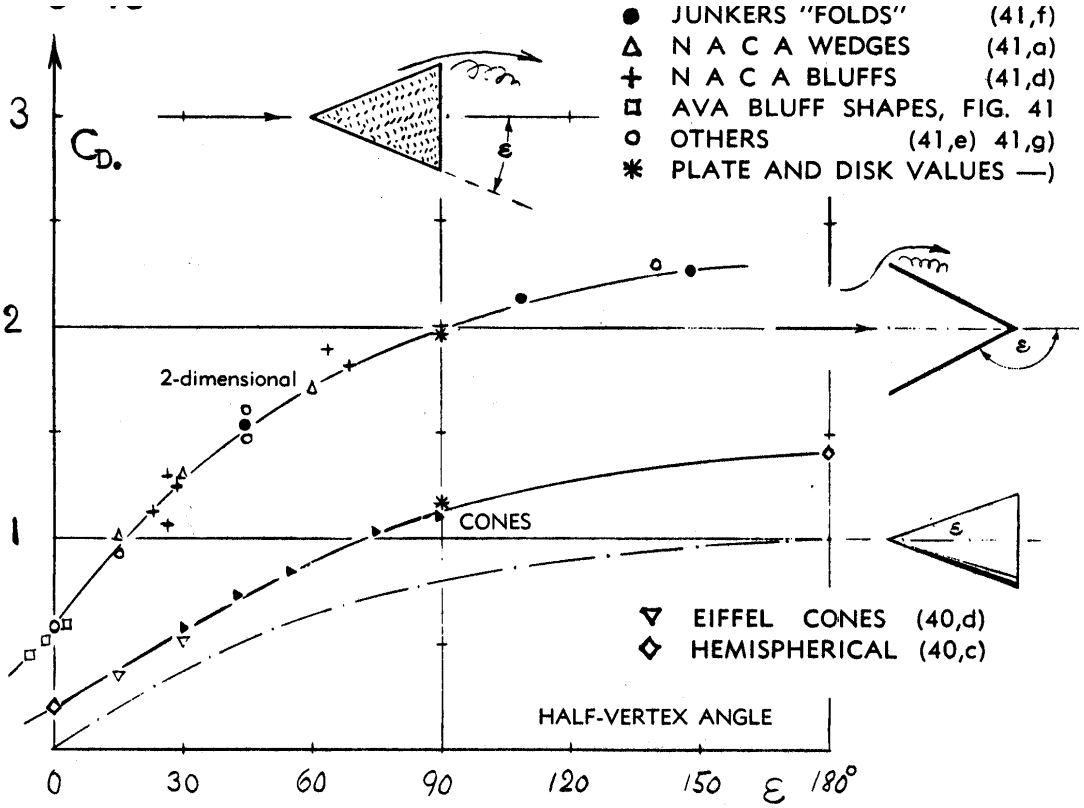

Figure 34. Drag coefficients of wedges, cones and similar shapes as a function of their half-vertex angle. At $\alpha = 90°$ the shape is that of plates in normal flow; between 90 and 180°, "folds" and hollow cones are plotted with their opening against the oncoming stream.

Figure 2.2 *Drag coefficients of blunt 2D wedges,* $Re = 10^4 ... 10^6$ *(from Hoerner, [34])*
(The angle ε corresponds with $90° - \phi_{\text{nose}}$ or $90° - \phi_{\text{tail}}$.)

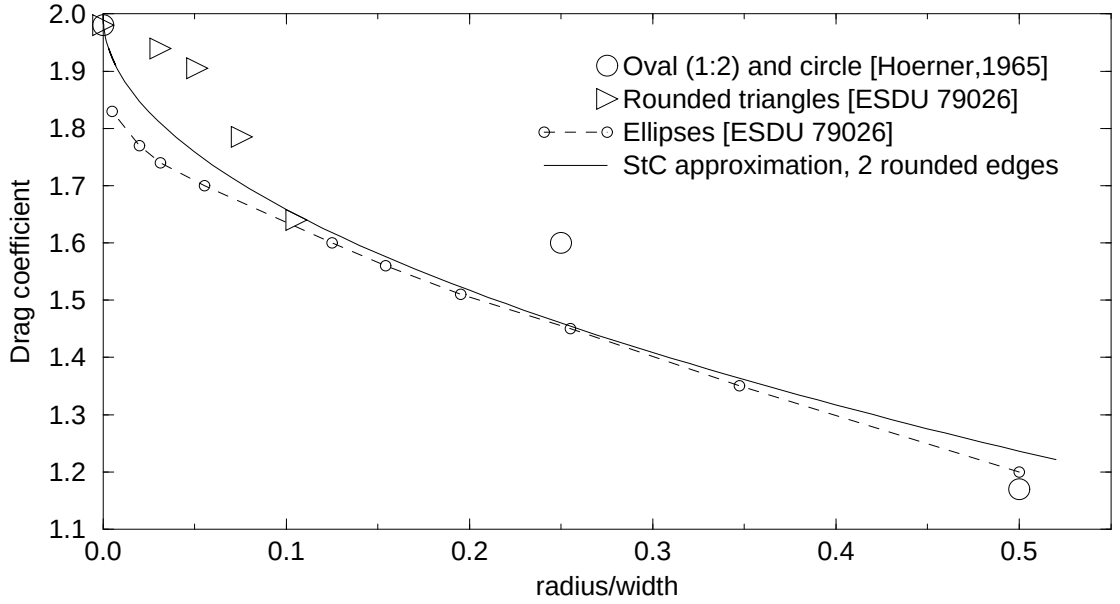

Figure 2.3 *Drag coefficients of ovals and ellipses*

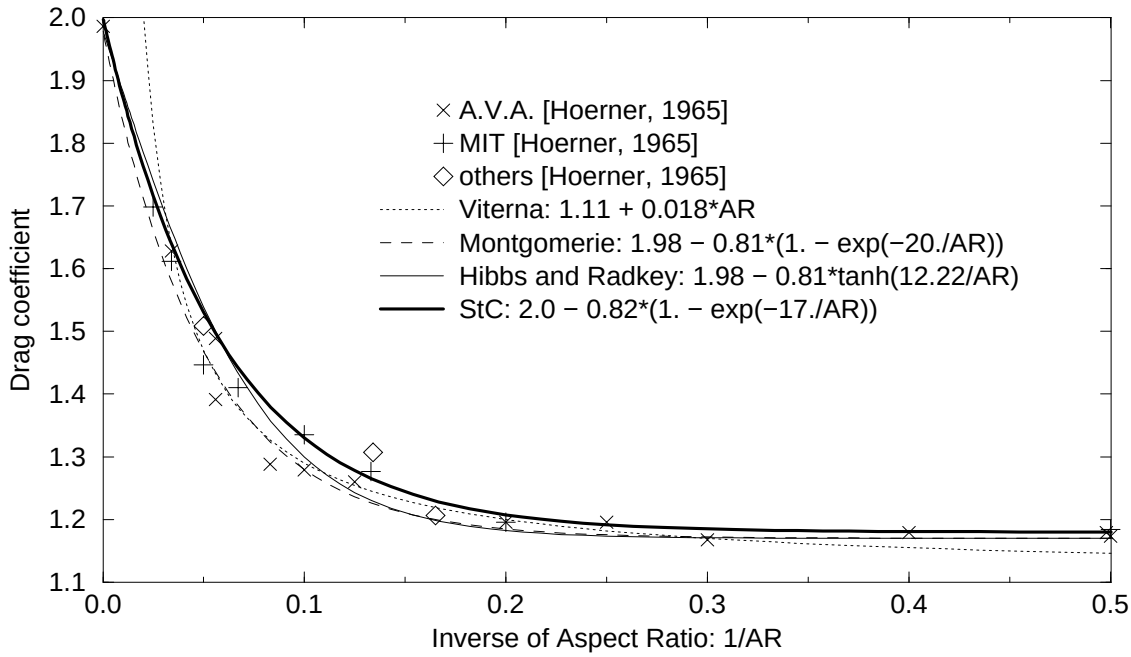

Figure 2.4 *Drag of a rectangular plate as function of aspect ratio*

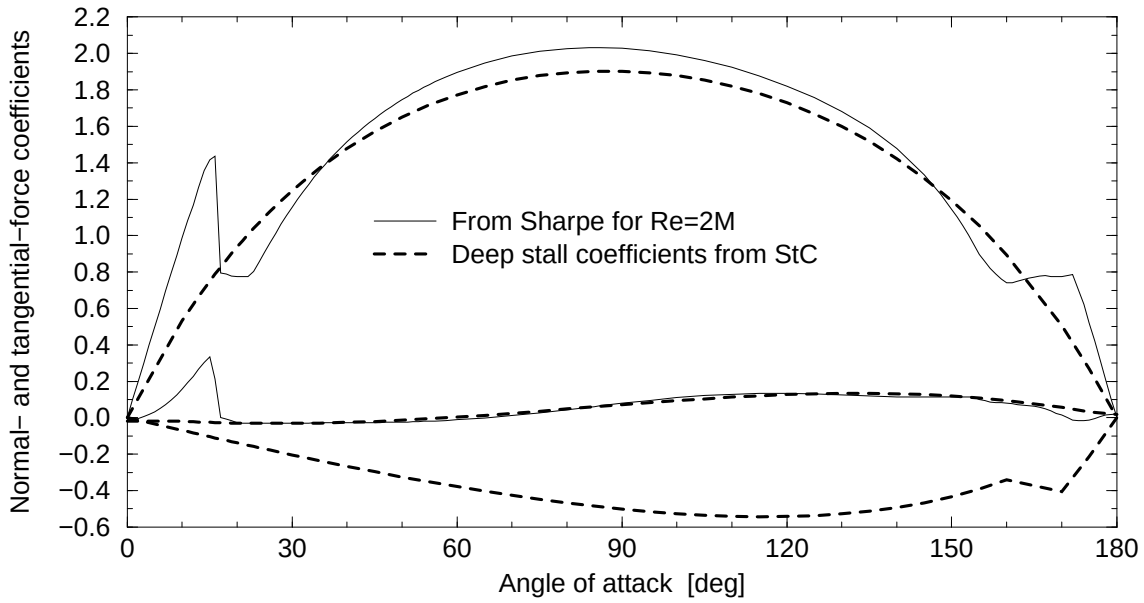

Figure 2.5 *Normal- and tangential force coefficients of NACA0012 in deep stall*

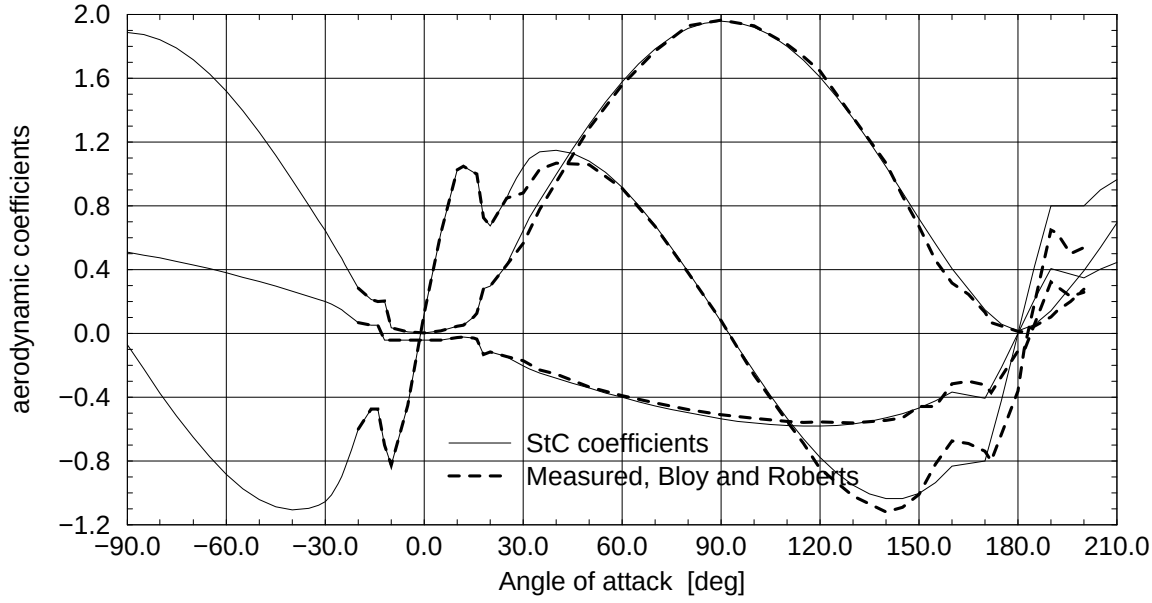

Figure 2.6. *Coefficients for the NACA63-215 airfoil, infinite aspect ratio.*

3. AERODYNAMIC COEFFICIENTS OF THE S809 AIRFOIL

The UAE phase-VI rotor has the 20.95% thick S809 airfoil shape. This airfoil was designed to have a restrained (relatively low) maximum lift coefficient of 1.0 and a design lift coefficient of 0.5 for a Reynolds number of $2 \cdot 10^6$, see [73]. For lift coefficients between 0.2 and 0.8 the drag coefficient was low, while the aerodynamic moment coefficient should not be smaller than -0.05. For the design Reynolds number and small angles-of-attack the airfoil has a weak laminar separation bubble on either sides. For larger angles of attack the suction surface separation bubble moves toward the leading edge while the lower surface bubble moves toward the trailing edge. For an angle of attack of about 8 deg or larger the flow becomes turbulent just aft of the leading edge. For angles of attack of 10deg until 15deg the flow has a 'stable' separation point near 50% chord location. Above 15deg separation moves to the leading edge.

The aerodynamic coefficients of the S809 airfoil described here are for the non-rotating conditions of the UAE phase-VI turbine in the NASA-Ames wind tunnel. The aspect ratio of the 10.058m diameter UAE phase-VI rotor is 7[1]. For a tunnel wind velocity of 15m/s and a rotational speed of 72rpm the Reynolds number is in the order of $0.9 \cdot 10^6$ to $1 \cdot 10^6$, see appendix A.

This chapter mainly describes the aerodynamic coefficients for a Reynolds number of (or close to) $1 \cdot 10^6$. For the higher Reynolds number of $2 \cdot 10^6$ the aerodynamic coefficients have been calculated by [88, 17, 86].

For comparison and evaluation of the measured coefficients and the corresponding angles-of-attack, some analytical investigations were performed first.

3.1 Calculated Aerodynamic Coefficients

For non-stalled flow, the aerodynamic lift and moment coefficients can be calculated reasonably with dedicated computer programs. The airfoil drag and the stalled flow conditions are hard to predict because they are related with turbulence. Following are the results of theoretical investigations into the zero-lift angle-of-attack and the slope of the lift curve.

3.1.1 Zero-lift conditions using thin airfoil theory

Following thin airfoil theory the distribution of the circulation is related to the shape of the camberline. On basis of thin airfoil theory, the method of Pankhurst, given in [1, page 72], can be used to obtain the zero-lift angle-of-attack and the aerodynamic moment coefficient:

$$\alpha_0 = 2 \sum_i A_i \, y_{\mathrm{c}.i} \qquad c_{\mathrm{m}} = 2 \sum_i B_i \, y_{\mathrm{c}.i} \; .$$

Here $y_{\mathrm{c}.i}$ gives the 'depth' of the camberline at chordwise location x_i.
The relative chordwise locations x_i and the coefficients are:

[1] The aspect ratio of the phase-VI rotor is 11, based on a 80% radius torque weighted chord (J.L. Tangler, NREL)

x_i	A_i	B_i	$y_{c.i\,(S809)}$
0.0	1.45	-0.119	0.0
0.025	2.11	-0.156	0.002254
0.05	1.56	-0.104	0.002883
0.1	2.41	-0.124	0.002032
0.2	2.94	-0.074	-0.001312
0.3	2.88	-0.009	-0.003917
0.4	3.13	0.045	-0.003489
0.5	3.67	0.101	0.000751
0.6	4.69	0.170	0.004527
0.7	6.72	0.273	0.007701
0.8	11.75	0.477	0.009430
0.9	21.72	0.786	0.008027
0.95	99.85	3.026	0.004884
1.0	-164.90	-4.289	0.0

For most NACA airfoils the thickness distribution is superimposed on the camberline such that the chord line (direction of zero angle-of-attack) does not run through the nose-end of the camberline. This is however not the case for the S809 airfoil, where it must be noted that this airfoil has a small leading edge radius. The shape of the camberline in the rightmost column of the table given above is obtained from the geometry coordinates of the S809 airfoil as was provided for the Blind Comparison in the fall of 2000. These coordinates were interpolated linearly to the x_i values needed, after which the averages of the upper contour and the lower contour are the values in the table above. After performing the summation following Pankhurst, the zero-lift angle-of-attack is -1.67deg and the aerodynamic moment coefficient is -0.055.

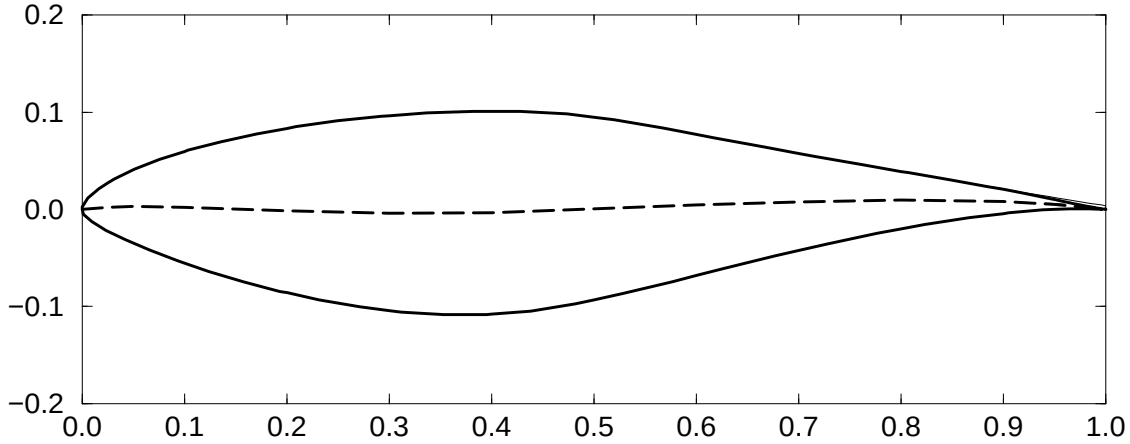

Figure 3.1 *S809 airfoil geometry with its camberline*

The shape of the S809 airfoil and of the camberline is plotted in Figure 3.1. The upper surface of the S809 airfoil has a light concave shape between 60% and 85% of the chord, after which the shape becomes convex. This last convex part gives a finite trailing wedge angle, which means that the flow will separate from either the upper or the lower surface. From the fact that the airfoil is designed and operated for positive angles-of-attack, separation will usually occur at the upper surface which gives some 'de-cambering' for the airflow. The effect of 'de-cambering' was investigated here with an assumption that the 'aerodynamic contour' for the outer flow, by fitting a parabola through the upper surface between 60% and 85% of the chord:

$$y_{\rm upper}/c = 0.0577 - 0.1913 \cdot (x/c - 0.7) + 0.038 \cdot (x/c - 0.7)^2 \ .$$

This parabola is extended to the trailing edge, see the thin line in Figure 3.2. After performing the summation following Pankhurst for the camberline based on the 'aerodynamic contour', the zero-lift angle-of-attack is -1.30deg and the aerodynamic moment coefficient is -0.047.

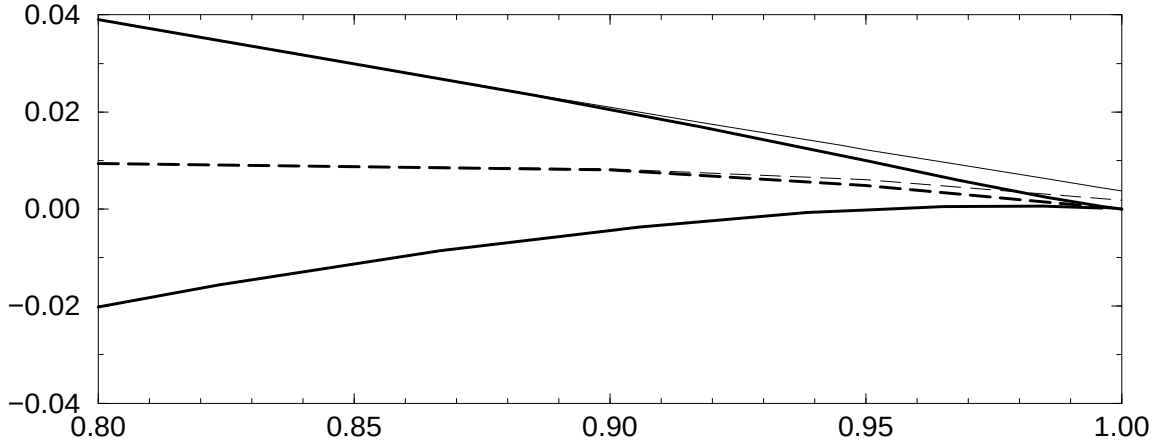

Figure 3.2 *Assumption for 'aerodynamic contour' near the tail*

3.1.2 2D calculations with airfoil design codes

Calculated aerodynamic coefficients for a Reynolds number of $1 \cdot 10^6$ were published by Dan Bernadett & Cees van Dam [7], in which they included the design calculations by Somers with the Eppler code [23]. The calculations by Bernadett & van Dam were performed with the airfoil design code MSES, developed by Drela. Zhang, Yang, & Ye [89] calculated the coefficients of the S809 airfoil with a Navier-Stokes code for a Reynolds number of $0.65 \cdot 10^6$ and a Mach number of 0.076, using different turbulence models. With the so-called 'isotropic $q - \omega$' turbulence model the aerodynamic coefficients were calculated for higher angles-of-attack.

The aerodynamic coefficients with the MSES code, the Eppler code, and the Navier-Stokes code of Zhang et al. are plotted in Figure 3.3.

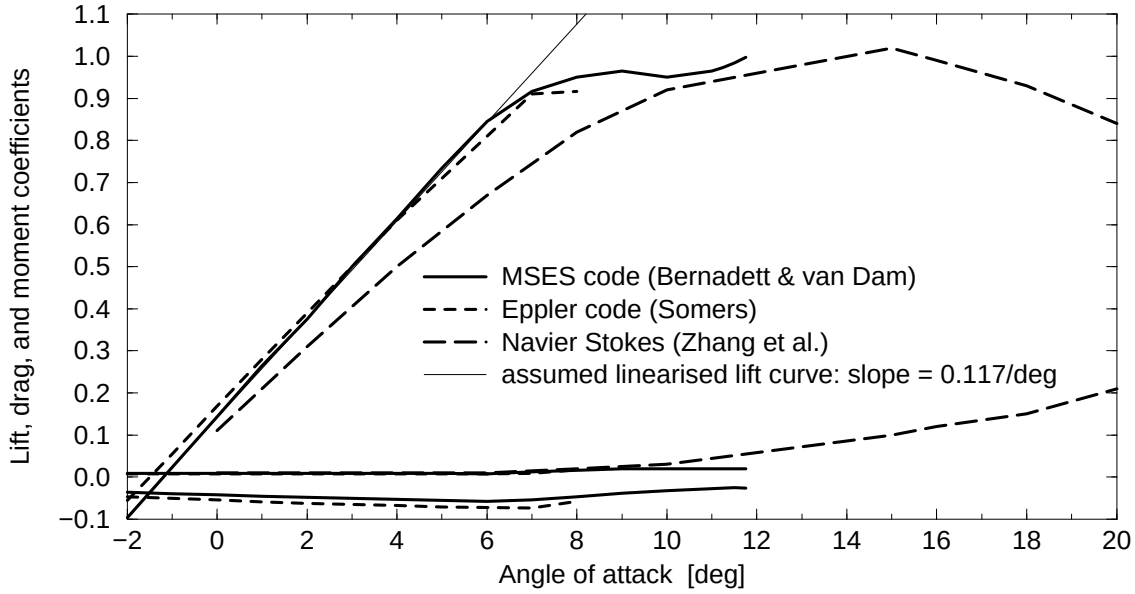

Figure 3.3 *Coefficients calculated with airfoil design codes*

The thin line included in Figure 3.3 is an assumed linearised relation for the lift coefficient. On basis of the calculations with the MSES code (by Bernadett and van Dam [7]) and from the measurements in the TU-Delft wind tunnel, the linearised lift coefficient has a zero-lift angle-of-attack of -1.20deg and a slope of 0.117/deg. From Figure 3.3 it follows that the Navier Stokes calculations by Zhang et al. give a far smaller slope of the lift curve.

3.2 Measured 2D Aerodynamic Coefficients

Wind tunnel measurements of airfoil loads are among others influenced by the presence of the tunnel walls. The tunnel walls give a restraint of the local flow expansion which leads to a local flow acceleration and thus a deviation of the velocity and of the chordwise pressure gradient. Another effect of the tunnel walls is the restraint of the upflow and downwash, in front and aft of the airfoil. For this last effect correction methods have been derived, which do not completely compensate for the tunnel-wall effects. Nevertheless it is still difficult to relate the angle-of-attack of the wind-tunnel configuration to the 2D angle-of-attack. This difficulty finally leads to a deviation of the slope of the lift-curve (c_l versus α).

Measured aerodynamic coefficients were provided by NREL from:
TU-Delft measurements for a Reynolds number of $1 \cdot 10^6$;
'OSU' measurements in the Ohio State University wind tunnel at Re = $0.75 \cdot 10^6$, and $1.0 \cdot 10^6$;
'CSU' measurements by the Colorado State University for Re = $0.3 \cdot 10^6$, $0.5 \cdot 10^6$, and $0.65 \cdot 10^6$;
The measured aerodynamic coefficients are plotted in Figure 3.4. The Reynolds number of these measurements are $1 \cdot 10^6$ except for the measurements in the CSU wind tunnel, of which the lift and drag coefficients for a Reynolds number of $0.65 \cdot 10^6$ are included.

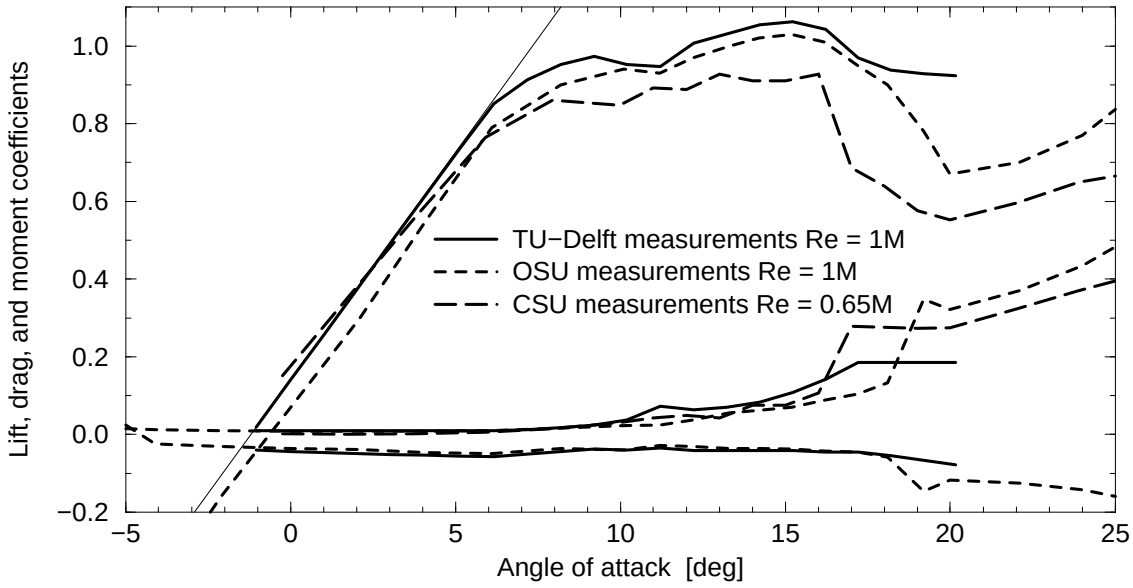

Figure 3.4 *Aerodynamic coefficients from 2D wind tunnel measurements*

From Figure 3.4 it follows that the coefficients measured in the Ohio State University tunnel have an angle-of-attack off-set of 0.6deg compared with the measurements in the TU-Delft tunnel. The lift-curve measured in the CSU wind tunnel appears to have a smaller slope and a smaller maximum lift coefficient, which may be a result from the 'tunnel-wall correction' method used.

3.3 Coefficients from the Non-rotating UAE Wind Tunnel Tests

The aerodynamic sectional loads of the UAE phase-VI rotor blades with the S809 airfoils were measured at a wind velocity of 20m/s and 30m/s. For the 20m/s wind velocity the Reynolds number ranges from $0.95 \cdot 10^6$ at the blade root to $0.5 \cdot 10^6$ at the tip. For the 30m/s wind velocity the Reynolds number range is from $1.4 \cdot 10^6$ to $0.75 \cdot 10^6$. The latter Reynolds numbers correspond better with the conditions of the rotating measurements, see appendix A.

Even for the non-rotating conditions the presence of the aerodynamic loads on the rotor wake has some influence on the local inflow distribution over the blade. This influence can be calculated with the trailing vortex representation of the wake structure. For this calculation the program *inflow* has been developed of which a description is given in appendix B. For the reconstruction of the aerodynamic coefficients of the UAE rotor blade, the radial locations at which the root vortex and the tip vortex leave the blade were 1.07m and 4.98m respectively. These locations are input properties for *inflow* and have a strong influence on the induced velocities at the inner and outer locations of the blade. The tip-vortex radius of 4.98m (= 99% R) was chosen smaller than the tip radius to account for the fact that the trailing-vorticity rolls-up at a smaller radius.

The measurements were performed for both
- stationary pitch angles with increments of about 5deg;
- slow continuous pitch sweeps, of which the 'ramp-down' data were used here.

Figure 3.5 shows the aerodynamic coefficients that were obtained from the measurements at 30m/s (stationary pitch angles), calculating the angle of attack straightforward from the angle between the local blade chord and the tunnel direction. This implies neglecting the deviations of the local flow direction due to lift of the airfoil, also called 'induced velocity'. The thin line in Figure 3.5

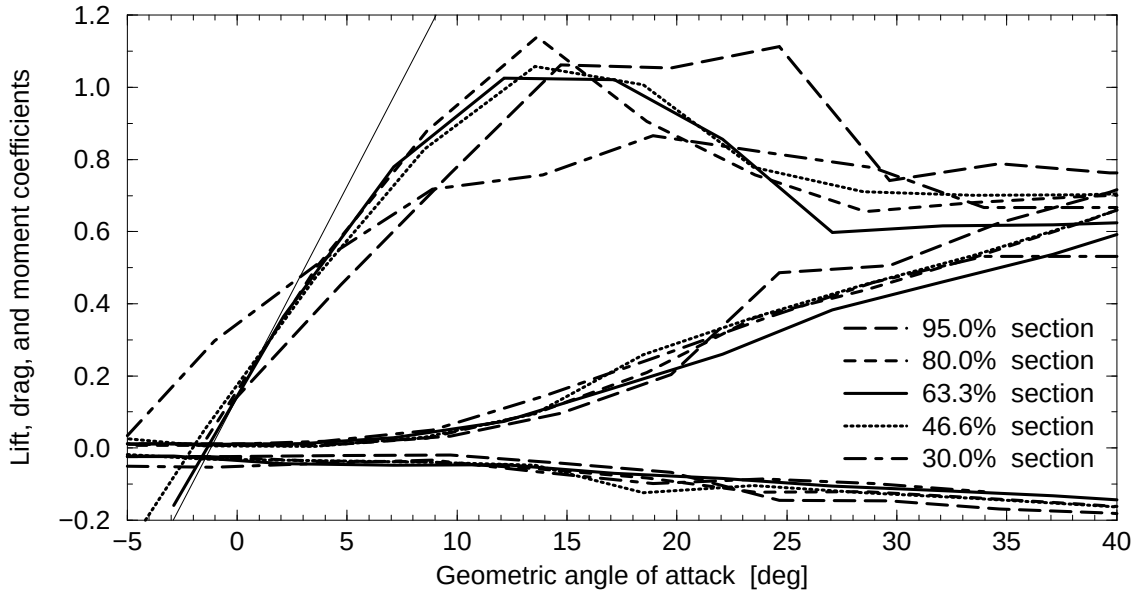

Figure 3.5 *Non-rotating aerodynamic coefficients without induced velocity*

represents the 'assumed linearised lift curve', with a slope of 0.117/deg and an intercept of -1.20deg. As can be seen from Figure 3.5, the slope of the lift-curves of the different sections is relatively small, at least for the root section at 30.0%.

Figure 3.6 shows the aerodynamic coefficients from the non-rotating measurements, but now obtained after correcting for the induced velocity as modelled in the program *inflow*. In this calculation also a correction for the 'virtual camber' (dealing with the flow curvature and the finite chord) is applied. The lift curves already show a more realistic slope while for the 46.6%, 63.3%, and 80.0% sections they are close to each other. The deviating coefficients for the root

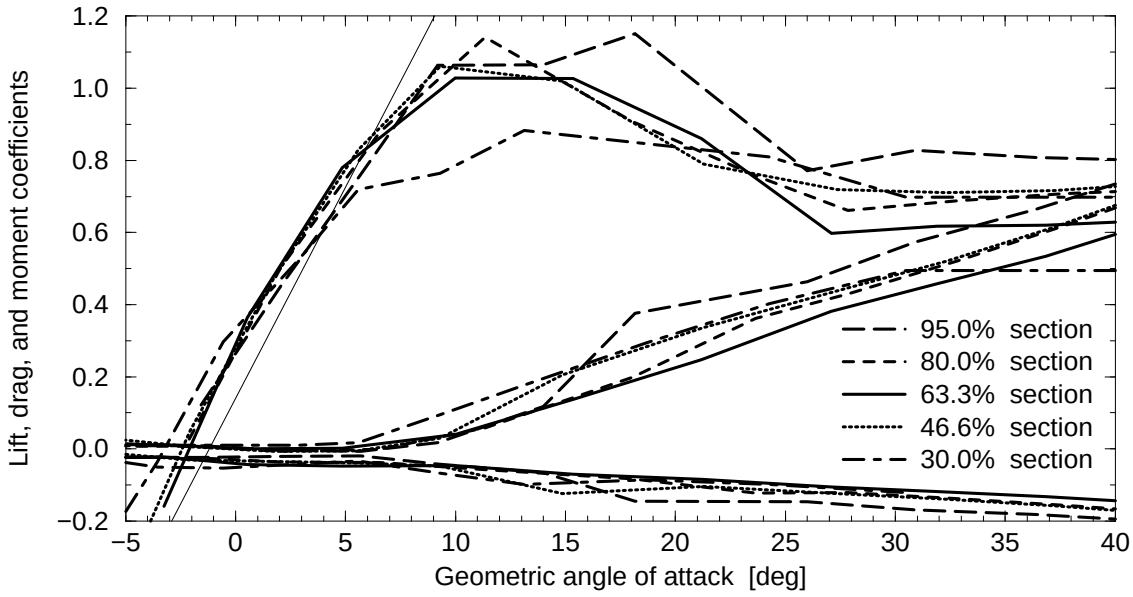

Figure 3.6 *Non-rotating aerodynamic coefficients with induced velocity*

and the tip section may be a result from radial flow components, which are not included in the 2D aerodynamic coefficients. In Figure 3.6 the zero-lift angle-of-attack still shows an off-set compared to the -1.2deg that was found in the 2D wind-tunnel tests at Delft and the numerical analyses by Bernadett and van Dam. Also the 'laminar drag bucket' shows to have a 'banked bottom'. For an angle-of-attack near 5deg, the drag coefficients even become slightly negative.

After some investigations it was found that applying a 1.0deg reduction on the blade pitch angle of the measurements, results in both a horizontal 'laminar drag bucket' and a zero-lift angle of about -1.2deg. The resulting aerodynamic coefficients are shown in Figure 3.7.

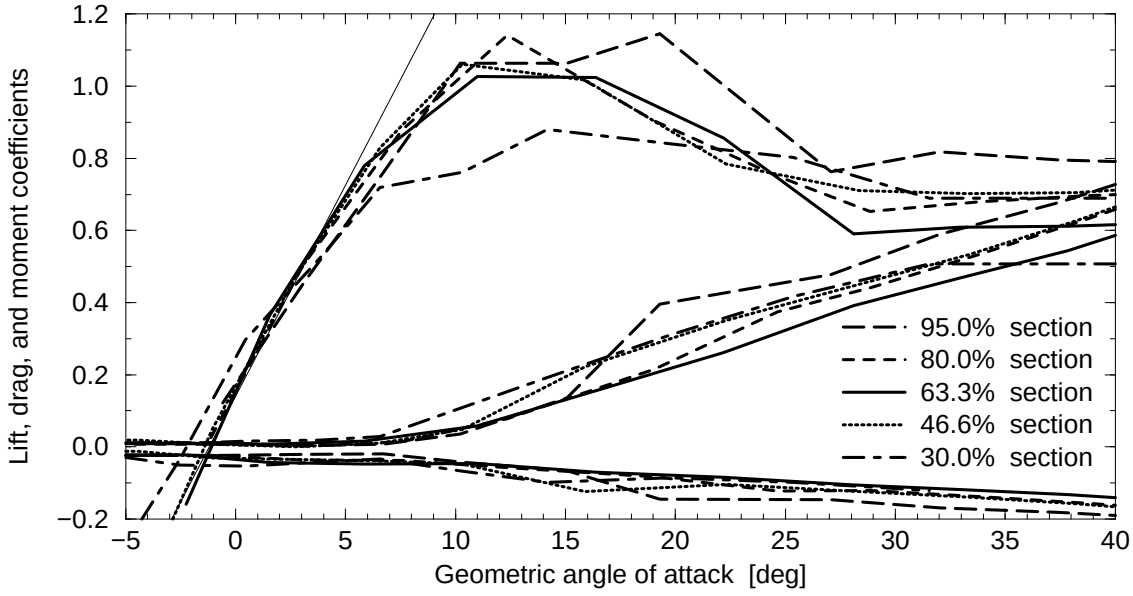

Figure 3.7 *Non-rotating aero. coeff with induced velocity and a -1.0deg pitch correction*

A comparison of the aerodynamic coefficients with and without the 1.0deg pitch angle correction is given in Figure 3.8, for the 'ramp-down' pitch sweeps at 30m/s. Without the pitch-angle correction, the laminar drag bucket is a little banked and has slightly (local) negative drag values. In Figure 3.8 only the coefficients of the middle section at 63.3% are shown. For each of the

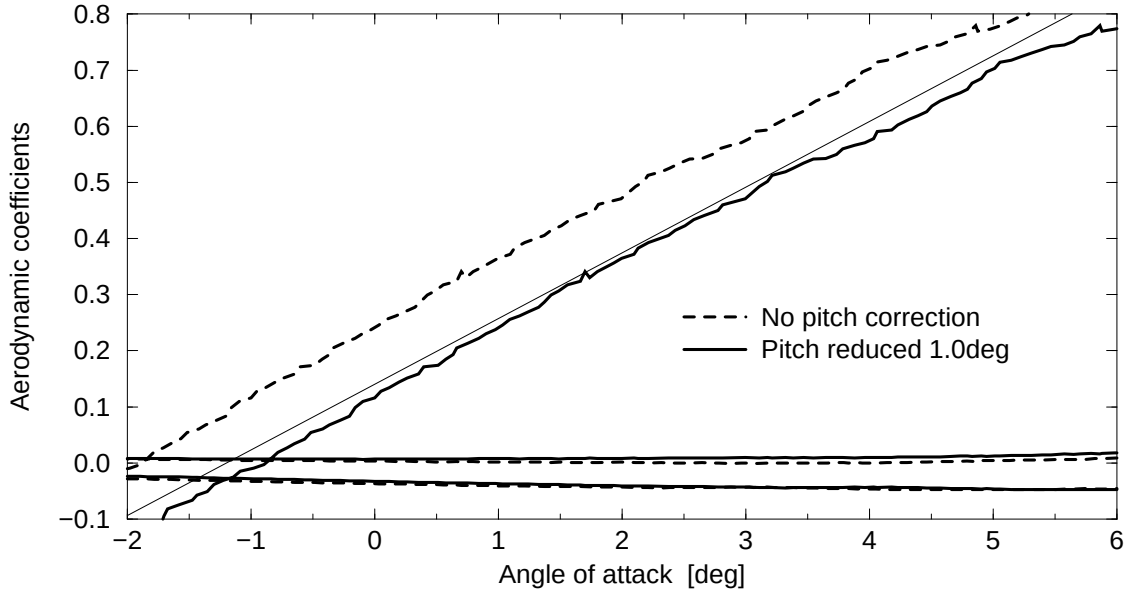

Figure 3.8 *Non-rotating aero. coeff at 63.3% with induced velocity and pitch correction*

instrumented sections Figure 3.9 through 3.13 give the aerodynamic coefficients obtained with the tool *inflow*, including the -1.0deg pitch correction.

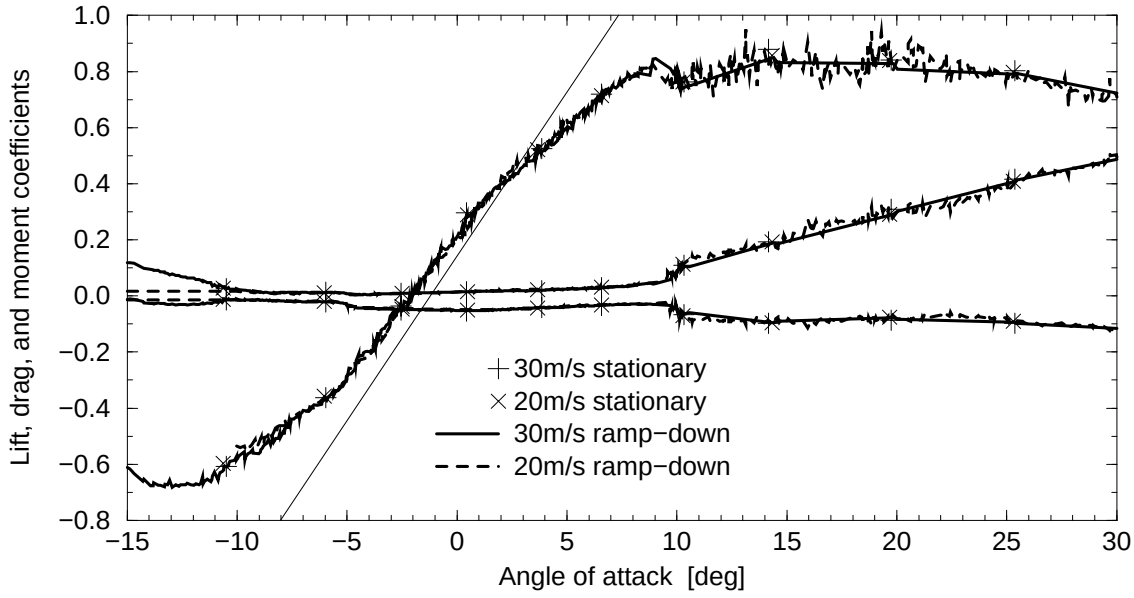

Figure 3.9 *Reconstructed aerodynamic coefficients for the 30.0% section*

The Figures 3.9 through 3.13 show that the coefficients retrieved from the measurements with stationary pitch angle and with 'ramp-down' pitch sweeps are nearly identical, except for small differences near maximum lift for the 46.6% section. The coefficients from the 20m/s measurements and the 30m/s measurements are also nearly identical except for the transition to deep-stall, see the 46.6% and 95.0% section: Figure 3.10 and 3.13. The difference in the deep-stall transition is most likely a Reynolds number related phenomenon.

Figure 3.10, 3.11, and 3.12 show that the coefficients for the 46.6%, the 63.3% and the 80.0% section are nearly identical. Although the lift curves from the measured data all show a maximum of about 1.1, the shape of this maximum is not completely similar to the shape of the lift-curve from the TU-Delft measurements.

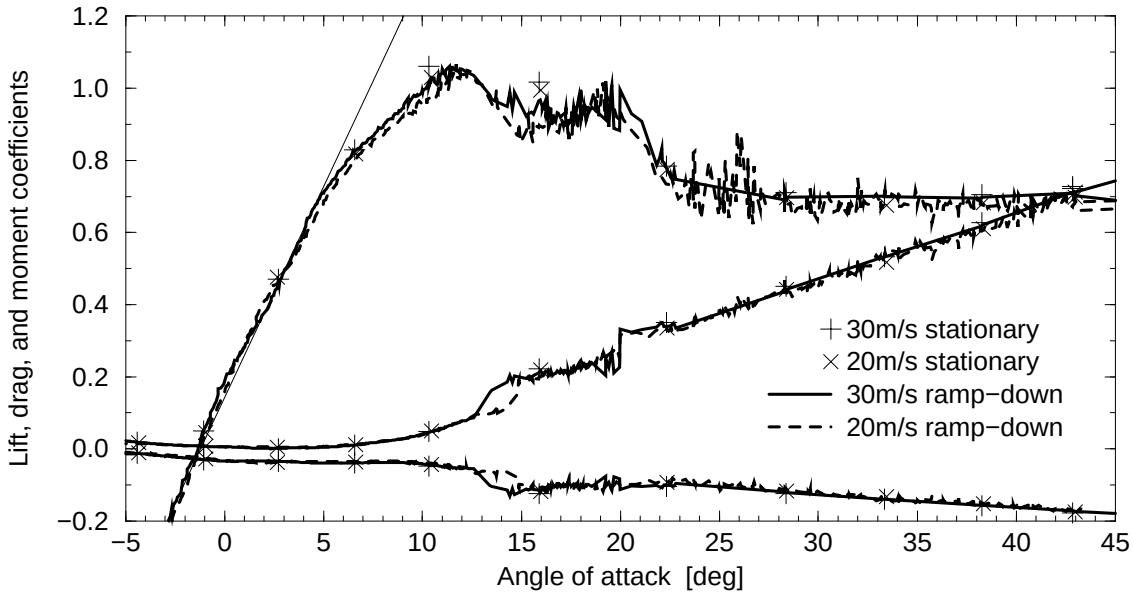

Figure 3.10 *Reconstructed aerodynamic coefficients for the 46.6% section*

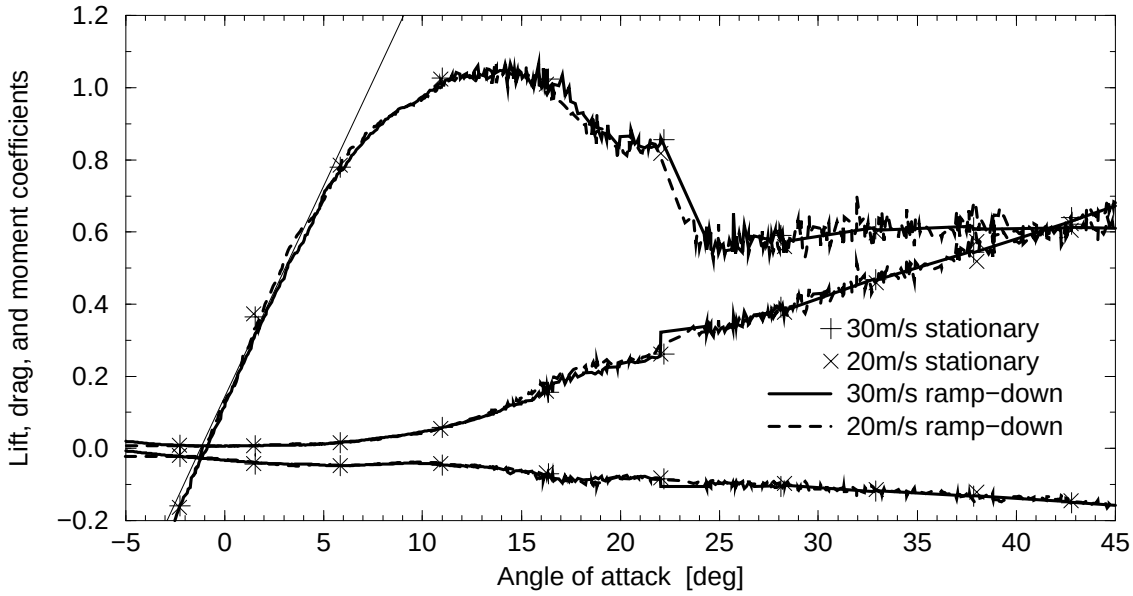

Figure 3.11 *Reconstructed aerodynamic coefficients for the 63.3% section*

The necessity of a pitch correction may be caused by a local deviation of the wind direction in the tunnel w.r.t. the UAE rotor or an error in the yaw angle. It may also be caused by the discretisation error of the integration of the normal-force and tangential-force coefficients from the finite number of pressure taps. On basis of the zero-lift angle-of-attack the pitch angle correction could have been slightly smaller, e.g. -0.9deg, in particular for the 63.3% section. However, with a -1.0deg pitch-angle correction the laminar drag bucket is horizontal.

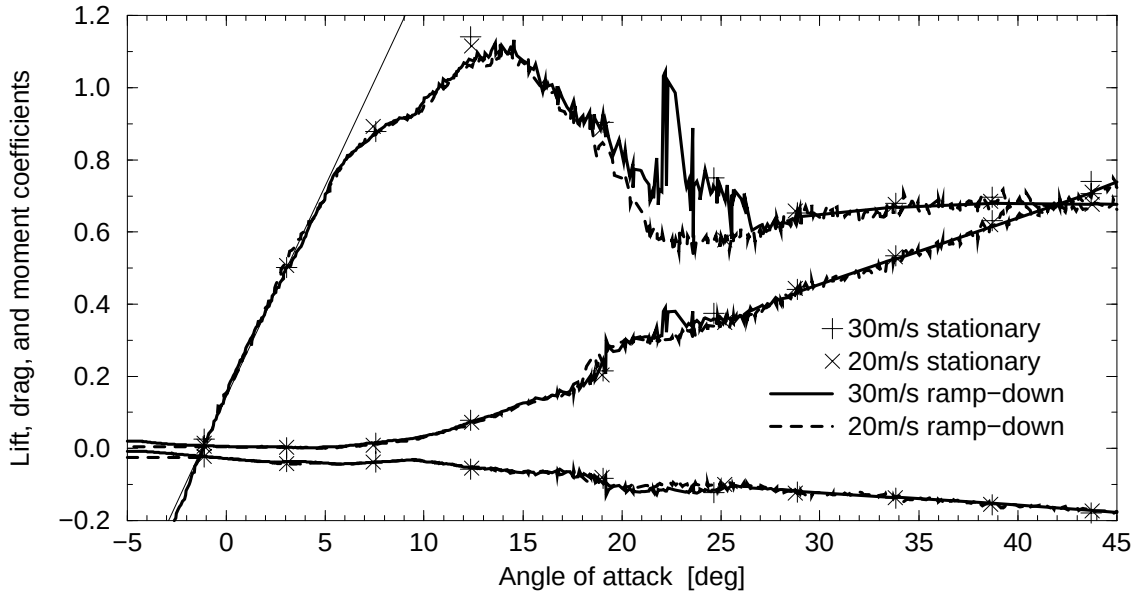

Figure 3.12 *Reconstructed aerodynamic coefficients for the 80.0% section*

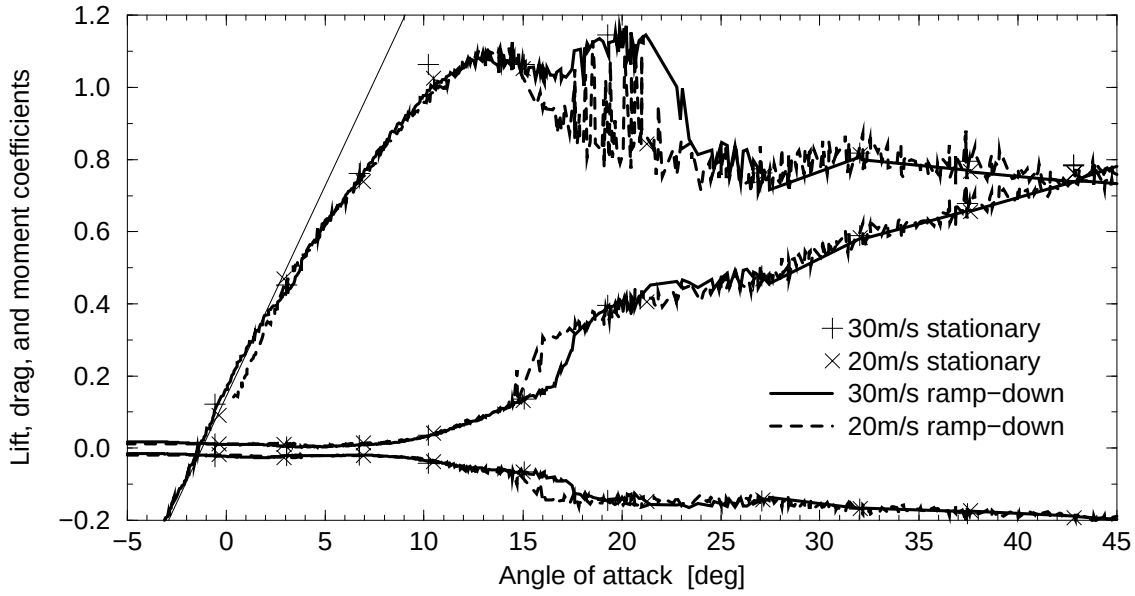

Figure 3.13 *Reconstructed aerodynamic coefficients for the 95.0% section*

3.3.1 Comparison of aerodynamic coefficients

Following is a comparison of some characteristic values of the aerodynamic coefficients from the different sources. The values from the method of Pankhurst are for the 'smoothed' trailing-edge.

Source	Re_c	α_{zerolift}	c_{mom}	$\partial c_l/\partial\alpha$	1st $c_{l\,\max}$	2nd $c_{l\,\max}$
Thin airfoil theory, Pankhurst		-1.30deg	-0.047			
Eppler code, Somers	$1\cdot10^6$	-1.50deg	-0.0545	0.11		
Navier-Stokes, Zhang et al.	$1\cdot10^6$	-1.2deg		0.09		1.02
MSES, Bernadett & v. Dam	$1\cdot10^6$	-1.21deg	-0.0425	0.118	0.965	0.998
TU-Delft measurements	$1\cdot10^6$	-1.18deg	-0.0435	0.116	0.973	1.062
OSU measurements	$1\cdot10^6$	-0.64deg	-0.0356	0.117	0.94	1.03
CSU measurements	$0.65\cdot10^6$	-0.994deg		0.0995	0.892	0.928
NASA-Ames data at 46.6%	$0.85\cdot10^6$	-1.34deg	-0.0337	0.108	1.05	
NASA-Ames data at 63.3%	$0.94\cdot10^6$	-0.90deg	-0.0326	0.121	1.05	
NASA-Ames data at 80.0%	$0.97\cdot10^6$	-1.15deg	-0.0279	0.120	1.10	
Calc. Yang, Chang, Arici	$2\cdot10^6$	-0.47deg		0.107		1.29
Calc. Dini, Coiro, Bertolucci	$2\cdot10^6$	-1.14deg		0.116		1.18
Calc. Wolfe & Ochs, turbul.	$2\cdot10^6$	-1.15deg		0.113		
Calc. Wolfe & Ochs, mixed	$2\cdot10^6$	-1.32deg		0.117		
TU-Delft measurements	$2\cdot10^6$	-1.201deg	-0.0443	0.120		1.1104

The NASA-Ames data were from the 'ramp-down' measurements at 30m/s wind including the -1.0deg pitch angle correction, of which the Reynolds numbers are listed for operation at 10m/s wind velocity (where the rotor starts to stall). If follows here that a 'pitch correction' of -0.9deg would also be realistic. The moment coefficients are the values for a zero angle of attack, and the slope of the lift curves was calculated from -1deg to 3deg. In this table the '1-st' maximum lift coefficient is for α near 9deg and the '2-nd' maximum for α near 14deg.

The aerodynamic coefficients calculated by Bernadett & van Dam, the 2D coefficients measured in the TU-Delft wind tunnel and the coefficients reconstructed from the non-rotating UAE measurements are plotted in Figure 3.14.

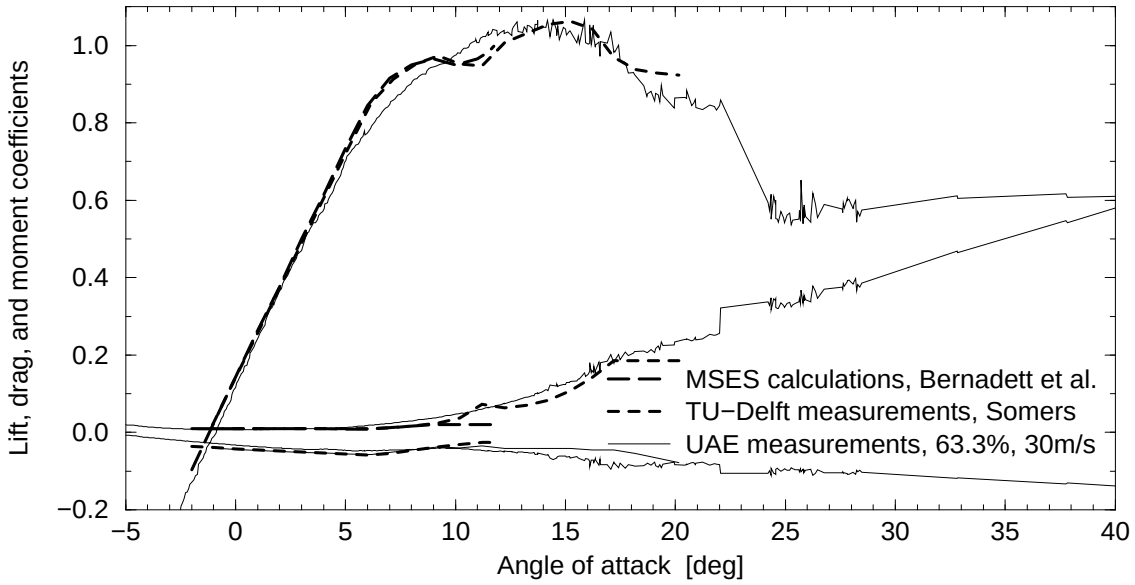

Figure 3.14 *Comparison of aerodynamic coefficients for the 63.3% section*

The coefficients reconstructed from the UAE measurements were for a tunnel wind speed of 30m/s and for the 63.3% section, for which the Reynolds number is close to $1\cdot10^6$. For the UAE coefficients the -1.0deg pitch correction was applied. The measurements in the TU-Delft wind

tunnel and the calculations with MSES correspond well except for an under-estimation of the drag coefficients from MSES for larger angles-of-attack. The aerodynamic coefficients reconstructed from the non-rotating UAE measurements do not show the first maximum.

3.3.2 Estimated coefficients in deep stall

With the improved program *StC* , see chapter 2, the aerodynamic coefficients of the S809 airfoil were calculated for the deep stall conditions. The geometry parameters used by *StC* were a leading edge radius of 0.00876, and trailing-edge angles of 7.6047deg and -3.9622deg for the upper and lower side respectively. The negative trailing-edge angle for the lower side indicates a concave surface or 'cusp', see Figure 3.2. The aspect ratio of the blade was 7. The deep-stall coefficients estimated with *StC* are compared in Figure 3.15 with the coefficients reconstructed with *inflow* for the 63.3% section, and with the coefficients measured in the CSU wind tunnel (2D, and Re = $0.65 \cdot 10^6$). Figure 3.15 shows that the coefficients estimated with *StC* are slightly higher

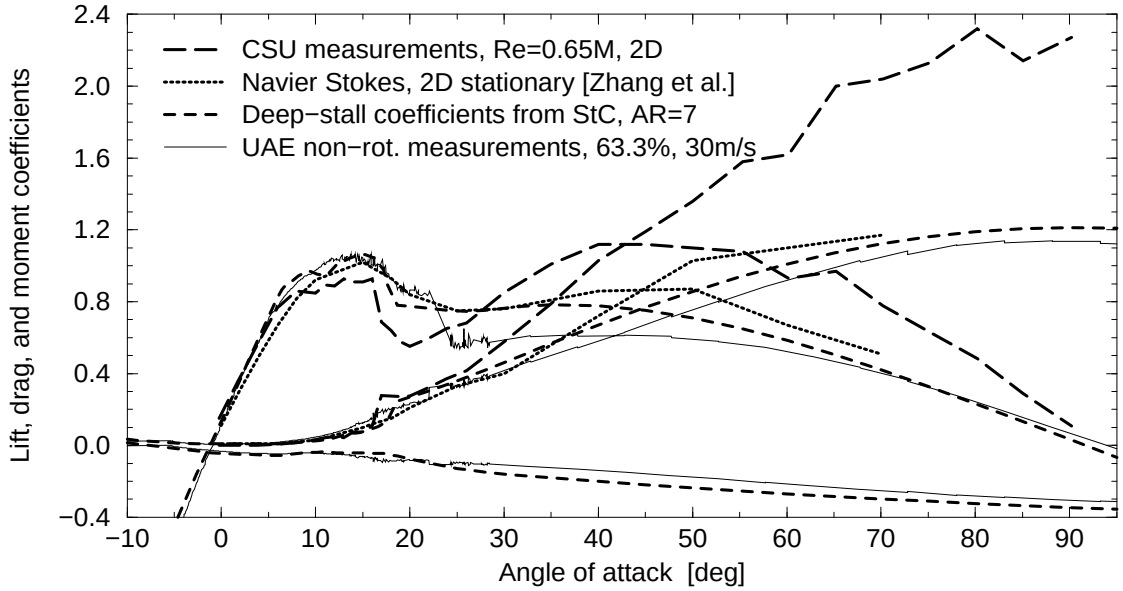

Figure 3.15 *Measured and empirical aerodynamic coefficients in deep stall*

(conservative for the design loads) compared with the data from the UAE measurements, while they are still smaller than the 2D coefficients measured in the CSU wind tunnel.

3.4 Non-rotating Aerodynamic Coefficients for the S809 Airfoil

For the comparison of the calculations with PHATAS and the measurements on the UAE phase-VI rotor in the NASA-Ames wind tunnel, a table with stationary aerodynamic coefficients has to be defined. For the Blind Comparison that was organised in the fall of 2000, these coefficients have been compiled from the measurements in the TU-Delft wind tunnel and those in the Ohio State University wind tunnel.

The measurements in the TU-Delft wind tunnel were considered as the most representative, which also follows from comparison with the coefficients calculated with the MSES code, see Figure 3.3 and 3.4. Because the measurements in the TU-Delft wind tunnel were for an angle-of-attack range from -2.63deg to 17.21deg, the coefficients for other angles-of-attack were taken from the OSU measurements. Following the recommendations of Nando Timmer (e-mail of Nov. 6, 2000, [81]) the angle-of-attack of the OSU coefficients were reduced with 0.53deg. The resulting set of aerodynamic coefficients range from -16.73deg to 18.67deg. Using the improved version of the tool *StC* , see chapter 2, the aerodynamic coefficients were extended to the -180deg to +180 range for an aspect ratio of 7, see Figure 3.16. The empirical deep-stall coefficients from *StC* were splined to the measured coefficients with 3-rd order polynomial functions over an interval of 10deg.

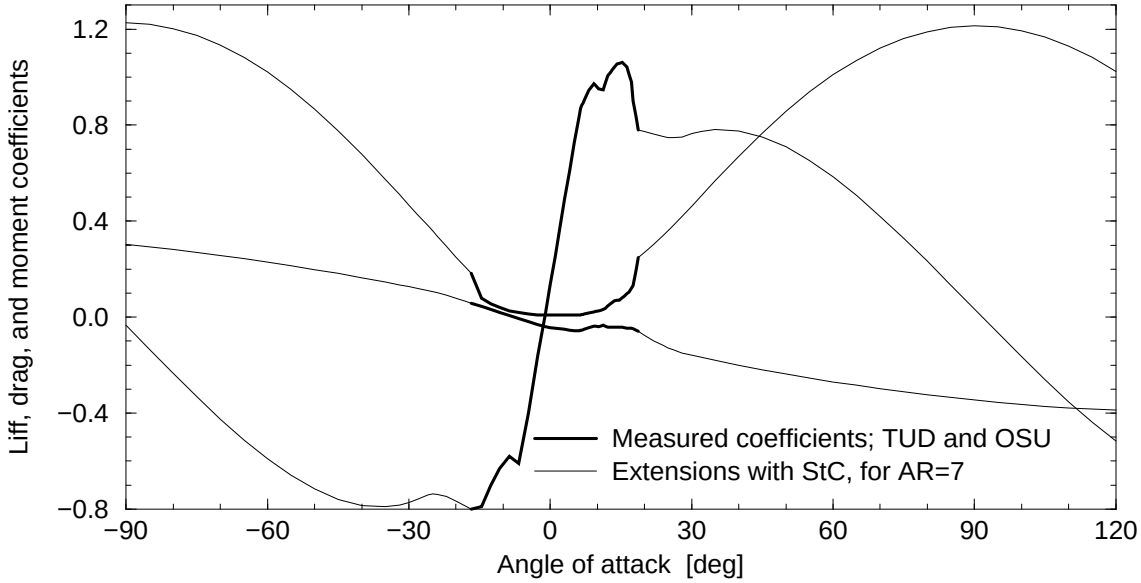

Figure 3.16 *Aerodynamic coefficients compiled for calculations with PHATAS*

For an angle-of-attack near 18deg, the lift coefficients from the OSU wind tunnel show drastic (leading-edge) stall with an increase in drag. In this region, the choice where to use the measured data and where to add the empirical coefficients is a conscious and difficult task.

The resulting aerodynamic coefficients for the S809 airfoil look realistic, except for the lift curve between -20deg and -7deg. For the conditions of the NASA-Ames measurements however, the airfoil will not operate in this angle-of-attack range. A listing of the aerodynamic coefficients for the S809 airfoil is given in appendix A.

4. ROTATIONAL EFFECTS ON THE AERODYNAMIC COEFFICIENTS

4.1 Introduction

For aircraft, Himmelskamp [33] investigated the increased (maximum) lift coefficients of rotating propeller blades which he addressed to the occurrence of radial flow. This increase in maximum lift is the strongest for the smaller radial sections while it was found that stall occurs at larger angles of attack than for the non-rotating state.

The effects of rotation has also been investigated intensively for helicopter rotors. These investigations also deal with the local oblique inflow of the rotor blades in forward flight, see e.g. Harris [32]. In the publication of Harris, the effects of rotation are modelled similar as a blade operating in yawed flow. Harris reported that in addition to the conventional approach of calculating the aerodynamics with the flow component normal to the blade axis, also the maximum lift increases slightly with a oblique inflow inflow. Fundamental aspects of the stalled flow area in oblique inflow is that the axis of vorticity is not perpendicular to the local flow direction and that the separation area is transported in spanwise direction. For helicopters in forward flight Dwyer & McCroskey [21] gave a description of the effect of 'crossflow' on the rotor blades.

For the early stall-controlled wind turbines it had been noticed in he past that the aerodynamic power tends to exceed the design value, which since then became a design item. For the description of the rotational effects or 'stall delay' several models have been formulated, most of which are in terms of a correction to be added to the non-rotating lift coefficient. A few of these models also describe a correction (increase) on the drag coefficient. Some correction models for rotational effects are based on the mechanism of centrifugal pumping of air in the trailing-edge separation bubble. One of the first calculation models for wind turbines that included the effects of rotation was described by Sørensen in [74]. In the publication of his work, Sørensen showed flow fields with radial-flow patterns in the trailing-edge separation area. This was supported by later numerical investigations for the S809 airfoil [75], which clearly show 'centrifugal pumping' near the trailing edge. Later Eggers & Digumarthi [22] compared a model for rotational augmentation with measurements on the UAE Phase-II rotor.

4.2 Effects of Rotation on the Airfoil Aerodynamics

4.2.1 Effect on laminar separation bubbles

In the cylindrical coordinate system attached to the rotating blade, the centrifugal loads act on all volumes of air of which the relative tangential velocity differs from Ωr . This includes the inner boundary layer, the (laminar) separation bubbles, and the turbulent separation at the trailing edge. The centrifugal loads on the boundary layer and the laminar separation bubbles accelerate the flow towards larger radial locations. In a rotating system, the air with radial velocity has a Coriolis acceleration towards the leading edge that has to be in equilibrium with the chordwise pressure gradient. If this pressure gradient is insufficient or absent the air with radial flow (in the separation bubble) tends to move towards the trailing edge.

As a result of this mechanism the boundary layer moves slightly outboard and is less thick and more "stable" compared to the non-rotating state. Finally separation bubbles may not occur at all, which is also indicated by the large leading-edge suction peaks measured by Barnsley and Wellicome [6]. The 'delay' or 'absence' of leading edge stall is also shown by Butterfield for the 80.0% section of the phase-II rotor (Figure 3 of [11]) giving a nearly constant rotating lift coefficient for the S809 airfoil, for angles of-attack where the non-rotating coefficients show a pronounced stall.

In [54] D. Milborrow reported on the conclusions by Harris [32] that '*Most have suggested that stall is likely to be delayed by radial flows but few have attempted to analyse the turbulent boundary layer, and none appear to have quantified the magnitude of the increased lift*'.

This means that depending on the airfoil, the aerodynamic coefficients first need to be found/corrected without formation of laminar separation bubbles so that the coefficients for leading edge stall have to be replaced by coefficients for trailing edge stall. This difficult task may be done using data from other airfoils with a similar after-body. Next a correction for the 'centrifugal pumping' mechanism may be applied, see the next subsection. Such an approach has been applied by Björn Montgomerie for the 'Blind Comparison' organised by NREL, see chapter 6. Montgomerie replaced the post-stall lift coefficients by constant values after instead of trailing edge stall coefficients. The correction for 'centrifugal pumping' effects that was added next, unfortunately led to rather high lift coefficients and also a high power. Montgomerie has shown to be aware of the difficulties of using correction methods for airfoils with leading-edge stall.

4.2.2 Centrifugal pumping mechanism

The centrifugal loads on the separated volume of air near the trailing edge causes radial flow. A direct result is that the volume of the separation bubble is smaller than without the centrifugal loads. Because of the span-wise gradient of the centrifugal loads, the pressure in the separated volume is smaller, which gives an increased normal force on the airfoil.

At larger angles of attack, the chord-wise pressure distribution on the suction side of an airfoil has a large suction peak just aft of the leading edge that decreases towards the trailing edge. The magnitude of this suction peak is proportional to the 'dynamic pressure' and thus increases with the radial location squared. The span-wise gradient of the dynamic pressure and the chord-wise gradient of the negative pressure on the airfoil provide a mechanism by which the air in the separated area flows to larger radial locations and can overcome the Coriolis-loads. Klimas [40] described radial flow based on the Euler-equations including the centrifugal and Coriolis-effects on the flow in the trailing-edge separation bubble.

Following Eggers & Digumarthi [22] and other authors this mechanism will be called 'centrifugal pumping' in the remainder of this report. It has also been reported as 'radial pumping' (Sørensen e.a. [75]) or 'spanwise pumping' (Harris [32]). A model based on the equations for 'centrifugal pumping' is described in section 4.3.

4.2.3 Shift in angle of attack

The 'centrifugal pumping' effect on the separated volume of air near the trailing-edge, gives an additional negative pressure on the airfoil-surface. This additional negative pressure gives a negative chordwise pressure gradient which is favourable for the stability of the boundary layer, and may therefore lead to a shift of the separation point towards the trailing edge. This shift in separation point is hard to model.

Instead, one may start with assuming that the same location of the separation point occurs for a larger angle-of-attack such that the chordwise pressure gradient, including the effect of the rotational augmentation, is the same as for the non-rotating state. On basis of this relation, correction models can be derived for the shift ("delay") in angle-of-attack. Related to this "shift" in angle-of-attack, the lift coefficient has to be scaled such that is has the same ratio between the curve for fully attached potential flow, and the curve for complete separation.

The observations by Himmelskamp also reported as if stall of the lift coefficients is delayed to larger angles of attack, although no delay was observed for the the rise in drag coefficient.

Some models for the rotational effects are formulated in terms of 'stall delay', such as the method of Corrigan & Schillings [14], see section 4.5. The method of Corrigan & Schillings has been investigated by Tangler & Selig [77] for constant-chord and tapered rotor blades with S809 airfoils.

4.2.4 Rotational effects on sectional drag

Many of the models that describe rotational augmentation in terms of delay of stall to larger angles-of-attack, inherently give give a reduction of the aerodynamic drag coefficients. In the introduction of [54], Milborrow reports on the observations of Viterna & Janetske [83] on basis of power measurements that the drag appears to be reduced, while Himmelskamp [33] found an increased drag on basis of chordwise pressure distributions. In [54] Milborrow concluded with the expectation of an increased drag. The empirical model for 'stall-delay' of Du & Selig [18] however describe a reduction of the drag coefficient. The measurements on the UAE phase-VI rotor in the NASA-Ames windtunnel finally give a serious increase of the aerodynamic drag coefficient.

It follows that there is no full consensus on what happens with the aerodynamic drag coefficient. Knowing that the rotating sectional coefficients show a strong (local) increase towards the root and a strong (local) decrease towards the tip that deviate from most correction models (section 4.7), the rotor shaft torque can not (yet) be used as complete basis for estimation/evaluation of the rotating drag coefficients. This leaves the (less accurate) chordwise pressure distributions as basis for modelling rotating drag coefficients. Based on this together with the fact that 'centrifugal pumping' adds energy to the flow one may conclude that the aerodynamic drag coefficient increases due to the effects of rotation. However, these facts do not exclude other mechanisms that describe a reduction in drag coefficient. The observations of an increased aerodynamic drag coefficient may be an indication that not the lift but the normal-force coefficient has to be increased, such as in the model described in section 4.3.

When using measurements as basis for modelling, one must be aware of the accuracy of the data, which was also stated by Milborrow in the first conclusion of [54]. This holds in particular for the drag coefficient because measurements from pressure-taps are already inaccurate while the resulting drag coefficient is very sensitive to small errors in the measured sectional angle-of-attack.

4.3 Correction Model Based on Centrifugal Pumping

The model described here is based on the effects of trailing-edge stall for which state the rotor acts as a centrifugal pump on the separated volume of air. For leading-edge separation bubbles it was already mentioned that due to rotational effects they will probably not occur at all, which is hard to model. The effect of rotation on trailing-edge stall however can be derived relatively easy because the area of 'separated flow' extends from the separation point to the trailing edge.

For 'attached flow' the pressure distribution over the airfoil surface is proportional to the dynamic pressure of the relative airflow on the blade section. Because the trailing-edge side of the separated area of flow has a pressure that is close to the atmospheric pressure, the pressure from chordwise flow in this area has only a small spanwise gradient. This means that the separated volume of flow is subjected to a dominant 'centrifugal loading' (a loading that appears if one works in a rotating coordinate system) that is proportional to the radial location of the section. Assuming that trailing-edge stall appears over a large spanwise area of the blade, one can derive that the 'centrifugal loads' result in a radial velocity v_{rad} that is proportional to (theoretically equal to) the tangential velocity: $v_{\mathrm{rad}} = \Omega\, r$.

If the separated area with radial flow follows the blade angular velocity $\Omega\, r$ it needs a Coriolis-acceleration that is proportional to $2\, v_{\mathrm{rad}}\, \Omega\, \cos(\theta_{\mathrm{tw}} + \theta_{\mathrm{p}}) = 2\, \Omega^2\, r\, \cos(\theta_{\mathrm{tw}} + \theta_{\mathrm{p}})$.
The term $\cos(\theta_{\mathrm{tw}} + \theta_{\mathrm{p}})$ is for the component of the Coriolis-effects in the chordwise direction. The cosine of this angle is approximated by 1 because:

- In fact one should use the component of the Coriolis-effects in the direction of the upper surface of the trailing-edge of the airfoil, which is airfoil-dependent;
- The cosine of this direction differs significant from 1 if the sum $(\theta_{\mathrm{tw}} + \theta_{\mathrm{p}})$ is large for which case either the airfoil is not in stall (small a.o.a.), or the local speed ratio is small which approaches the non-rotating conditions.

Adding the cosine of the direction $(\theta_{\mathrm{tw}} + \theta_{\mathrm{p}})$ does not give much different results because, as will be shown later, the end-effects near the blade root and blade tip are dominating for the discrepancy between theoretical models and the measured aerodynamic loads.

If the chordwise dimension of the trailing-edge separation area is expressed in the dimensionless separation parameter f: $size = c\,(1 - f)$ and assuming that the additional sectional load is proportional to this size, then the negative pressure on the suction side of the airfoil due to the Coriolis-accelerations gives an additional normal force on the airfoil that is proportional to:
$f_{\mathrm{n.rot}} - f_{\mathrm{n.non-rot}} = factor\ \rho\, c\, (1 - f)\, 2\, \Omega^2\, r$. where $factor$ is used for scaling of the correction. One may even consider that the total additional suction force is proportional to $(1 - f)^2$.

Following common practice to make the sectional aerodynamic loads dimensionless with $(\rho/2)\,((\Omega\, r)^2 + (U_{\mathrm{wind}} - U_{\mathrm{i}})^2)$ (Here U_{i} and V_{i} are the axial and tangential induced velocity.) gives for the increase in the dimensionless normal-force coefficient:

$$c_{\mathrm{n.rot}} - c_{\mathrm{n.non-rot}} = factor\ c\,(1 - f)\,\Omega^2\, r/((U_{\mathrm{wind}} - U_{\mathrm{i}})^2 + (\Omega\, r + V_{\mathrm{i}})^2)\,.$$

Because this derivation is addressed to the rotating state, the tangential induced velocity V_{i} can be omitted with respect to the rotational velocity $\Omega\, r$, which gives the expression for the increase in normal force coefficient:

$$c_{\mathrm{n.rot}} - c_{\mathrm{n.non-rot}} = 1.5\,(\frac{c}{r})\,(1 - f)\,(\Omega\, r/V_{\mathrm{eff}})^2 = 1.5\,(\frac{c}{r})\,(1 - f)\,(\Omega\, r/V_{\mathrm{eff}})^2\ .$$

The term $(\Omega\, r/V_{\mathrm{eff}})^2$ can be approximated (for $V_{\mathrm{i}} < \Omega\, r$) with the local speed ratio $\lambda_{\mathrm{r}}^2/(1 + \lambda_{\mathrm{r}}^2)$ with $\lambda_{\mathrm{r}} = \Omega\, r/(U_{\mathrm{wind}} - U_{\mathrm{i}})$. This rotor-speed dependency can also be expressed in the local inflow angle, and approaches zero for small values of λ_{r} (as for idling) and approaches 1 for λ_{r} larger than 1. The 'scaling' factor 1.5 results from fitting with the measured shaft torque of the UAE phase-VI rotor used for the Blind Comparison, see chapter 6.

The relation for trailing-edge separation f following the Kirchhoff/Helmholtz model (see also p.252 of [42] by Leishman) for the normal force coefficient is $c_{\mathrm{n}} = \partial c_{\mathrm{n.0}}/\partial\alpha \cdot \left((1+\sqrt{f})/2\right)^2 \cdot (\alpha - \alpha_0)$. Here the subscript '0' denotes the state (angle of attack) for zero lift.

The more negative pressure in the separation area also gives a 'delay' of the stall phenomenon to larger angles of attack. This shift in angle-of-attack due to rotation was modelled with the same function as for the rotating normal-force coefficient:

$$\alpha_{\mathrm{rot}} = \alpha_{\mathrm{non-rot}} + 0.3\mathrm{rad}/(2\,\pi) \cdot 1.5 \cdot (1-f) \cdot (c/r) \cdot (\Omega\, r/V_{\mathrm{eff}})^2 \ .$$

Here the factor $0.3\mathrm{rad}$ is an additional empirical scaling factor. The value $0.3\mathrm{rad}$ was based on the measurements on the UAE phase-VI rotor only so that it is recommended to fit this on basis of more measurements. Here the difficulty is that the scaling of the shift in angle-of-attack relies heavily on the increase of the drag coefficient, which requires accurate measurements of the tangential-force distribution and an accurate tool to reconstruct the inflow angle. For this reason effort is paid on a proper functioning of the tool *inflow* described in Appendix B.

The increase in lift and drag coefficient are the $\cos\alpha_{\mathrm{rot}}$ and the $\sin\alpha_{\mathrm{rot}}$ components of the increase in normal force coefficient:

$$c_{\mathrm{l.rot}} = c_{\mathrm{l.non-rot}} + 1.5 \cdot (\cos\alpha_{\mathrm{rot}} + 0.3\,\cos(\alpha_{\mathrm{rot}} - \alpha_{(\mathrm{Cl}=0)}) \cdot (1-f) \cdot (c/r) \cdot (\Omega\, r/V_{\mathrm{eff}})^2 \ .$$

$$c_{\mathrm{d.rot}} = c_{\mathrm{d.non-rot}} + 1.5 \cdot \sin\alpha_{\mathrm{rot}} \cdot (1-f) \cdot (c/r) \cdot (\Omega\, r/V_{\mathrm{eff}})^2 \ . \qquad (4.1)$$

In addition to the dependency of the speed ratio, major differences compared to other models are:
- An increase of the normal force coefficient instead of the lift coefficient;
- A shift in angle-of-attack that is related with the increase of the coefficients;
- A dependency of the chordwise dimension of T.E. separation bubble;
- A linear dependency of (c/r) instead of an empirical fit.

Basically the aerodynamic drag for the rotating state has a contribution from the fact that tangential momentum is fed to the separated volume of air with radial flow. It has not yet been investigated whether a term for the tangential momentum of the radial flow has to be added.

The major assumptions behind the model presented here are:
- Stall takes place at the trailing edge;
- The pressure in the separated air volume is roughly constant such that finally the radial velocity is proportional to the local radius;
- For the rotational conditions where the angle-of-attack is large the aerodynamic suction side of the airfoil is nearly in the plane of rotation.

Other correction models based on the mechanism of 'centrifugal pumping' are given by Corten [15] and by Chaviaropoulos [13], in terms of a correction on the lift coefficients.

4.4 ”3D-correction” of Snel, Houwink, and Bosschers

Snel, Houwink, and Bosschers derived a so-called ’3D correction’ method [71] that gives an increase of the aerodynamic lift coefficient for the effects of rotation. This derivation starts with the boundary-layer equations similar as have been reported by Banks & Gadd [5], and showed that the rotational effects are proportional to $(c/r)^{2/3}$. However, based on comparison with measurements their correction was finally formulated proportional to $(c/r)^2$:

$$c_{\mathrm{l,rot}} = c_{\mathrm{l,non-rot}} + 3.1 \cdot (c/r)^2 \cdot (c_{\mathrm{l,pot}} - c_{\mathrm{l,non-rot}}).$$

The factor 3.1 was used to fit with measurements. Discussions with H. Snel (March 2003) and comparison with measurements on the UAE rotor (see chapter 6) learned that this factor 3.1 could as well be reduced to 3. (while this also does not suggest a too high accuracy). Because it is known that the term $(c/r)^2$ is an empirical fit which gives a stronger dependency on (c/r) than what is found from theory, it was decided to maintain the factor 3.1, because the observations for the phase-VI rotor were for a relatively low aspect ratio compared to modern large rotor blades.

The conditions for application of the correction partly follow the recommendations of Snel e.a.:

Effect of local speed ratio Initial descriptions of correction-methods for the effects of rotation (also in the former PHATAS-III program) did not depend on the local speed ratio λ_{r}.
For aircraft propellers one was only interested in the performance during operation, so for reasonably high tip-speed ratio’s. For these applications, omission of the influence of the speed-ratio is fairly acceptable. For wind turbines however, the aerodynamic loads also have to be known for idling at strong wind, or for the calculation of the start procedures if the turbine must be self-starting. This is a rough approximation to avoid over-prediction of calculated loads for parked and for idling conditions. From the publication of Snel e.a. [71] it can be derived that the effects of rotation on the coefficients are proportional to
$(\Omega r)^2/V_{\mathrm{eff}}^2 = (\Omega r)^2/((U_{\mathrm{wind}} - U_{\mathrm{i}})^2 + (\Omega r + V_{\mathrm{i}})^2) \approx \lambda_{\mathrm{r}}{}^2/(1+\lambda_{\mathrm{r}}{}^2) = (\cos\phi_{\mathrm{inf}})^2$.
This means that for tip speed ratios with which wind turbines operate the rotational effects have their full value but they reduce rapidly to zero for a local speed ratio λ_{r} below 1.
This term is used in the programs BLADMODE and PHATAS, giving the final expression

$$c_{\mathrm{l,rot}} = c_{\mathrm{l,non-rot}} + 3.1 \cdot (\Omega r/V_{\mathrm{eff}})^2 \cdot (c/r)^2 \cdot (c_{\mathrm{l,pot}} - c_{\mathrm{l,non-rot}}) \,. \tag{4.2}$$

Maximum correction If the flow is completely laminar, the Kutta-Joukovsky condition gives a lift coefficient that is proportional to $2\,\pi\,\alpha$. Because the strongest effects of centrifugal and Coriolis-loads result in a full laminar flow, this gives a maximum to the rotating lift coefficients.

Spanwise area to apply a correction For a span-wise location larger than 80% of the tip radius, no correction is applied. in this respect it can be mentioned that investigations by Madsen [48] for a blade with aspect ratio of 9 and NACA63-2xx airfoils show that outboard of the 65% radius the maximum rotating lift coefficient is already smaller than the non-rotating lift coefficient. Towards the free end of the blade-tip the local pressure distribution on the blade surface decreases to the atmospheric pressure, because of the radial boundary-layer flow from the inboard sections. This gives a decrease of the aerodynamic coefficients, see section 4.6.

Angle-of-attack range for correction The correction is applied from the zero-lift angle-of-attack up to a 30deg angle-of-attack. From an angle-of-attack larger than 30deg the correction decreases linearly to zero at 50deg, see Figure 4.1 and 4.2. In former descriptions of the model of Snel et al. this ’end angle-of-attack’ was 45deg but was increased (March 2003) to 50deg on basis of calculations for the Blind Comparison, chapter 6.

4.5 Stall-Delay model of Corrigan and Schillings

Corrigan & Schillings [14] developed a correction model for the effects of rotation, formulated in terms of delay of stall coefficients to larger angles of attack.

The derivation of this method also starts with the boundary-layer equations published by Banks & Gadd [5]. Together with the expression for the velocity gradient in the boundary layer $\partial u/\partial z$ the amount of stall delay was related to the angular location of the separation point: θ_s. The formulation in terms of the angular location θ_s implies a dependency on the chord/radius ratio, similar as for other models.

A characteristic assumption of their model is that airfoils with a high non-rotating maximum lift can have a strong suction peak at the leading edge which gives a strong radial pressure gradient and thus a stronger outboard radial flow. For simplicity, the model of Corrigan & Schillings was finally formulated in the angular location of the trailing edge θ_{TE}. For not too large chord values, this can be approximated with (c/r).

The delay of stall is expressed with a shift in angle-of-attack for the non-rotating coefficients:

$$\Delta\alpha = (\alpha_{Cl.max} - \alpha_{Cl=0}) \cdot \left(\left(\frac{K\,\theta_{TE}}{0.136} \right)^n - 1 \right) . \qquad (4.3)$$

The value K describes the velocity gradient which fits to the universal relation: $c/r = 0.1517/K^{1.084}$.

For n = 0 this expression gives the non-rotating coefficients. Corrigan indicates that a value of n between 0.8 and 1.6 gives a good correlation with most data, and a value 1 gives good results for many cases. In the applications by Tangler & Selig [77] and by Xu & Sankar [87] $n = 1$ was used.

The table with non-rotating coefficients is shifted over this stall delay angle $\Delta\alpha$, where the lift coefficient is given an additional increase of: $c_{l,rot} = c_{l,non-rot(\alpha+\Delta\alpha)} + (\partial C_l/\partial\alpha)_{pot}\,\Delta\alpha$.
Here $(\partial C_l/\partial\alpha)_{pot}$ is the slope of the linear part of the lift curve for which Xu & Sankar [87] used 0.1 for the phase-VI rotor.

Comparison of correction methods

Figure 4.1 and 4.2 show the coefficients of the S809 airfoil obtained with the different correction models. For all coefficients the dependency of $(\Omega r/V_{eff})^2$ was approximated by $(\cos\phi_{inf})^2$, where ϕ_{inf} is the sum of the angle-of-attack, the local twist angle, and the 3.0deg pitch angle used for most of the NASA-Ames wind tunnel measurements.

For the correction of the S809 airfoil coefficients following the method of Corrigan & Schillings, the range $(\alpha_{Cl.max} - \alpha_{Cl=0})$ was determined at 10.4deg (the 1st maximum of c_l) while the slope of the lift-curve a was chosen at 0.1, similar as done by Xu et al. [87]. The c/r ratios of the 46.6% and 63.3% sections are 0.2676 and 0.1701, see appendix A. Without the term $(\Omega r/V_{eff})^2$ the shift in angle of attack ('stall delay') is thus 1.722deg and 1.304deg for the 46.6% and 63.3% section respectively.

The S809 airfoil has 2 maximum values of the lift coefficient with a 6deg difference in angle-of-attack, see section 3.3.1. For airfoils such as the S809, this implies that using the Corrigan & Schillings stall-delay correction depends strongly on the choice of the lift-maximum. For this reason this method is badly quantified for airfoils with a smooth maximum lift. This inaccuracy together with the fact that one has to chose a value for the exponent n requires some insight in the amount of rotational augmentation for a realistic correction of the S809 coefficients.

The choice of the 1st maximum c_l for the PHATAS calculations reported in section 6.3.4, was made because for its conservatism compared to other correction methods and compared to measurements. On basis of the results in section 6.3.4 one may also consider to use the 2nd maximum c_l.

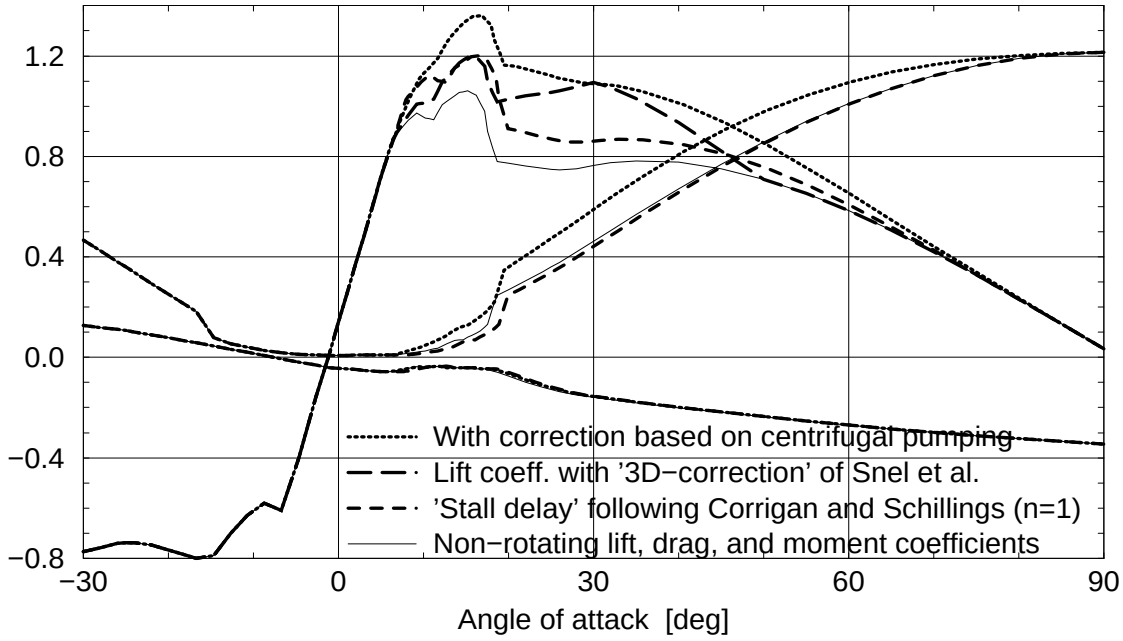

Figure 4.1 *Rotating aerodynamic coefficients of S809 at 46.6%, c/r = 0.2676,* $\theta_{tw}+\theta_p$ *= 9.49deg*

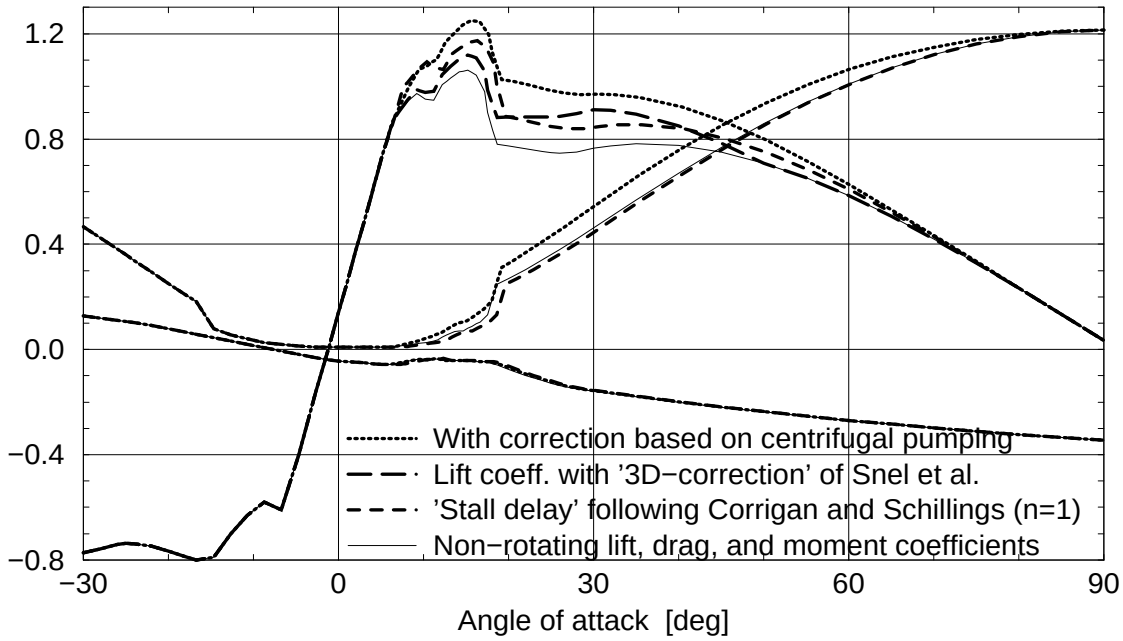

Figure 4.2 *Rotating aerodynamic coefficients of S809 at 63.3%, c/r = 0.1701,* $\theta_{tw}+\theta_p$ *= 5.89deg*

4.6 Reduction of Rotating Sectional Coefficients near the Tip

Most methods for the prediction of the aerodynamic coefficients of a rotating airfoil are theoretical/empirical expressions for the flow of the boundary layer and/or the trailing-edge separation area. Most of these theoretical backgrounds are based on a continuous increase of the dynamic pressure and centrifugal and Coriolis-effects with radial location, and likewise a continuous radial flow. For the blade tip area, the radial 'suction' from the centrifugal effects and the spanwise gradient of dynamic pressure reduce near the blade tip are ending. This means that the radial flow in the boundary layer and in the trailing-edge separation area is not driven or 'pumped' further than the blade tip region. This radial flow from the midspan of the blade results in a reduction of the negative pressure on the airfoil suction side, compared to the non-rotating case. The result is that the rotating lift coefficients of the tip sections are smaller than the non-rotating coefficients, while the flow is still *not in stall*.

It should be stressed that this reduction of the aerodynamic coefficients is of a different nature than the reduction in angle of attack due to the flow around the blade tip. The latter can be described with the tip-vortex, for which the factor of Prandtl is applicable and often used.

The decay of the rotating sectional lift coefficients towards the tip is described here with an exponential function of the aspect-ratio of the part of the blade outboard of the section under consideration: $AR_{\rm out}$. The sectional lift coefficients reduce to the values in deep-stall because the radial flow phenomena only disturb the (negative) pressure on the suction side of the airfoil. After some careful and conservative fitting with the coefficients of the 95% section and with the blade root flapping moment, the following empirical reduction was formulated:

$$c_{\rm l.rot.tip} = c_{\rm l.non-rot} - (\Omega\, r/V_{\rm eff})^2 \cdot e^{-2.0\, AR_{\rm out}} \cdot (c_{\rm l.pot} - c_{\rm l.non-rot})\, c_{\rm l.non-rot}/c_{\rm l.pot}\ . \qquad (4.4)$$

This reduction is proportional to the "amount of stall", here expressed with $(c_{\rm l.pot} - c_{\rm l.non-rot})$. In fact the reduction in lift coefficients is related to the dimension of the separated area of the more inboard sections. The factor $c_{\rm l.non-rot}/c_{\rm l.pot}$ is simply to avoid negative lift coefficients. This empirical reduction is implemented in the programs BLADMODE and PHATAS for locations outboard of the 80% radius, while inboard of the 80% radius the expression(s) for enhanced lift (and drag) and/or delay of stall are applied. The "potential lift coefficient" applies to $c_{\rm l.pot} = 2\pi\, \sin(\alpha - \alpha_0)$. This expression also has the dependency on the speed ratio $(\Omega\, r/V_{\rm eff})^2$, similar as was derives for the enhanced coefficients due to rotational augmentation. Although an exponent of e.g. $-1.5\, AR$ fits better with the measurements on the UAE phase-VI rotor, some conservatism is applied by using $-2.0\, AR$ because the reduction of sectional loads also reduces the design loads calculated with e.g. PHATAS. However, modern large size wind turbines have a strongly tapered blade geometry for which this load reduction will never be strong.

Remarks

Because the model presented here is highly empirical, the following remarks can be made:

- The exponent 2.0 in the decay-function can be fitted more accurately (and slightly less conservative?) if the measurements of more and different rotors are used;
- The reduction of the aerodynamic drag coefficient (see Figure 4.7) has not been modelled yet. Based on the fact that the radial flow from the inboard sections give some positive pressure in the tail-region of the airfoil, some reduction of the drag coefficient may be expected.
- When assuming the radial flow from the inboard part of the blade as the driving forces for the reduction of the sectional loads near the tip, this reduction should in fact depend on whether the inboard parts are stalled or not. Again this implies that for a rotating blade it is difficult to work with sectional coefficients.

4.7 Measured Rotating Coefficients for the S809 Airfoil

Similar as with the non-rotating measurements, the rotating aerodynamic coefficients of the S809 airfoil were reconstructed from the measurements of the normal-forces and tangential-forces on the 5 instrumented sections. These forces were measured in the NASA-Ames wind tunnel for the wind speed values: 5.0m/s, 6.0m/s, 7.0m/s, 8.0m/s, ..., and 25.11m/s. The measurements used here were for a 3.0deg pitch angle while the rotor speed (near 72rpm) was measured. The campaigns were for the 's' configuration, which means that the pitot-tubes were removed, so that they could not affect the aerodynamic characteristics.

With the corresponding values for rotor-speed, air density, and wind velocity the aerodynamic coefficients were reconstructed with the program *inflow*, see appendix B. For this reconstruction no pitch-correction was applied. Because of the radial flow components near the blade root, and the strong influence of the 'suction area' in the rotor centre, the aerodynamic coefficients for the 30.0% section were not thought to be valid for comparison with models based on quasi-2D blades.

For the 5 instrumented sections the coefficients from both the non-rotating measurements (for 30m/s tunnel wind velocity) and the rotating measurements are plotted in Figure 4.3 through 4.7. The rotating measurements are for the tunnel wind speed values from 6.0m/s through 18.1m/s (with increments of 1m/s) and for 20.1m/s and 25.11m/s. For comparison the results from the EllipSys3D calculations by Risø (see [38, 75]) are included.

For evaluation of the theoretical modelling of the rotational effects these figures also contain the coefficients corrected with the 'centrifugal pumping' method described in section 4.3. In the correction for rotational effects the dependency of the speed ratio $(\Omega r/V_{\text{eff}})^2$ was approximated with $(\cos\phi_{\text{inf}})^2$. The rotating measurements did not include the aerodynamic moment coefficients. Similar analysis of the measurements in terms of normal- and tangential- force coefficients were done by Schreck and Robinson [63].

For the small tunnel wind speed values of 6m/s and 7m/s a relatively large area of the blade is not in stall. For those conditions the aerodynamic coefficients match well with the coefficients for the non-rotating measurements, the values for the smallest a.o.a., which gives some confidence in the process applied by the tool *inflow*. Also the fact that the drag coefficients for small angles-of-attack are not negative shows that the tool *inflow* is not that bad. A comparison of the analysis tools for the induced velocities and angles-of-attack is given in section 4.8.

The rotating coefficients in stall for the most inner section (30.0%) in Figure 4.3 show a (unrealistic) decrease in angle-of-attack for wind speed values increasing from 11m/s to 14m/s. This decrease in angle-of attack, and the associated high lift coefficients may be caused by stall of the midspan region of the blade, which gives boundary-layer suction of the separation area of the root section. Although it is always right to consider mistakes/deficiencies in the analysis tools (here *inflow*) it follows that the aerodynamics of a rotating blade can not be described easily on sectional basis. The decreasing angle-of-attack for the 30.0% section may also be caused by the discretisation of the blade in only 5 segments, see also section 4.8.

For the 30.0% section Schreck and Robinson [63] found very large normal-force coefficients. The rotating coefficients for the 46.6% and the 63.3% section show an increased lift coefficient of the same amount as what is expected from the correction models for rotational augmentation. Contrary to this, the rotating lift coefficients for the 80.0% section show a small reduction in maximum lift, while the rotating lift coefficients for the 95.0% section appear to be much smaller than the non-rotating values. The lower lift coefficients for the 95.0% section were also found by Sørensen with the Navier-Stokes code EllipSys3D [38, 75]. For the 30.0% section the EllipSys3D calculations did also show large values of the lift coefficient although they remain below $2\pi\alpha$.

In general, it is felt that with the program '*inflow*' the angle-of-attack for the 30.0% section (esp. in stall) is too small, see also section 4.8 and section B.5.

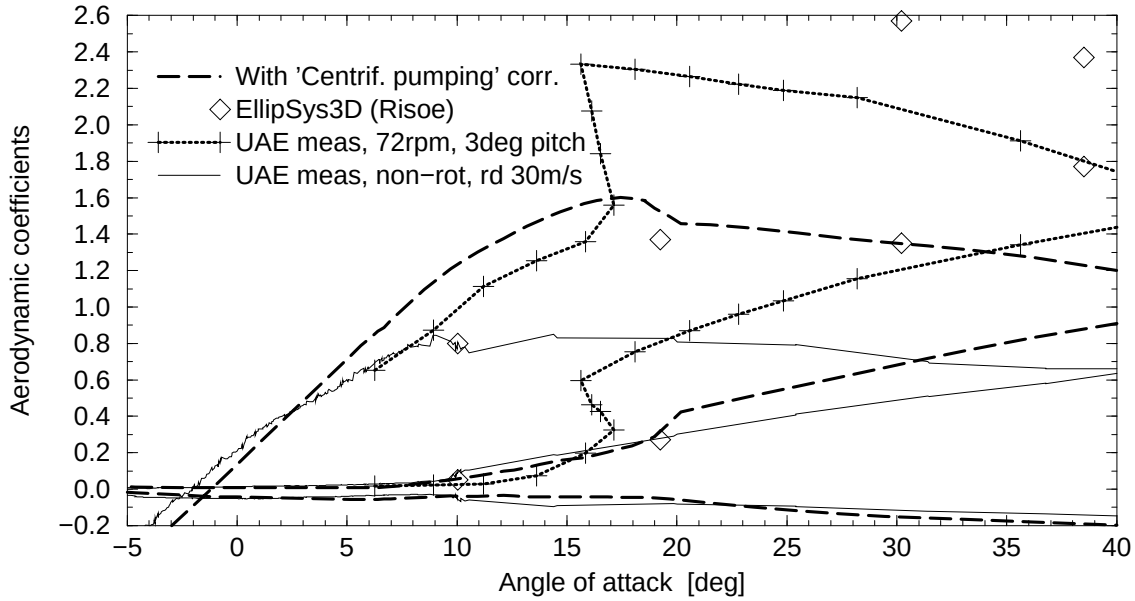

Figure 4.3 *Rotating and non-rotating coefficients for the 30.0% section*

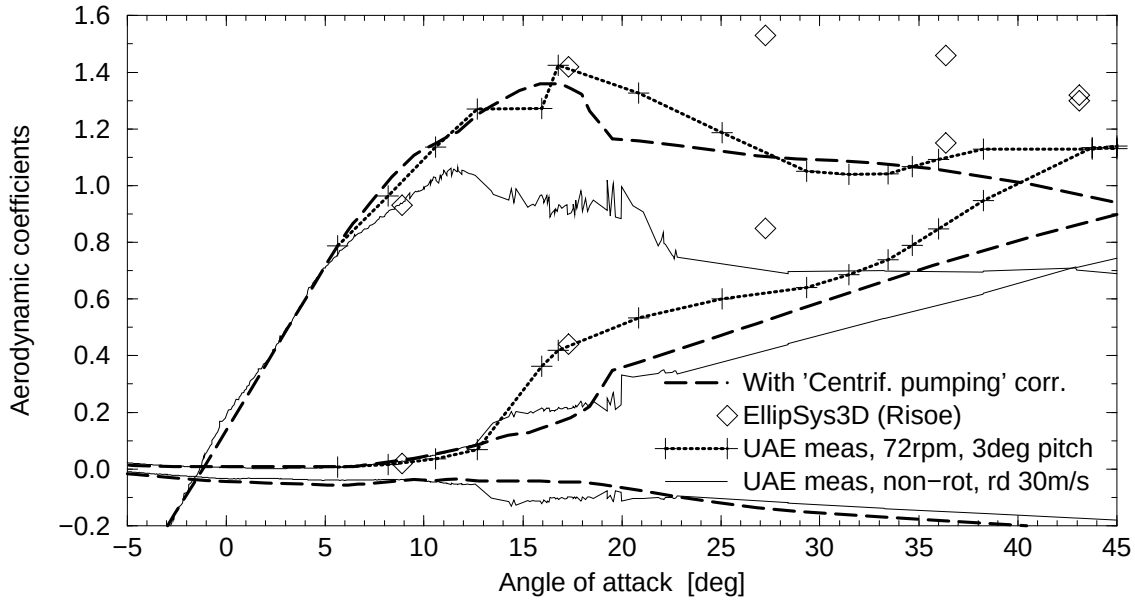

Figure 4.4 *Rotating and non-rotating coefficients for the 46.6% section*

Figure 4.5 shows that the lift coefficient at the 63.3% section drops down (stalls) at an angle-of-attack of 17deg, which is for the 11m/s tunnel wind speed. At higher angle-of-attack or wind speed values the lift recovers to values up to 1.2, which was also found by Tangler [78]. An explanation has not yet been given, although one may conclude that these local 'stall cells' are hard to predict with BEM-based models.

For the sections up to and including 80% the drag coefficients from the rotating measurements show to be larger than the non-rotating drag coefficients, although the for the 80.0% section the lift coefficient does not exceed the non-rotating values. For the 95.0% section the rotating lift coefficients appear to be smaller than the non-rotating coefficients while the drag coefficients are nearly equal to the non-rotating values, except in deep stall. It can thus be concluded that for the UAE phase-VI rotor the effects of rotation include an increase of drag coefficients in stall for a large span of the blade. For the 95.0% section the empirical model for the lift reduction near the tip is conservative because no comparisons have been made with measurements of other blades.

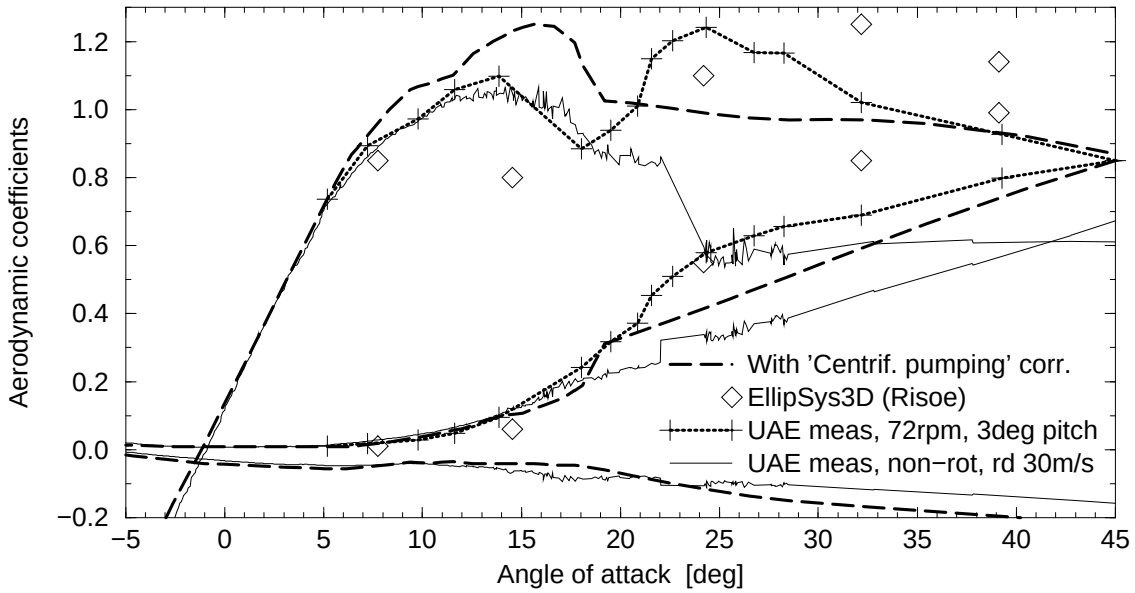

Figure 4.5 *Rotating and non-rotating coefficients for the 63.3% section*

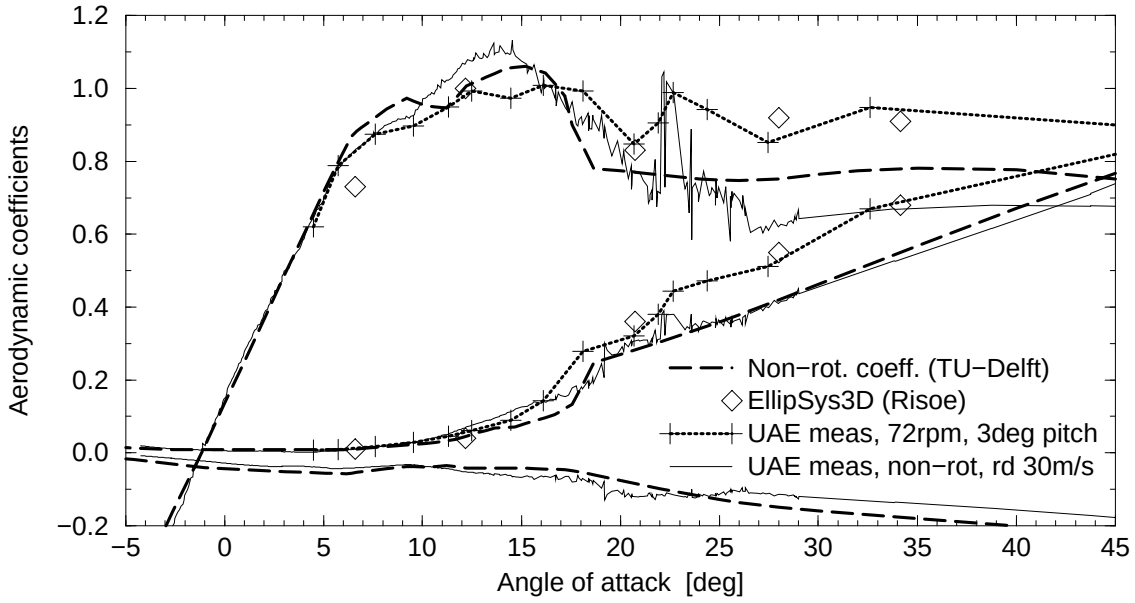

Figure 4.6 *Rotating and non-rotating coefficients for the 80.0% section*

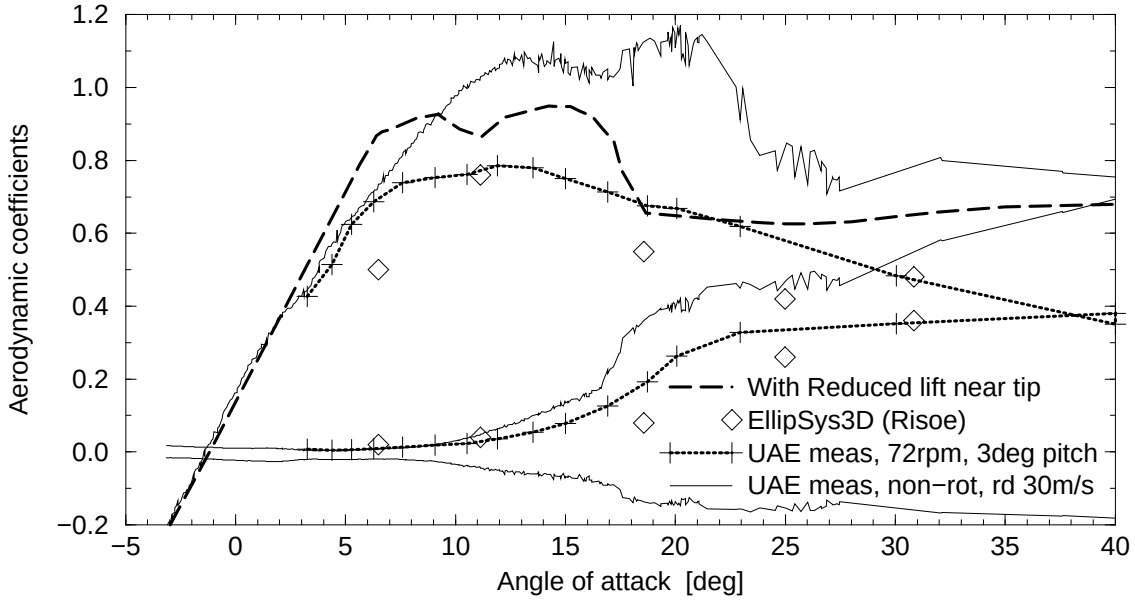

Figure 4.7 *Rotating and non-rotating coefficients for the 95.0% section*

Aerodynamic coefficients retrieved with '*inflow*'

Following are the aerodynamic coefficients that are retrieved with the tool *inflow* from the rotating measurements on the phase-VI rotor. This was done by including the 'flow curvature' effects related with the finite chord. However, the influence of the aerodynamic moment is not included, which may be the reason for the relative small angle-of-attack for the stalling state of the root section.

The number of decimals in this table does not reflect the accuracy.

	30.0% section		46.6% section		63.3% section		80.0% section		95.0% section	
# Wind	Alpha	C_lift	C_drag	Alpha	C_lift	C_drag	Alpha	C_lift	C_drag	Alpha	C_lift	C_drag
6.0	6.17	0.654	0.017	5.58	0.787	0.006	5.13	0.736	0.009	4.46	0.620	0.007	3.23	0.427	0.007
7.0	8.88	0.872	0.022	8.15	0.964	0.016	7.19	0.894	0.017	5.73	0.789	0.009	4.37	0.515	0.004
8.0	10.90	1.119	0.022	10.37	1.139	0.032	9.59	0.974	0.026	7.48	0.876	0.016	5.15	0.625	0.005
9.0	13.58	1.256	0.072	12.66	1.270	0.067	11.61	1.059	0.048	9.52	0.898	0.029	6.27	0.686	0.008
10.1	16.00	1.352	0.201	16.07	1.269	0.365	13.97	1.097	0.096	11.40	0.949	0.046	7.67	0.738	0.014
11.0	16.98	1.565	0.323	16.66	1.428	0.417	17.96	0.887	0.241	12.41	0.995	0.061	9.00	0.754	0.018
12.1	16.72	1.831	0.431	20.97	1.322	0.536	19.62	0.937	0.318	14.57	0.973	0.091	10.61	0.761	0.024
13.1	16.33	2.067	0.469	25.17	1.182	0.602	20.96	1.008	0.372	16.20	1.007	0.145	11.99	0.785	0.037
14.1	15.72	2.328	0.599	29.38	1.049	0.640	21.62	1.148	0.454	18.15	0.993	0.278	13.55	0.779	0.055
15.1	18.13	2.303	0.755	31.49	1.039	0.686	22.66	1.202	0.509	20.71	0.847	0.321	15.02	0.750	0.079
16.1	20.51	2.271	0.870	33.40	1.044	0.739	24.30	1.244	0.578	21.89	0.907	0.380	16.89	0.714	0.126
17.1	22.81	2.224	0.960	34.67	1.067	0.789	26.75	1.167	0.628	22.67	0.988	0.444	18.74	0.675	0.193
18.1	24.87	2.187	1.034	36.02	1.091	0.846	28.30	1.165	0.656	24.41	0.942	0.472	20.08	0.669	0.264
20.1	28.11	2.156	1.156	38.22	1.132	0.948	32.14	1.022	0.689	27.41	0.853	0.511	22.92	0.620	0.328
25.1	35.62	1.912	1.340	43.74	1.128	1.133	39.28	0.927	0.798	32.61	0.947	0.669	30.04	0.483	0.351

4.8 Comparison of Analysis Tools for the Induced Velocities

In appendix B a description is given of two analysis tools to reconstruct the angle-of-attack for a rotating rotor on basis of the blade load distribution. One of these tools *inflow* has been used for the measurements of the UAE phase-VI rotor in the NASA-Ames wind tunnel, and is based on a vortex description of the rotor wake. In particular because the aerodynamic coefficients retrieved for the 30.0% section give rise to some questions, special attention was paid to the evaluation of the tool *inflow*, see section B.5, while another analysis tool *beminf* has been developed on basis of the BEM approach, see section B.3.

An evaluation of the tools by comparison of the rotating coefficients from the UAE phase-VI measurements is given in Figures 4.8, through 4.11, where the coefficients obtained by Tangler with the angle-of-attack distribution of the Lifting-Surface Prescribed-Wake code 'LSWT' [78] are included. Using the code LSWT Tangler calculated the spanwise distribution of the induced velocities and angles-of-attack for a blade model with 40 strips. By adjusting the airfoil coefficients used in LSWT it was tried to match the spanwise distribution of the normal- and tangential- forces with those measured in the NASA-Ames wind tunnel. As reference these Figures also contain the non-rotating coefficients assessed in section 3.4 and the rotating coefficients without the influence of induced velocities. The coefficients of the 80.0% section show a good agreement and are therefore not plotted, see also Figure 4.6.

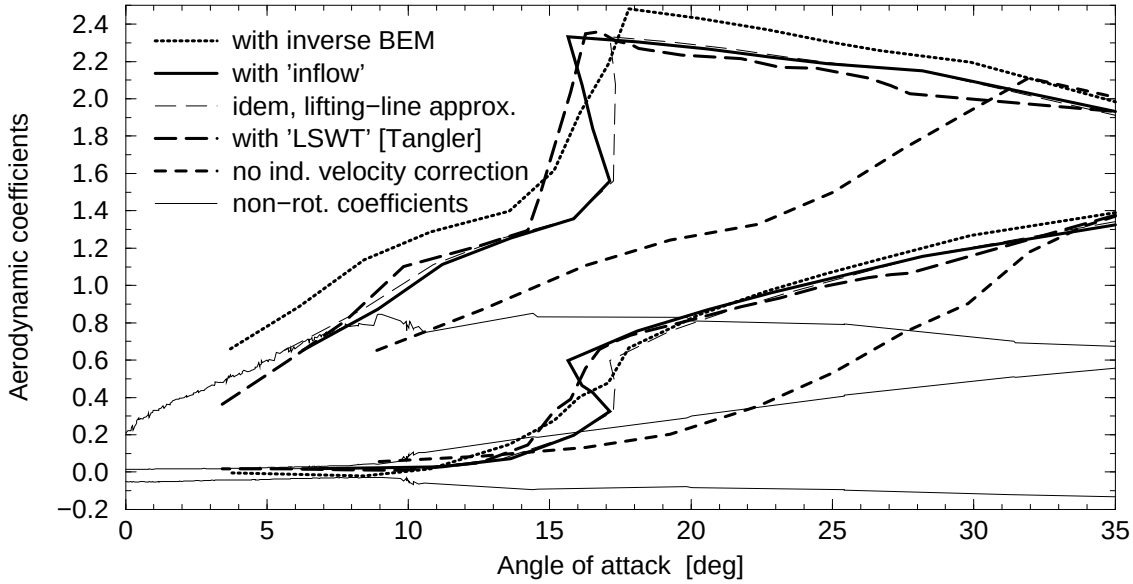

Figure 4.8 *Rotating coefficients reconstructed for the 30.0% section*

In general the magnitude of the lift coefficients retrieved with the different tools is quite similar. The angles-of-attack retrieved with the different tools show a reasonable agreement, knowing that the methods are fairly different. Although the tools 'LSWT and *inflow* are based on the theory differences still appear because in *inflow* the blade is modelled with only 5 segments (40 for LSWT). The angles-of-attack obtained with '*beminf*' (based on the 'inverse BEM' method) tend to be a bit too small such that it looks as if the non-stalled lift coefficients are over-predicted. For the maximum lift coefficient of the 30.0% section the inverse BEM method *beminf* gives a larger lift coefficient than the other methods. This may be caused by an under-prediction of the modelled 'effective relative velocity'. For some angles-of-attack the aerodynamic drag coefficients obtained with *beminf* are negative, in particular for the root section. The discrepancies for the root and tip sections can be explained with the fact that the flow around the tip and the root are approximated with e.g. the Prandtl factor, while this aspect is described in more detail with a vortex-description of the wake. It is thus concluded that although the inverse BEM method is practical but not the

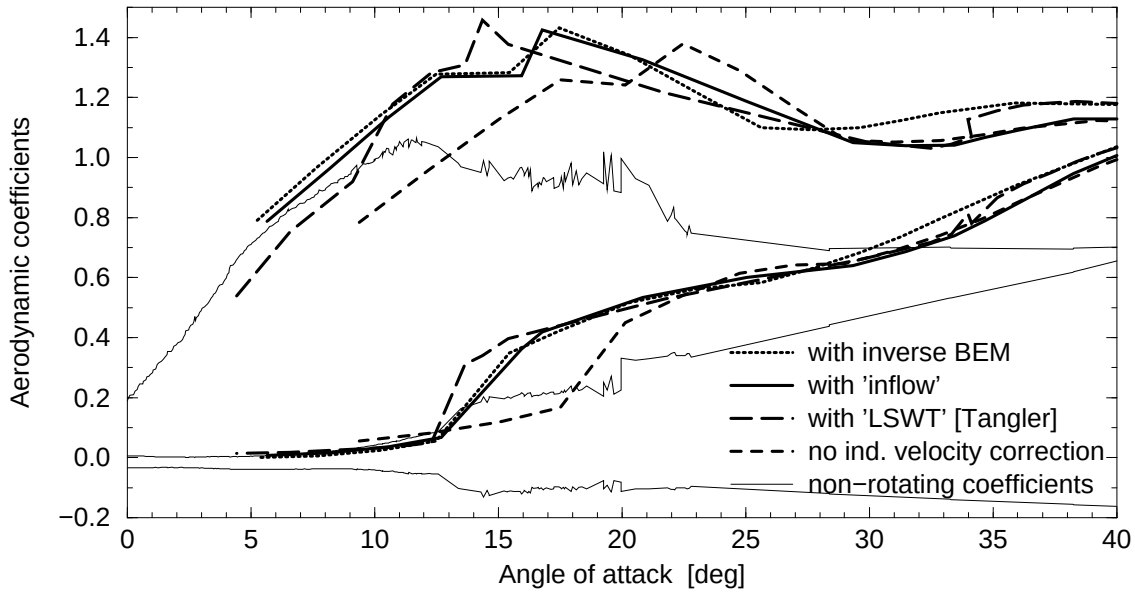

Figure 4.9 *Rotating coefficients reconstructed for the 46.6% section*

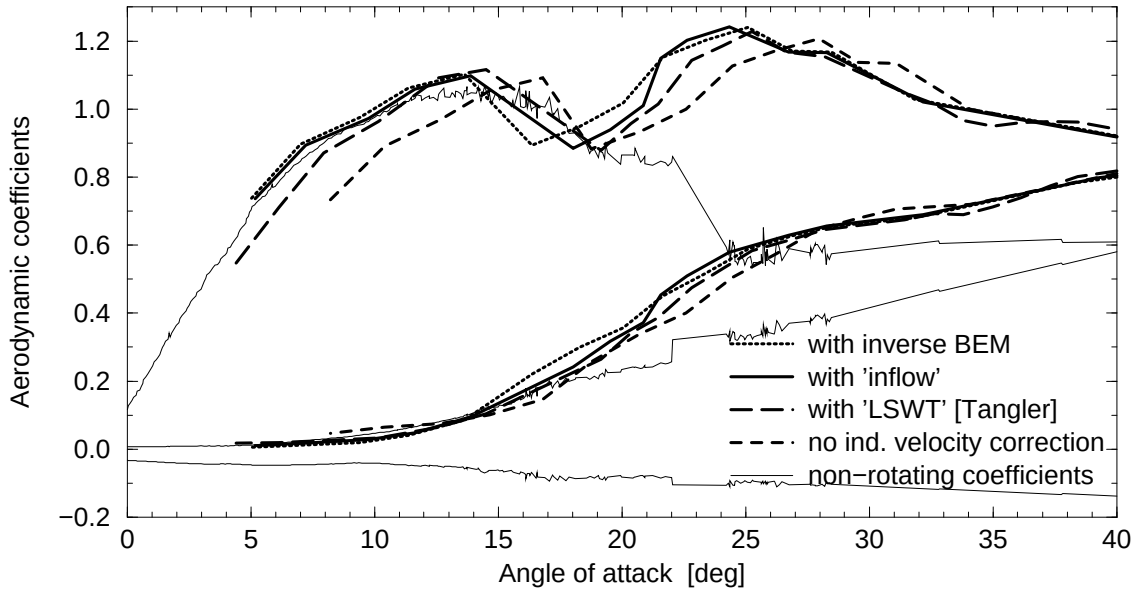

Figure 4.10 *Rotating coefficients reconstructed for the 63.3% section*

most accurate. This is also reflected by the negative drag coefficients found for the 30.0% section. For the root section the 'assumed' radius of the root-vortex has a large influence on the inflow distribution while it should be mentioned that the Prandtl factor does not apply well for the strong helical geometry of the root vortex. Based on this and knowing that the root area contributes little to the overall rotor performance R. van Rooij suggested (IEA meeting, May 2003) not to model root-loss effects at all.

The lift-curve retrieved with *inflow* for the 30% location still looks quite un-usual, at least compared to the 2D state. This lift curve is influenced most by the fact that the lift distribution is only modelled with 5 bound vortices. Another reason may be the effects associated with the finite chord. In the program *inflow* the 'bound vorticity' is assumed to be concentrated at the 25% chord line, while the inflow conditions are evaluated at the 75% chord line. To investigate the influence of these effects for the 30.0% section, the coefficients were also retrieved with *inflow* for which the circulation was concentrated at the blade-axis where also the inflow conditions were

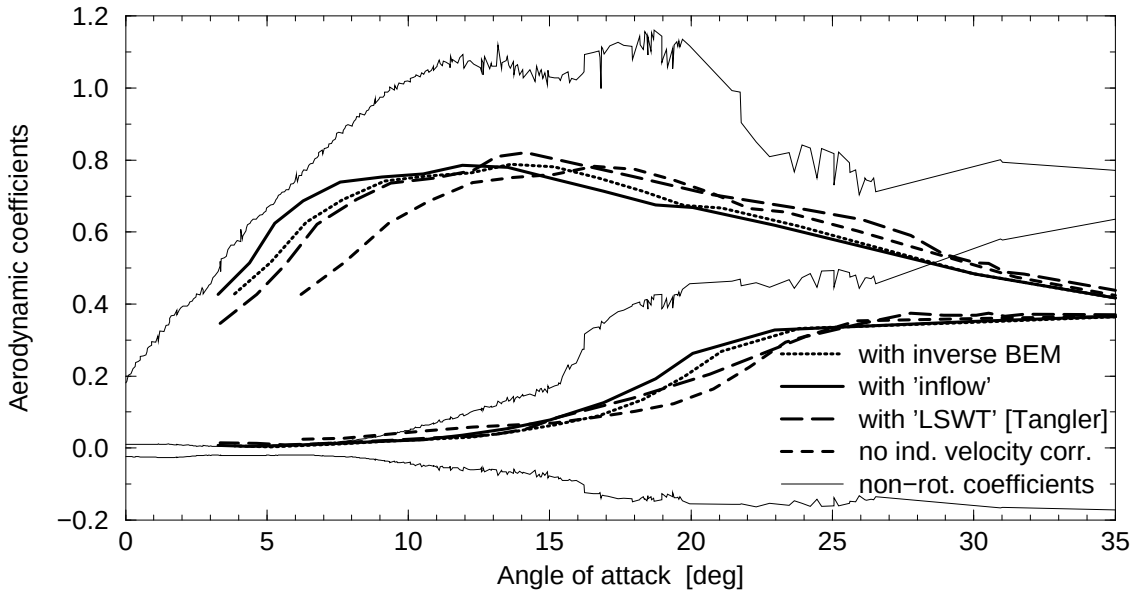

Figure 4.11 *Rotating coefficients reconstructed for the 95.0% section*

evaluated, see the thin dashed line in Figure 4.8. Using the 'lifting-line' approximation in *inflow* gives a difference (improvement?) in angle-of-attack for maximum lift of only 1.5deg. For blades with a relatively large chord it is finally suggested to include the contribution of the aerodynamic moment in the location of the bound-vorticity.

For both *beminf* and *inflow* it has to be mentioned that the induced velocities depend strongly on the choice of the radius of the root and the tip vortex, which can be used (although not very scientific) to obtain realistic coefficients for the root and tip sections.

Spanwise distribution of Angle-of-Attack

The lift curve for the 30.0% section retrieved from the rotating measurements (Figure 4.3 and 4.8) showed a very steep increase for a nearly constant or even decreasing angle-of-attack, which is for the measurements at 11m/s to 14m/s wind. This 'reversed' slope of the lift curve was not found with all tools for retrieving the angle-of-attack distribution. It should also be noted that the very steep slope of the lift curve for the 30.0% section was not calculated by Risø with the EllipSys3D code. In searching for more insight, the distribution of the angle-of-attack was plotted in Figure 4.12 together with the geometric angles-of-attack and the angle-of-attack distributions calculated with EllipSys3D (Risø) and PHATAS. The latter was done with the '3D correction' of Snel e.a.

Because these investigations are finally addressed to improvements of the current BEM-based design codes, the results of PHATAS in Figure 4.12 should not be seen/used as reference for analysis of the measurements. Figure 4.12 shows that the angles-of-attack from the rotating measurements (with *inflow*) for the 46.6% section at 15m/s wind are even larger than the geometric angle-of-attack. This may be caused by the influence of the strong loading of the 30.0% section together with the fact that the phase-VI rotor blade is modelled in *inflow* with only 5 segments of constant bound-vorticity.

For the higher wind-speed value of 15m/s the angle-of-attack for the 30.0% section was rather small, which is also shown in the validation of '*inflow*', see section B.5. The under-prediction of the root angle-of-attack may be caused by the finite number of sections from which loads are used. Despite the validations of *inflow* reported in section B.5, it must still be expected that the model needs improvements/corrections.

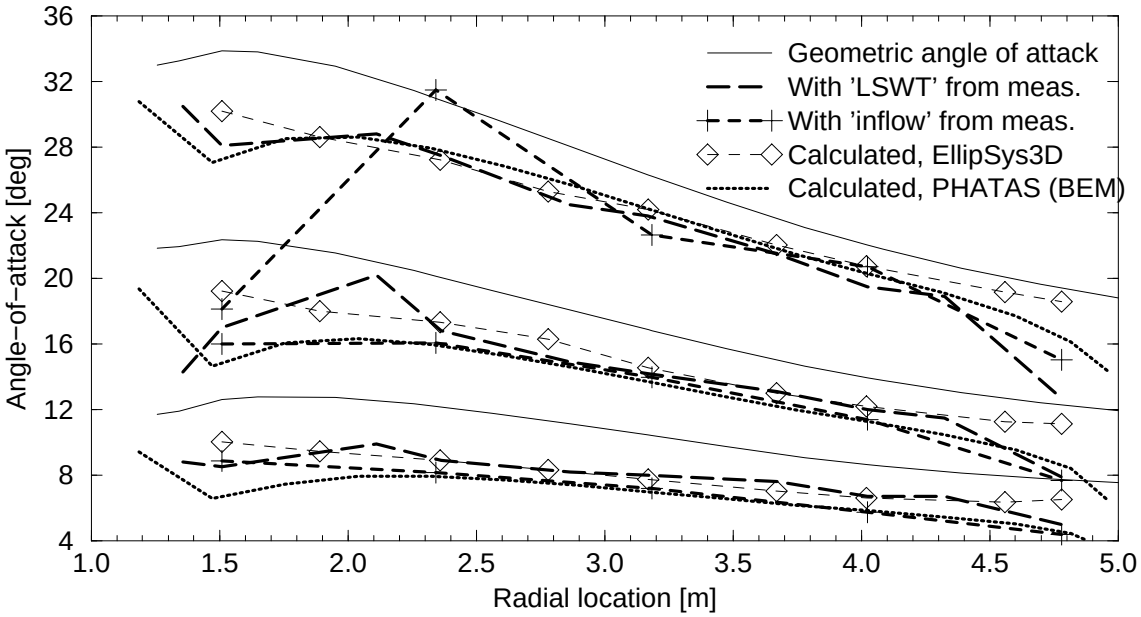

Figure 4.12 *Angle-of-attack distributions for 15, 10, and 7m/s wind*

4.9 Comparison of Correction Methods

To give a rough impression of the difference between some of the correction models for rotational augmentation and the measured properties of the blade, the spanwise distribution of the maximum lift coefficient is plotted in Figure 4.13. The maximum calculated lift coefficients in Figure 4.13 following the correction methods all include the dependency on the speed ratio $(\Omega\, r/V_{\mathrm{eff}})^2$ with the approximation $(\cos\theta_{\mathrm{p}} + \theta_{\mathrm{tw}} + \alpha)^2$. Here θ_{p} is the 3.0deg pitch angle of the phase-VI rotor.

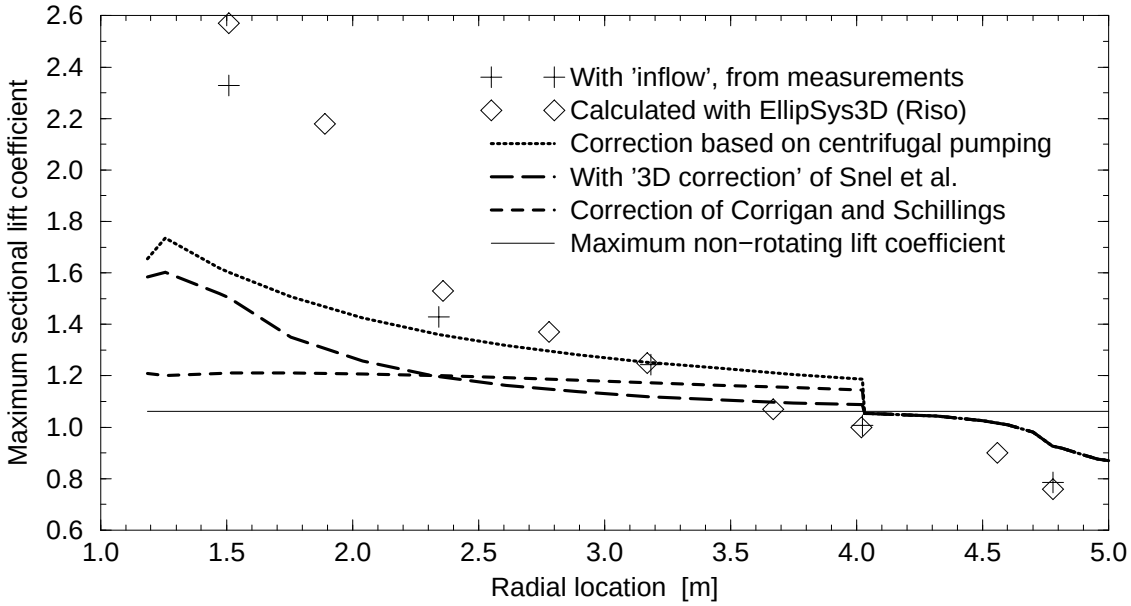

Figure 4.13 *Spanwise distribution of the maximum lift coefficients*

Although strictly speaking the EllipSys3D results are also based on some model representation (that is very detailed) the spanwise distribution of the maximum lift coefficients matches very well with the measurements and can thus be seen as additional reference for investigations.

The quadratic dependency of the method of Snel et al. has a spanwise distribution that fits reasonable with the maximum lift from the measurements, although the amount of enhanced

lift is far smaller (1/3). It is expected that both the maximum sectional coefficients and the rotor performance (see chapter 6) can be described well if also the increase in drag coefficient is modelled.

It should be kept in mind that Figure 4.13 has a limited value because it does not represent the lift distribution as function of angle-of-attack, nor the rotating drag coefficients.

4.10 Concluding Remarks

Modelling rotational augmentation is difficult because:

The non-rotating coefficients don't serve as basis So first these are to be assessed.

The enhanced lift is partly due to a 'delay of stall' It should be found-out how the increase of normal force (lift) and shift in a.o.a. are related.

Reduction of coefficients of tip sections The small values of the 'stall' lift coefficient measured for the 95.0% section and the corresponding reduced drag compared with the non-rotating coefficients show that the effects of rotation in the tip-region are opposite to that for the midspan and root region of the blade. This implies that the under-prediction of the load-reduction towards the blade tip is not (only) due to a mis-fit of the Prandtl factor.

The root has excessive strong rotational effects In fact this requires additional modelling, probably of the spanwise equilibrium equations of the separated flow.

Stall is not uniform over the blade span This means that it is hard to use sectional coefficients.

Positive aspects are:

The model of Snel et al. fits reasonable Although the quadratic (c/r) dependency is too strong compared to the equations for 'centrifugal pumping', it does imply a fit for the excessive rotational effects at the root area.

Rotor-average effects work quite well Although (stable) local stall may occur, the rotor-average effects of rotating aerodynamic coefficients can be calculated with reasonable accuracy using the existing empirical models.

Questions to be solved:

Effect on drag is still badly quantified Measurements show a far larger maximum lift than what is found with the empirical rules, although the calculated (rotor-average) shaft power corresponds reasonably. It is thought that both the maximum lift and the rotor performance can be matched better if also the enhanced drag is modelled.

Location of the root vortex For the following question to be solved, first the location of the root vortex has to be defined.

Rotational effects near the root The effects near the blade root are still not yet described, although they are approximated with a too strong dependency of (c/r).

At the 80.0% section there seems to be no rotational augmentation. Still the lift and drag coefficients (from measurements and from EllipSys3D code) for 25deg or more are larger than the non-rotating state. This can be due to the fact that the formation of leading-edge separation bubbles or leading-edge stall does not occur in the rotating state.

For the work within the IEA Annex-XX project it is suggested here to investigate the location of the separation point, similar as the investigations by Schreck [64]. The accuracy may be limited by the finite number of pressure taps.

5. ASPECTS OF BEM THEORY

5.1 Introduction

The inflow conditions of a wind turbine rotor are a combination of the wind loading and the 'induced velocity'. The latter describes the influence of the aerodynamic rotor loading on the flow. For a normal operating wind turbine, the rotor subtracts energy from the air which implies that the generally the induced velocity is smaller than the undisturbed wind velocity. For a slender rotor blade with a relative low loading, a very rudimentary approach would be to calculate the aerodynamics directly from the relative inflow over the blade, resulting from the undisturbed wind velocity and the blade motion. This means using the 'geometric' angle-of-attack, see Figure 4.12.

For wind turbines this is not sufficient since they are designed to subtract energy from the air and therefore give some reduction (in the order of 30.0%) of the flow velocity in the rotor disk. The basic purpose of BEM codes (**B**lade **E**lement **M**omentum method) is to describe this so-called 'induced velocity', which is done by equating the loss of momentum of the flow to the loads on the rotor blades/disk. In computer codes for wind turbine rotor design, these momentum equations are solved for a finite number of annular stream-tubes, of which the loss of momentum in the flow is equated to the aerodynamic loads of a blade element. The detailed flow around the tips of the blades is described with a so-called 'tip loss' factor, for which the expression derived by Prandtl is commonly used in engineering models. Although BEM theory looks quite simple, its accuracy depends on a proper implementation of the combination of models for e.g. 'tip-loss', oblique inflow, unequal blade loading, wind shear, and turbulent wake state.

This chapter deals with some aspects of BEM theory for which the insight has been improved or that need special attention. The formulations presented here reflect the implementations in BLADMODE [45] and in release "OCT-2002" of the program PHATAS [46]. These formulations were also used in the 'inverse BEM method', described in section B.3.

Vortex structure of the wake

The influence of the wake on the flow in the rotor plane can be described as if it results from the vorticity in the wake. Although this approach is of practical use in calculation models, one should realise that a vortex is in fact a method to describe circulation in the flow, such as with the Biot-Savart law (see also appendix B). The mathematical relations for vorticity are based on the continuity relations and conservation of momentum for an incompressible fluid.

At the tip of a rotor blade and also an aircraft wing the air flows from the aerodynamic pressure side to the aerodynamic suction side. This can be described with the trailing vorticity, which gives a reduction of the inflow-angle towards the blade tip and likewise a reduction in lift on the blade. For wind turbines this is called 'tip loss'. The name 'tip loss' was already used in the early investigations into wind turbine dynamics, where it was known that the performance had to be calculated with e.g. 97% of the real rotor radius, which looks as if the power of 3% of the radius is "lost". This mechanism for reduction of loads towards the tip can be described with a vortex representation of the flow where the decrease in circulation (lift) involves trailing vorticity. Downwind of the blade/wing this trailing vorticity tends to roll-up to a concentrated tip vortex.
(For an aircraft flying with low speed –so with high lift– through humid air, the low pressure in the core of the tip vortices lead to condensation which can be observed during landing approach.)

The relative inflow angle of the air on the blade/wing sections can be described for the vortex structure that consists of bound vorticity and of trailing vorticity. This implies that aerodynamic models based on a vortex description of the wake and 'lifting-line' or 'lifting-panel' methods are capable of describing the flow around the blade/wing tip. Here a lifting-panel model has the

advantage over a lifting-line model that it includes the effects of the finite chord of the blade.

The use of Blade Element Momentum theory with a correction for tip flow (such as the Prandtl factor) for wind turbine rotors is meant to describe the induced velocity distribution and is as such the counterpart of the "integral-equations of Prandtl" described in 'wing theory' for aircraft.

5.2 Blade Element Momentum Equations

For lightly loaded rotors the wake has a semi infinite cylindrical geometry. The loss of momentum of the air in the rotor wake can be described with a trailing vortex structure on the "surface" of this cylinder resulting from lift, and a helical vortex structure resulting from drag, see Figure 5.1.

The centre of the rotor wake contains some root vorticity of which the strength equals the axial components of the trailing vorticity on the wake boundary, such that flow outside of the rotor wake does not have a global tangential induced velocity. At the rotor plane the induced velocity of the trailing vortex structure on the surface of the cylindrical wake and of the root vorticity is half of the induced velocity far downstream in the wake since the wake structure is semi infinite.

For low solidity rotors the viscous wake from drag of the airfoils consists of helical filaments of air enclosed by "sleeves" of vorticity. With the trivial assumption that diffusion of these filaments takes place behind the rotor plane, these vortex sheets induce *no* velocity in the rotor plane, because this is outside of the viscous wake filaments. Since the momentum equations are used to calculate the induced velocity in the rotor plane these equations do *not include the drag-term*, see also [3, p.117] and [84, p.4-10]. Still the viscous wake of the airfoil has a small influence because the loss of momentum involves some flow expansion. This disturbance from flow expansion is perpendicular to that from the loss of momentum due to drag, which means that flow expansion from airfoil drag should *not* be described as loss of momentum of the annular flow.

For lightly loaded rotors the wake has a nearly cylindrical shape while the radial flow components are zero. From application of Bernoulli's law and conservation of momentum but also from a wake decomposition (shown in Figure 5.2) it follows that the axial induced velocity in the rotor plane is half of the induced velocity far downwind. For stationary axial flow through an annulus of width Δr in the rotor plane with cone angle α_c, equating the loss of axial momentum in the rotor plane to the axial component of the lift forces on the rotor blades gives

$$B\,(\rho/2)\,c\,(\Delta r/\cos\alpha_c)\,c_l\,\cos\phi_{inf}\,\cos\alpha_c\,V_{eff}^2 = \rho\,(2\,\pi\,r\,\Delta r)\,2\,U_i\,|U_{wind}-U_i|$$

with ϕ_{inf} the local inflow angle: $\tan\phi_{inf} = (U_{wind}-U_i)\cos\alpha_c\,/(\Omega\,r+V_i)$,
V_{eff} the local velocity on the blade element: $V_{eff} = \sqrt{((U_{wind}-U_i)\cos\alpha_c)^2+(\Omega\,r+V_i)^2}$,
U_{wind} the undisturbed wind velocity,
and U_i and V_i are the axial- and tangential induced velocities at the rotor plane.
The absolute value of the 'transport velocity' term $|U_{wind}-U_i|$ is used, such that this formulation also holds for reversed flow. Still the aerodynamic forces are to be evaluated with the local flow at the rotor blade: $U_{wind}-U_i$.
Note that in an annulus of width Δr the length of an element is $\Delta s=(\Delta r/\cos\alpha_c)$ while the axial force on the annulus is the $\cos\alpha_c$ component of the normal force on the rotor blades.

Dividing the resulting momentum equation by the air density ρ and the area of the annulus gives

$$\sigma\,c_l\,\cos(\phi_{inf})\,V_{eff}^2 = 4\,U_i\,|U_{wind}-U_i|\,. \tag{5.1}$$

Here $\sigma = B\,c/(2\,\pi\,r)$ is the local 'solidity' at radius r.
The momentum equation in tangential direction can be formulated similarly

$$\sigma\,c_l\,\sin(\phi_{inf})\,V_{eff}^2\,/\cos\alpha_c = 4\,V_i\,|U_{wind}-U_i|\,. \tag{5.2}$$

The tangential blade loads do not have to be decomposed so they still have the factor $1/\cos\alpha_c$.

The description given here deals with the 'aerodynamic cone angle' of the blade, which includes the cone angle of the rotor hub with the pre-bend geometry and the elastic deformation.
The cone angle α_c of the rotor appears as '$\cos \alpha_c$' components (so second order effects of α_c) in the tangential momentum equation (5.2) and indirectly in the relative velocity V_{eff} on the blades. The influence of the cone angle on the relative flow of the airfoils is described in section 5.7.
For a more complete description of the cone angle effects one may also include the radial flow components and also use the equation for the radial momentum and the radial pressure gradient.

5.3 Modelling the Flow around the Blade Tip

By the influence of the flow around the tip (trailing vortex), the angle-of-attack decreases towards the blade tip. For a wind turbine rotor this can be described as if the local induced velocity is larger than the average induced velocity between the subsequent passings of the blades. The wake of the rotor has a helical structure consisting of trailing vortices. For high tip-speed ratios the flow of this wake structure has some similarity with the flow around the edges of a set of flat plates placed in downwind direction.

For the flow around a set of semi infinite plates perpendicular to the ambient flow, representing the vortex sheets, Prandtl described a relation between the average flow between the plates at radius r and the relative velocity of the plates (or vortex sheets).

$$\bar{U}_{\text{i.wake}} = F_{\text{tip}} \cdot U_{\text{i}} = 2/\pi \, \arccos(e^{-\pi(R-r)/d}) \cdot U_{\text{i}} \, .$$

Although the geometry of the semi-infinite plates differs from that of the helical rotor wake, Prandtl suggests to use this factor F . The velocity $\bar{U}_{\text{i.wake}}$ is the downstream-average in the wake (*not* the annulus-average), r is the local radius, and d the distance between the trailing vortex sheets. For turbines with a high tip speed ratio, the distance d is small compared to the radius R so that F approaches 1 for small radial positions r . This means that only near the edges of the rotor or its wake, the factor F differs from 1. Near the edges of the rotor wake, the geometric similarity with the edges of a semi infinite row of plates is good enough to use the expression for F.

The reduction in angle-of-attack near the blade root is included using also the Prandtl factor. The resulting expression for F finally becomes:

$$F = F_{\text{tip}} \cdot F_{\text{root}} = 2/\pi \, \arccos(e^{-\pi(R-r)/d}) \cdot 2/\pi \, \arccos(e^{-\pi(r-r_{\text{root}})/d_{\text{root}}}) \, . \qquad (5.3)$$

Here d is the distance between the trailing vortex sheets.

The distance d between the trailing vortex sheets decreases in downwind direction so that the factor F tends to be under-estimated. However, the fact that trailing vortices also tend to roll-up in downwind direction (to e.g. 95% of the radius) and the fact that the trailing vortex sheets are cylindrical rather than straight implies an over-estimation of the factor F.

A more accurate solution for this 'tip loss factor' (in terms of Bessel functions) was derived by Goldstein [29]. This solution is based on a cylindrical wake geometry so that it holds for lightly loaded propellers.

For the implementation of the 'correction factors' for the flow around the blade tips of wind turbines, several formulations of the momentum equations exist. These formulations differ in the 'mass flow' term or 'transport velocity' that is used in the axial (and also in the tangential) momentum equations.
Glauert : $F \, U_{\text{i}} \, (U - U_{\text{i}}) \, .$
Wilson and Lissaman : $F \, U_{\text{i}} \, (U - F \, U_{\text{i}}) \, .$
A more detailed expression for the average loss of momentum was given by de Vries [84], in terms of the distribution of the induced velocities between the trailing vortex sheets. More accurate descriptions for the loss of momentum such as formulated by de Vries, have the complication that the radial velocities near the blade tip imply a radial transport of axial momentum. For this reason

the models in PHATAS and in BLADMODE still use the formulation of Wilson and Lissaman. A comparison of different implementations of the tip-correction factor has been reported by Shen et al. [68].

Using the factor F on the annulus-average induced velocity and the relations (see Figure 5.3 for zero α_c) $\cos\phi_{inf}\, V_{eff} = \Omega\, r + V_i$ and $\sin\phi_{inf}\, V_{eff} = (U_{wind} - U_i)\cos\alpha_c$ gives for the momentum equations:

$$\sigma\, c_l\, (\Omega\, r + V_i)\, V_{eff} = 4\, F\, U_i\, |U_{wind} - F\, U_i| \; ; \tag{5.4}$$

$$\sigma\, c_l\, (U_{wind} - U_i)\, V_{eff} = 4\, F\, V_i\, |U_{wind} - F\, U_i| \; . \tag{5.5}$$

Trailing vortex distance

The tip loss factor used in the expressions of the flow around the blade tips depends on the distance between the trailing vortex sheets d, where it has already been mentioned that this distance decreases in downwind direction while the diameter of the wake expands. Here the trailing vortex distance is expressed with the wake geometry short downwind of the rotor because this has the largest influence, where the downwind-average axial velocity is $U_{wind} - F\, U_i$. Short downwind of the rotor the wake has its full tangential induced velocity ('wake rotation'), so that the downwind-average of the relative velocity on the blade is $\Omega\, r + 2\, F\, V_i$, see Figure 5.3.

However, the wake of a rotor blade does not have a concentrated trailing vortex, but a vorticity that is distributed over the outer part of the blade. The fact that the influence of the trailing vorticity is the total of the influence of the outer part of the blade, implies that one may use a trailing vortex distance that is an average over the outer part of the blade span. For some rotor blades it was shown that the induced velocity U_i increases towards the tip while the product $F\, U_i$ decreases towards the tip. For BLADMODE and PHATAS it was decided to use a velocity of the 'average tip vortex' of $\sqrt{F}\, U_i$ which shows little variation of the calculated trailing vortex distance d over the blade span.

Velocity of tip vortices

The difference between the velocity inside and outside of the rotor wake is described in fact by the trailing vortices. This means that these trailing vortices can be modelled as located between the inner and outer flow of the rotor wake. Similar as for 'roller bearings between two surfaces', the velocity of the tip-vortices is the average of the velocity inside and outside of the wake.

Using these velocities in the so-called 'velocity triangle' gives for the distance d:

$$d \; = (2\,\pi\, R/B)\, (U_{wind} - 0.5\,\sqrt{F}\, U_i)/\sqrt{(\Omega\, r + \sqrt{F}\, V_i)^2 + (U_{wind} - 0.5\,\sqrt{F}\, U_i)^2} \; . \tag{5.6}$$

A similar expression is used for the trailing vortex distance at the root, using r_{root} instead of R. Because of the fact that the trailing vortex distance d depends on the tip loss factor means that an iterative procedure is needed for the aerodynamic loads in each annulus. This iteration is also needed because of the non-linear nature of the momentum equations and of the relation between the lift coefficient with angle-of-attack.

The influence of the tip loss modelling on the performance of the UAE rotor is shown in section 6.3.4.

5.4 Correction for Flow Curvature Effects with Finite Chord

For blade sections that move in a coned rotor plane, the relative motion is not only a velocity V_{eff} but also a rotation $\Omega \sin\alpha_c$. In a coordinate system that is moving with the blade the relative airflow looks as if curved, see Figure 5.4 When omitting the tangential induced velocity V_i with respect to Ωr this flow curvature can be expressed with $\sin\alpha_c \cos\phi_{\text{inf}}/r$. In the research for vertical axis wind turbines the aerodynamics of an airfoil in curved flow is compared with an airfoil with additional 'virtual' camber in a straight uniform flow, see also Cardona [12] and Mandal & Burton [50]. This implies that a different set of aerodynamic coefficients has to be applied.

For a moderate flow curvature and for attached flow, the influence of 'virtual camber' on the aerodynamic coefficients can be described with a shift in the angle-of-attack and a correction on the aerodynamic moment coefficient.

For an airfoil with a uniform camber-line it can be shown with thin-airfoil theory that for a fully laminar flow the strength of the circulation (lift) is such that the flow at the 3/4 chord location is in the direction of the camber-line. Based on this, the angle-of-attack in curved flow is evaluated with the flow direction at the 3/4 chord location. If the 1/4-chord location lies a distance y_{ac} aft of the blade axis, the 3/4-chord angle-of-attack for a blade element is

$$\alpha_{3/4\,c} = \phi_{\text{inf}} - \theta_{\text{eff}} + \Omega \sin\alpha_c\,(c/2+y_{ac})/V_{\text{eff}} = \phi_{\text{inf}} - \theta_{\text{eff}} + \sin\alpha_c\,(c/2+y_{ac})\cos\phi_{\text{inf}}/r\ . \quad (5.7)$$

The angle θ_{eff} is the total value: $\theta_{\text{eff}} = \theta_p + \theta_{tw} - \phi_z$ with ϕ_z the blade torsional deformation.

In section 4.3 of 'Theory of Wing Sections' [1], (originally formulated by R.C. Pankhurst in 1944, see also section 3.1) an engineering method is given for the 'flow curvature' correction of the aerodynamic moment coefficient due to 'virtual camber'.
For a uniform curvature $\sin\alpha_c \cos\phi_{\text{inf}}\,(c/r)$ the corrected moment coefficient (nose-up) is

$$c_{m(\text{curved})} = c_m - 0.39 \sin\alpha_c \cos\phi_{\text{inf}}\,(c/r)\ .$$

In the program PHATAS the effect of flow curvature is not modelled in terms of a correction for 'virtual camber'. Instead, the inflow angle is evaluated with the relative flow components on the 3/4 chord location of the blade sections. This means that also the 'flow curvature' effects from the aerodynamic tower stagnation, from the turbulence in the wind, and from the blade pitch actions and torsional deformation are included. The dynamic pressure on the moving blade sections is evaluated with the relative velocities at the 25% chord location. The lift and drag components are also still defined in the directions of the local flow at the 25% chord location.

5.5 Mass Flux for Oblique Inflow

For wind turbines oblique inflow is usually dominated by yaw misalignment, although even for zero misalignment the rotor tilt angle gives some oblique inflow which is included in the models of BLADMODE and PHATAS. In general, oblique inflow on the rotor has the direct effect of a different local velocity and angle-of-attack on the rotor blades, which is called

'*advancing and retreating blade effect*'.

(In the program BLADMODE, only the rotor-disk average effects are included.)

When expressed in the wind direction, the loads on a yawed rotor disk have an axial and a lateral component. For the (now elliptical) wake of the rotor the 'wind-axial' component of the rotor loading leaves tangential vorticity on the (elliptical) wake surface, for which the momentum equations in the previous section can be applied on the airflow through the elliptical projected rotor plane. The 'wind-lateral' component of the rotor wake gives a change in transverse velocity, which can be described by two regions of axial vorticity on opposite sides of the wake. From potential flow theory it follows that for a change in lateral velocity of an elliptical tube the inertia loads are those for a volume of air that is the sum of the mass (here air) in the tube and the mass of a cylinder of air enclosing the width of the tube. The latter is a form of '*apparent mass*'.
Per unit wake-length the inertia loads thus have to be calculated for a mass of $\rho\,\pi\,R^2(1+\cos\chi)$.
Here χ is the misalignment angle between the wind direction and the rotor axis.

For the effects of oblique inflow in BLADMODE the in-plane loads on the rotor disk are omitted which means that the normal force on the rotor disk can simply be decomposed in the longitudinal and lateral components with respect to the wind direction relative to the rotor axis χ.

Using $U_{\rm tr} = \sqrt{(U_{\rm wind}\,\cos\chi - F\,U_{\rm i})^2 + (U_{\rm wind}\,\sin\chi)^2}$ as transport velocity, the longitudinal loss of momentum of the far wake in wind direction applies to $D_{\rm ax}\,\cos\chi = \rho\,(\pi\,R^2\,\cos\chi)\,U_{\rm i.long}\,U_{\rm tr}$ and the lateral loss of momentum of the far wake applies to $D_{\rm ax}\,\sin\chi = \rho\,(\pi\,R^2\,(1+\cos\chi))\,U_{\rm i.lat}\,U_{\rm tr}$.
Reconstructing the rotor-axial induced velocity at the rotor plane gives:

$$U_{\rm i} = (U_{\rm i.long}\,\cos\chi + U_{\rm i.lat}\,\sin\chi)/2 = \frac{D_{\rm ax}}{2\,\rho\,\pi\,R^2\,U_{\rm tr}}\,(\cos\chi + \frac{(\sin\chi)^2}{1+\cos\chi}) = \frac{D_{\rm ax}}{2\,\rho\,\pi\,R^2\,U_{\rm tr}}\ .$$

From this result it follows that the loss of momentum in axial direction has to be calculated for a volume of airflow with a cross-sectional area of $\pi\,R^2$ which is the area of the rotor plane. This has also been used by Glauert [28], see e.g. Bramwell [10] pp.124 and following.
So for a single annulus, the axial momentum equation is still:

$$\sigma\,c_{\rm l}\,(\Omega\,r + V_{\rm i})\,V_{\rm eff} = 4\,F\,U_{\rm i}\,\sqrt{(U_{\rm wind}\,\cos\chi - F\,U_{\rm i})^2 + (U_{\rm wind}\,\sin\chi)^2}\ . \qquad (5.8)$$

Tangential momentum equation

For a straight rotor blade the induced velocity in the relative flow on the airfoils is a result of the circulation around the airfoil and is therefore perpendicular to the local relative velocity.
This was also derived by De Vries [84] when he related the tangential induced velocity to the axial induced velocity:

$$V_{\rm i}/U_{\rm i} = \tan\phi_{\rm inf} = \cos\alpha_{\rm c}\,(U_{\rm wind}\,\cos\chi - F\,U_{\rm i})\,/\,(\Omega\,r + F\,V_{\rm i})\ . \qquad (5.9)$$

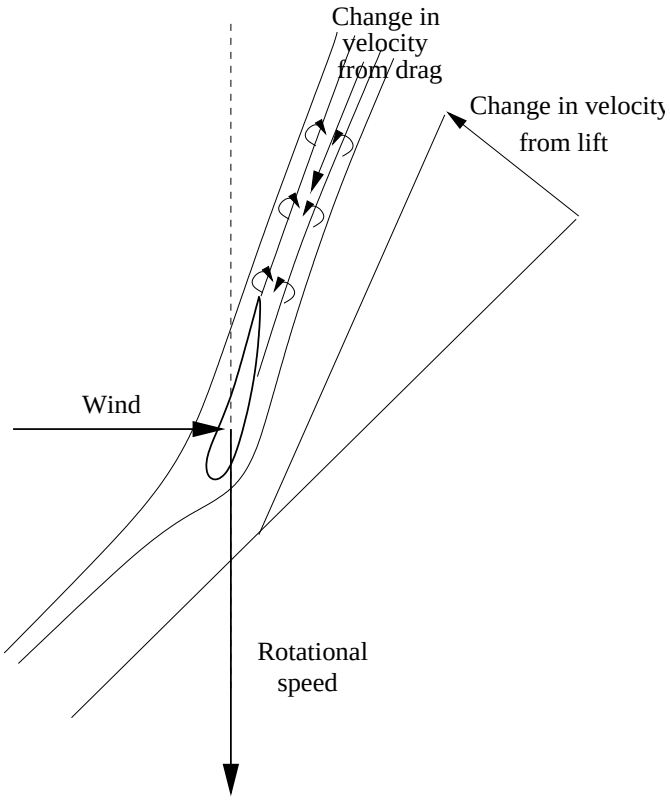

Figure 5.1 *Change in wake velocity from lift and from drag*

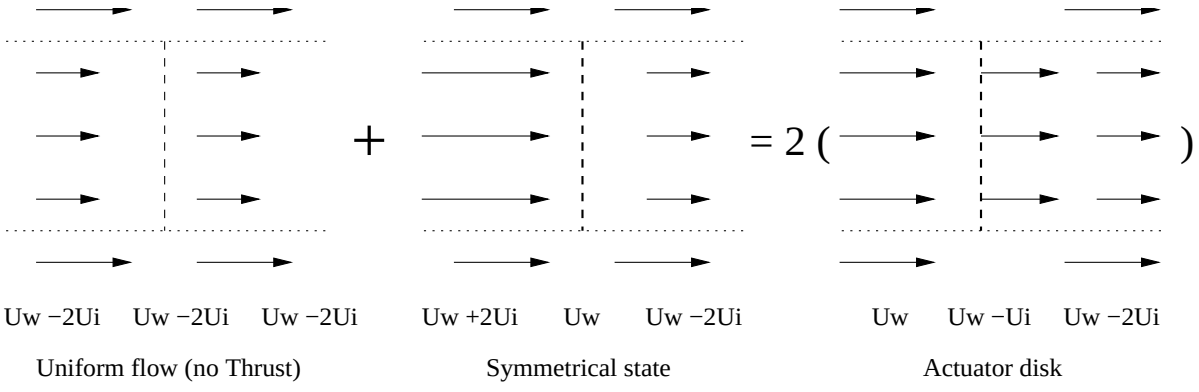

Figure 5.2 *Wake decomposition of an actuator disk*

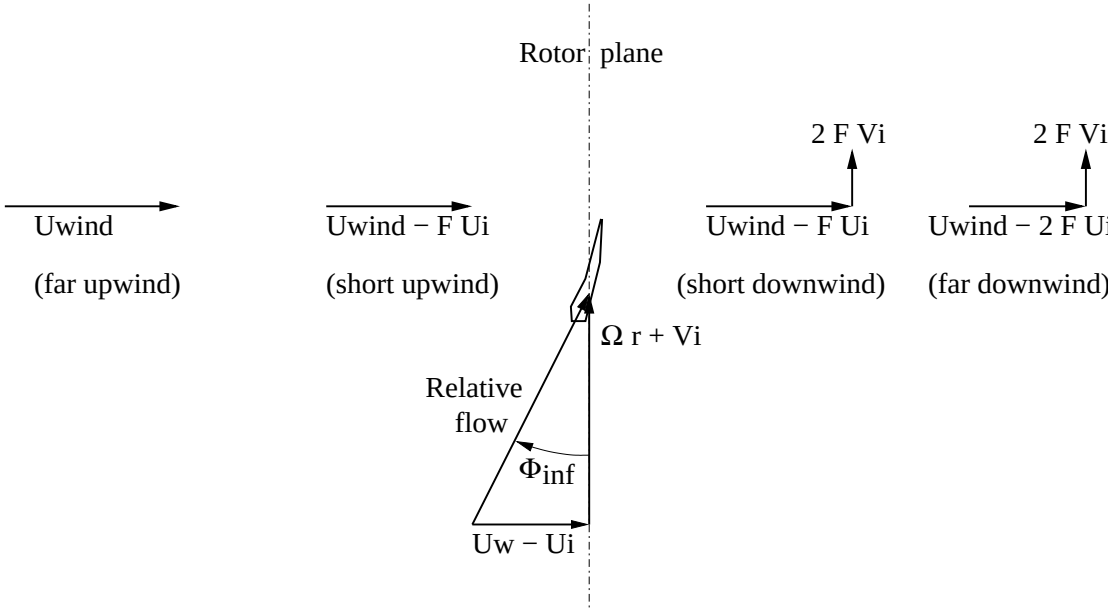

Figure 5.3 *Velocity distribution through the rotor plane*

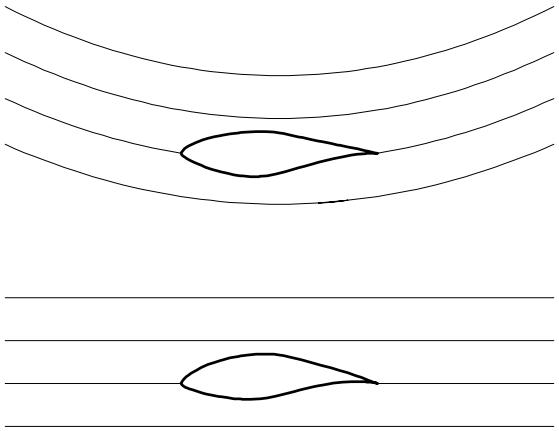

Figure 5.4 *Virtual camber of an airfoil in curved flow*

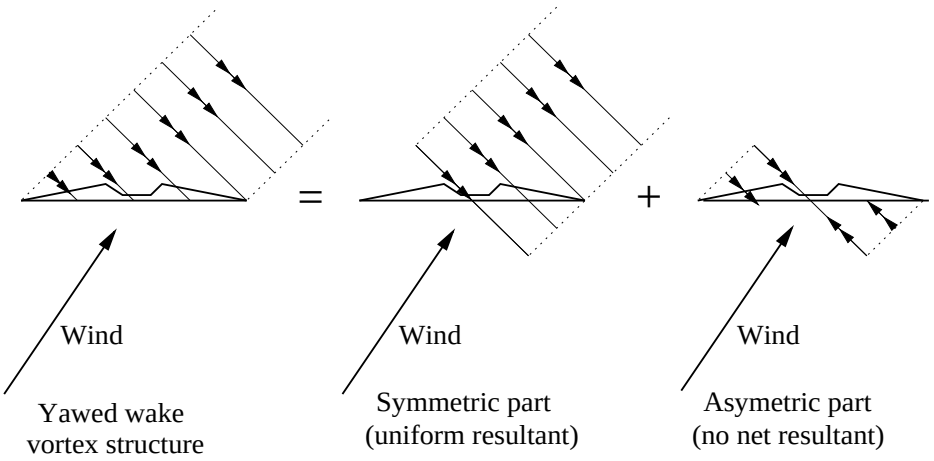

Figure 5.5 *Decomposition of wake geometry at oblique inflow*

6. BLIND COMPARISON CALCULATIONS

6.1 Introduction

In the spring of 2000 aerodynamic measurements are performed of the 10m diameter 2-bladed UAE phase-VI rotor of NREL in the NASA-Ames wind tunnel under various conditions. A description of the UAE rotor in the NASA-Ames wind tunnel is given in Appendix A A 'Blind Comparison' was coordinated by NREL, which dealt with the calculation of the aerodynamic loads for 20 measurement campaigns. These campaigns were selected from an extensive set of measurements and were all for quasi-stationary operation for a rotor speed of 72rpm and a 3deg blade pitch angle. All campaigns used for the 'Blind Comparison' were for the same rotor speed of 72rpm and the same blade pitch angle of 3deg. The scatter of this 'Blind Comparison' was the basis fur planning further investigations of the aerodynamics of rotating rotors, see also [43].

The characteristic conditions for this Blind Comparison were:

- For a windspeed of 15m/s the tip speed ratio is 2.53, which is low.
- A blade aspect ratio of 7.2, which is less than half the value of modern large wind turbines.
- Due to this aspect ratio, an aerodynamic solidity of 5.8% which is high for a 2-bladed rotor.
- A Lock number of 1 (very low) as a result of the large blade bending stiffness.

The relatively low rotor speed is a limitation to the aerodynamic thrust of the rotor, which means that the axial induced velocity will be a small fraction of the tunnel wind velocity. The result is that the aerodynamic loads are dominated by airfoil aerodynamics and that models for the rotor/wake aerodynamics can hardly be investigated. For the 72rpm rotor speed and 3deg pitch angle used for the 'Blind Comparison', the rotor-average induction factor calculated with PHATAS is drawn in Figure 6.1. Figure 6.1 shows that only for a wind speed below 10m/s the aerodynamic induction factor exceeds 0.1. With this low disk loading and the small ratio between rotor swept-area and tunnel cross-section (0.09) the tunnel-blockage effects are less than 1%. Sørensen e.a. [75] concluded however that near the beginning of stall (at 10m/s) the state of flow is rather unstable and can still be influenced by small blockage effects.

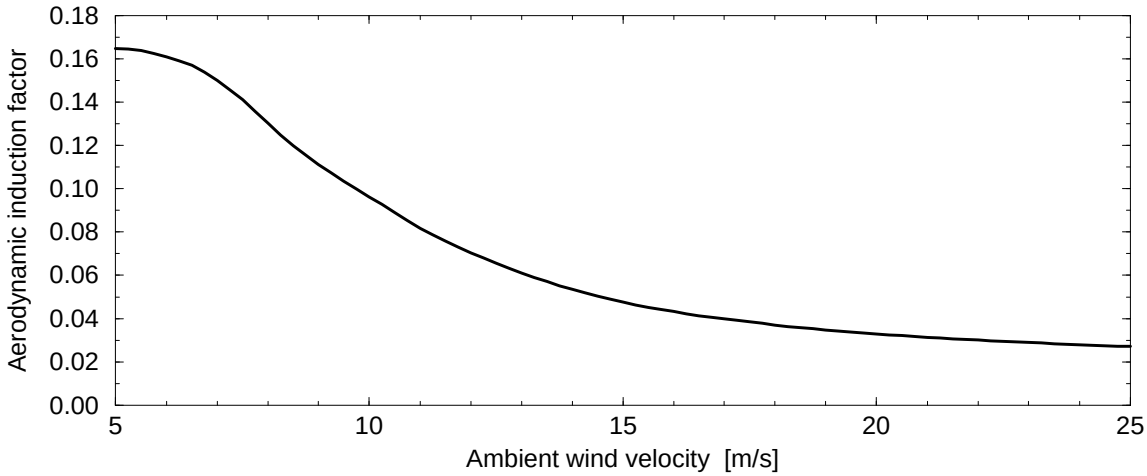

Figure 6.1 *Aerodynamic induction factor for 72rpm and 3deg pitch angle*

The measurement campaigns used for the 'Blind Comparison' can be divided in:

- Up-wind; Various wind speeds; No misalignment.
- Up-wind; Misalignments 10deg, 30deg, and 60deg; Wind of 10m/s, 13m/s, and 15m/s.
- Downwind; 0deg and 20deg misalignment; 7m/s and 17m/s wind.

Comparisons are presented between measured and calculated properties, all for the up-wind cases. This includes the results with the former PHATAS release "DEC-1999" (used for the Blind Comparison) and with the current PHATAS release "OCT-2002".

6.2 Modelling conditions for the Blind Comparison

The calculations for the Blind Comparison were performed with the modelling conditions and parameters similar as used for design calculations (IEC or G.Ll. load-sets) which implies:

- Tower bending;
- Blade bending, in flapwise and lead-lag direction;
- Rotor shaft torsion;
- Generator characteristics, here for an asynchronous generator;
- Using a firs order dynamic stall model.

In addition to this, the blade torsional deformation was modelled because of its direct effect on the angle of attack, which is important for comparison of the results with measurements.

The time increment is 0.005s. For a rotor speed of 72rpm this means 240 solutions per revolution, which is slightly higher than for other turbines analysed with PHATAS (200 solutions per rev). This small time increment was chosen for the relatively high blade bending frequencies.

The '3D-correction' method on the coefficients for the effects of rotation was used. Because for most of the conditions the phase-VI rotor operates in stall, some comparative investigations were performed with different correction models.

6.3 Up-Wind, Zero Misalignment

The following measurement campaigns were for stationary operation:

Campaign	Wind	Yaw	Air density
`s0700000`	7.0m/s	0.0deg	1.246kg m^3
`s1000000`	10.0m/s	0.0deg	1.246kg m^3
`s1300000`	13.1m/s	0.0deg	1.227kg m^3
`s1500000`	15.1m/s	0.0deg	1.224kg m^3
`s2000000`	20.1m/s	0.1deg	1.221kg m^3
`s2500000`	25.1m/s	-0.1deg	1.220kg m^3

See also the web-page `http://wind.nrel.gov/amestest` .
For each campaign also the rotor speed was given by NREL. However, the PHATAS calculations were performed with the asynchronous generator model so that the rotor speed is part of the result.

On basis of the air densities of the other non-yawed rotating measurements, the calculations up to and including 10.1m/s wind were done for an air density of 1.245kg/m^3 and the calculations for higher wind speed values were done for an air density of 1.225kg/m^3. These air densities differ not more than 0.2% with the measurement conditions.

To obtain the solutions for all these conditions easily, the response was calculated with PHATAS for a slowly increasing wind speed from 5m/s to 30m/s in 150s. This increase in wind speed is slow enough to give a quasi-stationary power curve. Here the calculations with the former PHATAS release "DEC-1999" were also repeated to account for the modifications of the input.

6.3.1 Results for the stationary non-yawed cases

In Figure 6.2 and 6.3 a comparison is given of the shaft torque and the blade root flapping moment. This flapping moment was at 0.432m from the rotor centre which corresponds with the specified strain gauge location. Because of the blade pitch angle this flapping moment differs 3deg w.r.t. the rotor plane direction.

Figure 6.2 and 6.3 also include the results calculated with BLADMODE, and those calculated by Risø with their 'EllipSys3D' code because during the Blind Comparison the latter code was found to be a high-level aerodynamic model.

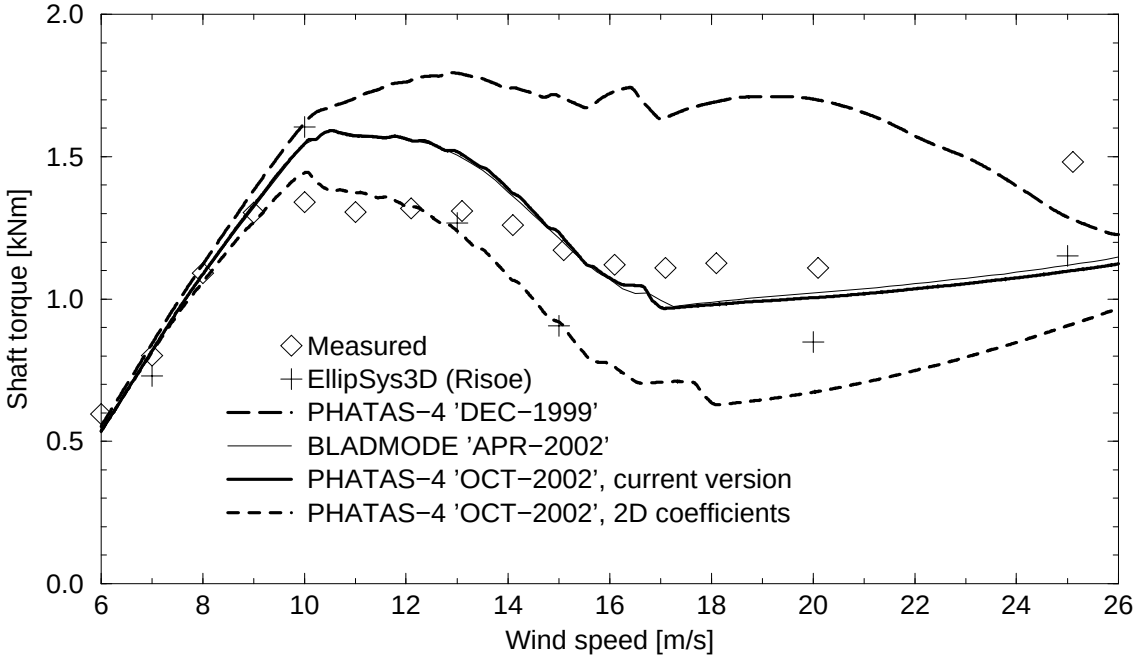

Figure 6.2 *Stationary shaft torque as function of wind velocity*

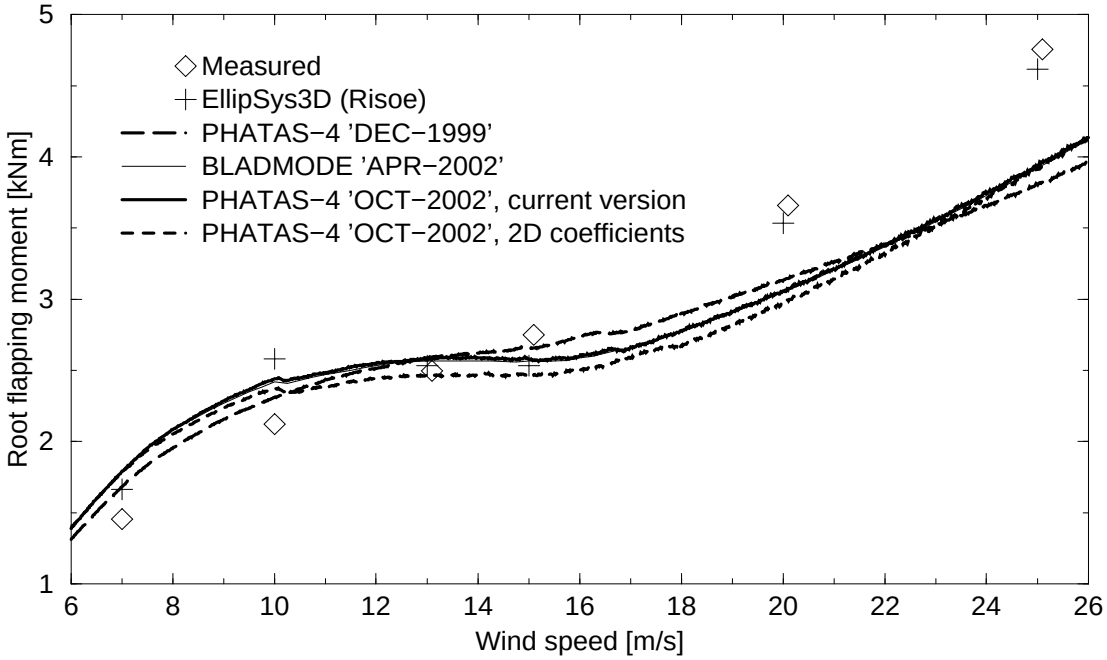

Figure 6.3 *Blade root flapping moment as function of wind velocity*

From Figure 6.2 and 6.3 it follows that the shaft torque calculated with the former PHATAS release, "DEC-1999", gives a strong over-estimation for a wind velocity from 10m/s to 22m/s. The reason for this over-estimation was that the model for correction of the rotational effects did not yet have the dependency on the local speed ratio λ_r. Another reason is that the correction of the lift coefficient decays to zero at an angle-of-attack of 50deg, instead of 45deg for the previous PHATAS versions. Calculations with a 'decay ending' at an a.o.a. of 55deg showed a better agreement with the measured shaft torque. Because these observations are based on measurements on only one rotor, this 'decay ending' was set (conservatively) to 50deg, see section 4.3.

The results calculated with BLADMODE and with PHATAS agree well because the algorithms for the rotor aerodynamics are based on the same theoretical models.

The 'waviness' of the shaft-torque shown in Figure 6.2 is caused by subsequent stalling of each of the blade elements, related to the strong drop in the lift coefficient and a strong increase in drag coefficient for an angle-of-attack between 17deg and 18deg, see Figure 3.16.

The under-prediction of the shaft torque calculated without the correction-model for rotational effects (Figure 6.2) shows that in stall the rotational augmentation has a dominating effect.

The shaft torque at 10m/s wind calculated without the non-rotating ('2D') coefficients is also larger than the measured shaft torque. For a 10m/s wind, Sørensen et al. found that the blades start to stall which is rather unstable. The unstable state may be sensitive to small effects such as the tunnel blockage effect of about 1%.

6.3.2 Sensitivity to numerical and modelling aspects

In order to obtain insight in the influence of the numerical and modelling conditions of the PHATAS calculations, the stationary operational state was also calculated:

- with a wind speed that increases 2 times as fast;
- with 10 blade elements instead of 17;
- without blade bending and torsional deformation;
- using the PHATAS option for a power curve calculation.

The stationary state was also calculated without the dynamic stall model, which showed nearly identical results as with the dynamic stall model. The shaft torque from these calculations is plotted in Figure 6.4. From the fact that the lines in Figure 6.4 nearly coincide, it follows that the calculations shown here were affected marginally by the modelling conditions. The calculation with 10 elements shows a different 'waviness' in the shaft torque because the blade elements stall at a different wind speed. The calculations with a faster increasing wind speed show slightly larger values for the shaft torque, which means that for this wind the wake is not completely stationary.

The quasi-stationary rotor characteristics are calculated with PHATAS for a 3deg pitch angle. Here the '3D-correction' method is included. Similar as for the tip-losses, the root-losses are accounted for with the factor of Prandtl, using a 'root-vortex radius' of 1.07m.

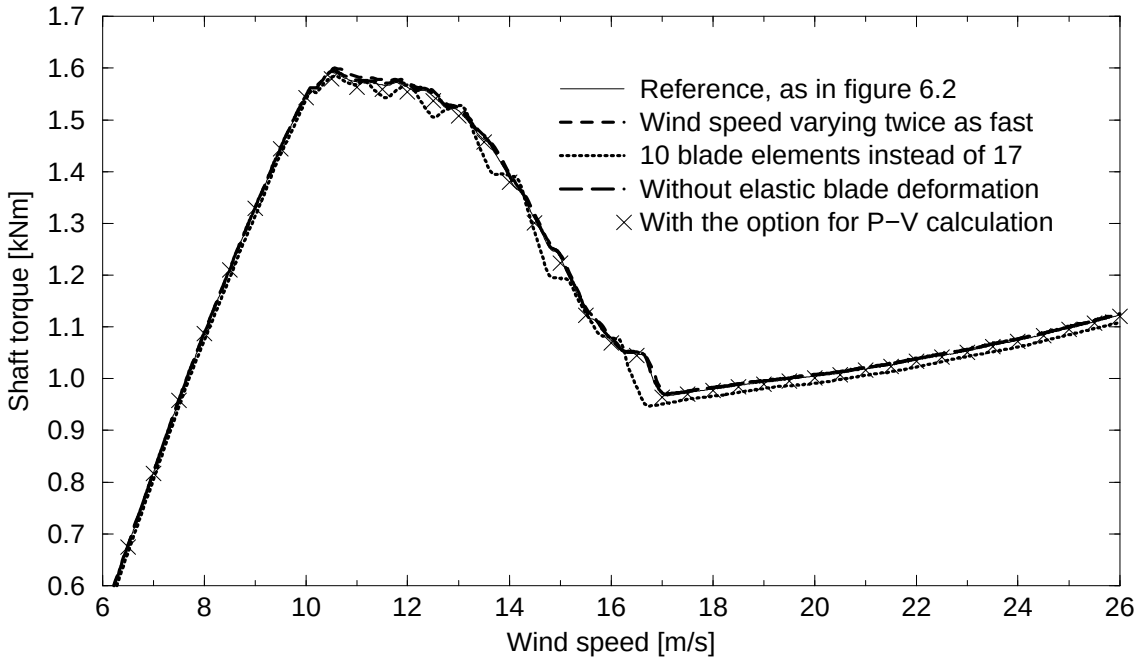

Figure 6.4 *Stationary shaft torque calculated for several conditions*

6.3.3 Influence of the non-rotating aerodynamic coefficients

The documentation provided to the participants of the Blind Comparison contained tables with aerodynamic coefficients from different wind tunnels, and also for different Reynolds numbers. Before and also after this Blind Comparison it was already mentioned that the calculated results depend strongly on the choice of the tables with aerodynamic coefficients.

Knowing that the Reynolds number of the measurements in the NASA-Ames wind tunnel is near $1 \cdot 10^6$, only the aerodynamic for this (or closest to this) Reynolds number are considered. To investigate the influence of the airfoil coefficients table used, the stationary aerodynamic power curves are calculated with PHATAS using the data from:
TU-Delft For Re = $1 \cdot 10^6$, deep-stall from *StC* ;
TU-Delft Idem, modified by Timmer (Nov. 2000) [81], and finally used here.
Ohio State Univ For Re = $0.65 \cdot 10^6$, deep-stall from *StC* .
Ohio State Univ Idem, with angle-of-attack shifted -0.53deg.
Colorado State Univ For Re = $0.65 \cdot 10^6$, with measured deep-stall coeff.
The coefficients from these wind tunnels are plotted in Figure 3.4. From Figure 3.4 it follows that the OSU wind tunnel data are 'shifted' compared with the other data, for which W.A. Timmer (TU-Delft). suggested a correction or 'shift' of -0.53deg (November 2000) [81].

Except for the coefficients from the CSU wind tunnel, the aerodynamic coefficients in deep-stall are generated with *StC* for an aspect ratio of 7. The shaft torque resulting from these calculations are plotted in Figure 6.5 together with the measured values and the torque from the calculations by Risø with EllipSys3D. These calculations are performed with the '3D correction' model of Snel e.a. and with the empirical model for reduction of the coefficients near the blade tip.

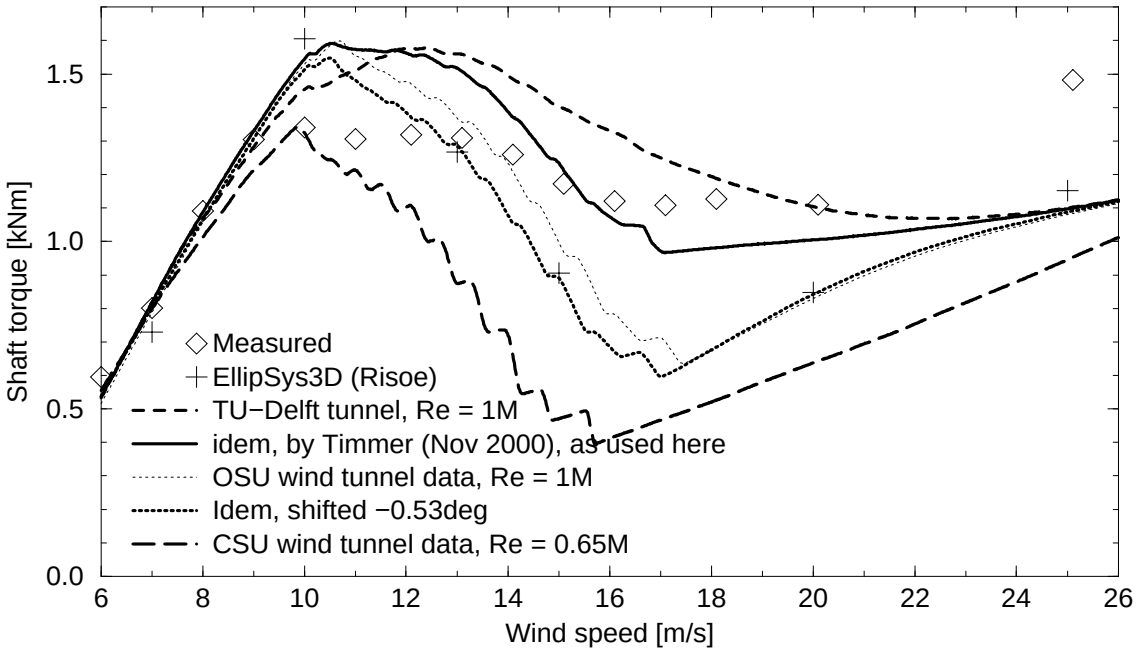

Figure 6.5 *Stationary shaft torque calculated with different coefficients files*

Figure 6.5 shows a strong influence of the choice of the stationary airfoil coefficients file.

The differences in shaft torque from 14m/s to 20m/s reflects directly the lift coefficient for 'stall' angles-of-attack near 20deg, see Figure 3.4 and 3.15. The shaft torque calculated with the CSU coefficients is low because the maximum lift is smaller (low Reynolds number), and because the slope of the linear part of the lift curve is smaller. Both these reducing aspects are "amplified" by the fact that the lift coefficients from the CSU wind tunnel are below those for the 'potential lift' which means that the reduction in coefficients towards the tip is stronger.

For wind velocities near 25m/s the results calculated with the TU-Delft data and with the OSU data approach to each other which is because for both these tables, the deep-stall coefficients are generated with *StC* .

It is remarkable that the TU-Delft data directly from the Blind Comparison documentation, and those corrected by W.A. Timmer show such a large difference while for both cases the deep-stall coefficients have been generated with *StC* .

6.3.4 Influence of the models for rotational effects

From the results in the previous section, it follows that the correction on the lift coefficients for the effects of rotation have a dominant influence on the calculated results, in particular on the aerodynamic power and the shaft torque. An investigation was performed into the influence of different models for the effects of rotation that were described in section 4.3, 4.4, and 4.5. The main difference of the model based on centrifugal pumping compared to that of Snel et al. [71] is that this model described an enhanced normal force instead of an enhanced lift, which implies in increased rotational drag coefficient. Other differences between these models is the dependency on the c/r ratio instead of a quadratic dependency, and a dependency on the size $c(1-f)$ of the stalled volume of air. The 'stall delay' to larger angles-of-attack has not yet been included.

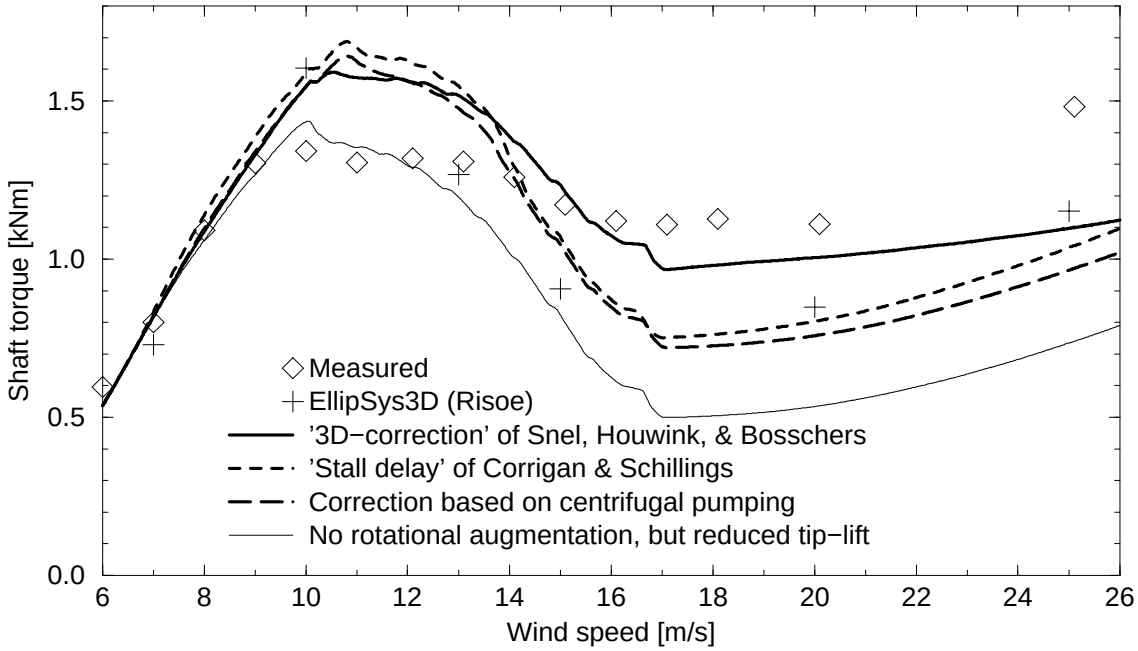

Figure 6.6 *Stationary shaft torque for different correction models*

The results calculated with the correction models described in chapter 4 are plotted in Figure 6.6 and 6.7. These graphs show that the (models for) rotational effects do have a strong influence. In particular because the UAE phase-VI rotor has a small aspect ratio (and thus a relatively large c/r ratio) but also because in general the correction models may be scaled different for different rotors (as was mentioned in the description of the Corrigan-Schillings model [14]) one should not judge too easily on the amount of correction. Instead, one should try to learn from the trends of the correction methods.

Although the quadratic c/r dependency of the model of Snel et al. [71] is stronger than follows from theory, the calculations with this model show a good trend with the measured shaft torque.

The alternative model based on centrifugal pumping gives a blade root bending moment of which the trend fits better with the measurements on the phase-VI rotor, and also with the results calculated

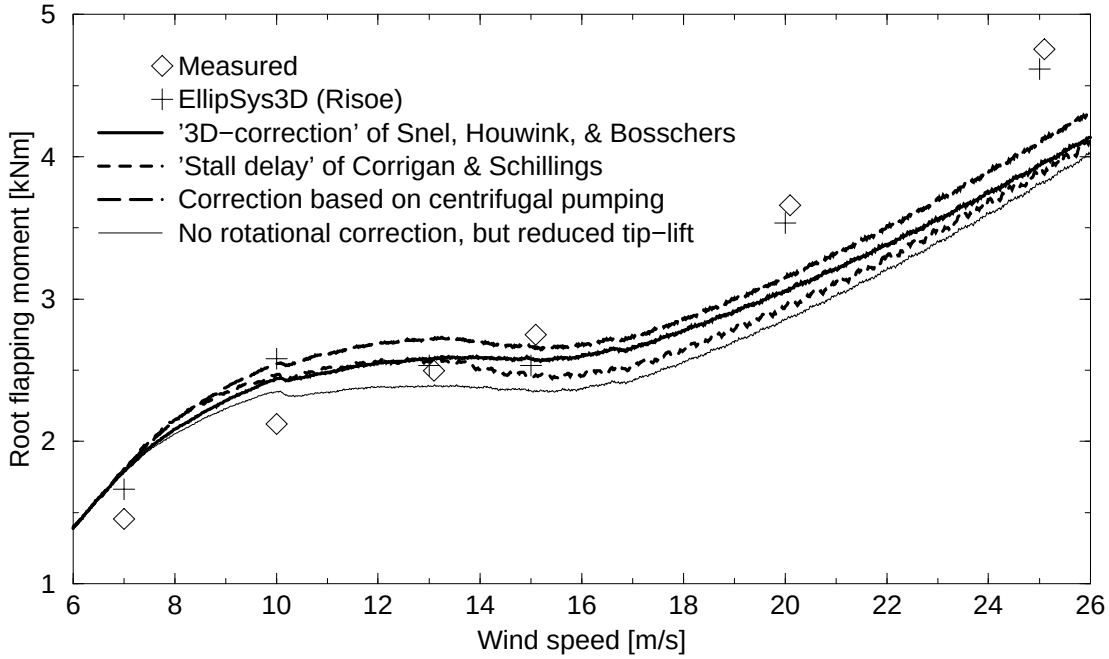

Figure 6.7 *Blade root flapping moment for different correction models*

by Risø with their EllipSys3D code.

At first sight the results with the 'stall delay' model of Corrigan & Schillings look reasonable, but they give an over-prediction of the shaft torque for non-stalled operation and are thus too optimistic for performance calculations. This 'optimism' may be reduced by adding an increase of the drag coefficient, based the energy (shaft torque) needed for centrifugal pumping of the radial flow. The Corrigan-Schillings method does not show much effect for the blade root flapping moment, see Figure 6.7, which is caused by the smaller drag coefficients for the rotating state.

6.3.5 Influence of tip aerodynamics

Some of the improvements of the program PHATAS are on the implementation of the tip-loss factor, and on the reduction of aerodynamic lift coefficient at the tip. An investigation was performed by calculation of the power curves calculated with different modelling of the tip aerodynamics.

- without tip-loss factor and without lift-reduction;
- with the tip-loss factor calculated for a trailing-vortex distance following the local inflow direction ϕ_{inf};
- with the reduction in lift coefficients and the tip-loss factor as implemented in PHATAS.

For these calculations the rotational effects are included using the '3D-correction' model of Snel et al. The empirical model for reduction of the lift coefficients towards the tip is described in section 4.6.

The resulting shaft torque is shown in Figure 6.8. For the low wind speed values, Figure 6.8 shows that with the current PHATAS release the shaft torque is slightly smaller than for the classical implementation on basis of local inflow direction. This eliminates the 'classical' over-estimation of the calculated wind turbine performance, in particular for 2-bladed wind turbines. For the higher wind speed values it appears that as a result of the tip-loss factor, the blades stall at slightly higher wind speed values. For further analysis of the NASA-Ames measurements this means that the modelling of the tip-losses should be taken into account.

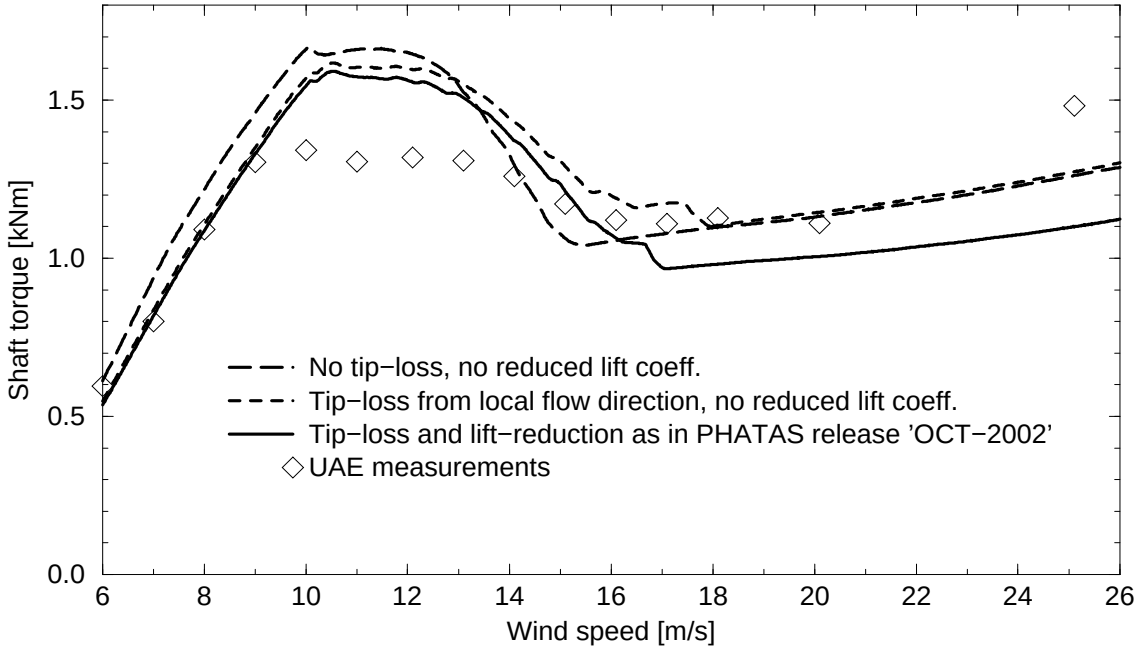

Figure 6.8 *Stationary shaft torque for different tip-loss modelling*

The differences for the higher wind speed can not be evaluated quantitatively since they depend also on the models (with its scaling factor) for deep-stall coefficients and for rotational augmentation.

6.4 Up-Wind, Yaw Misalignment

The calculations for stationary operation with misalignment were performed for a given wind speed, and with a very slow yaw rate of 0.8deg/s. This slow yaw action was calculated from -20deg to 70deg such that from the 'symmetry' with respect to the zero-yaw direction, one can evaluate whether the yaw rate is slow enough to be quasi-stationary.

For the wind velocities of 10m/s, 13m/s, and 15m/s that were also part of the 'Blind Comparison' the stationary behaviour was calculated with PHATAS. These calculations correspond with the measurement campaigns:

Campaign	Wind	Yaw	Air density
s1000100	10.1m/s	10.0deg	1.246
s1000300	10.1m/s	30.2deg	1.246
s1000600	10.1m/s	60.0deg	1.246
s1300100	13.1m/s	10.1deg	1.227
s1300300	13.0m/s	30.0deg	1.227
s1500100	15.1m/s	10.0deg	1.224
s1500300	15.1m/s	29.9deg	1.225
s1500600	15.1m/s	60.0deg	1.225

The aerodynamic power from these calculations are plotted in Figure 6.9.

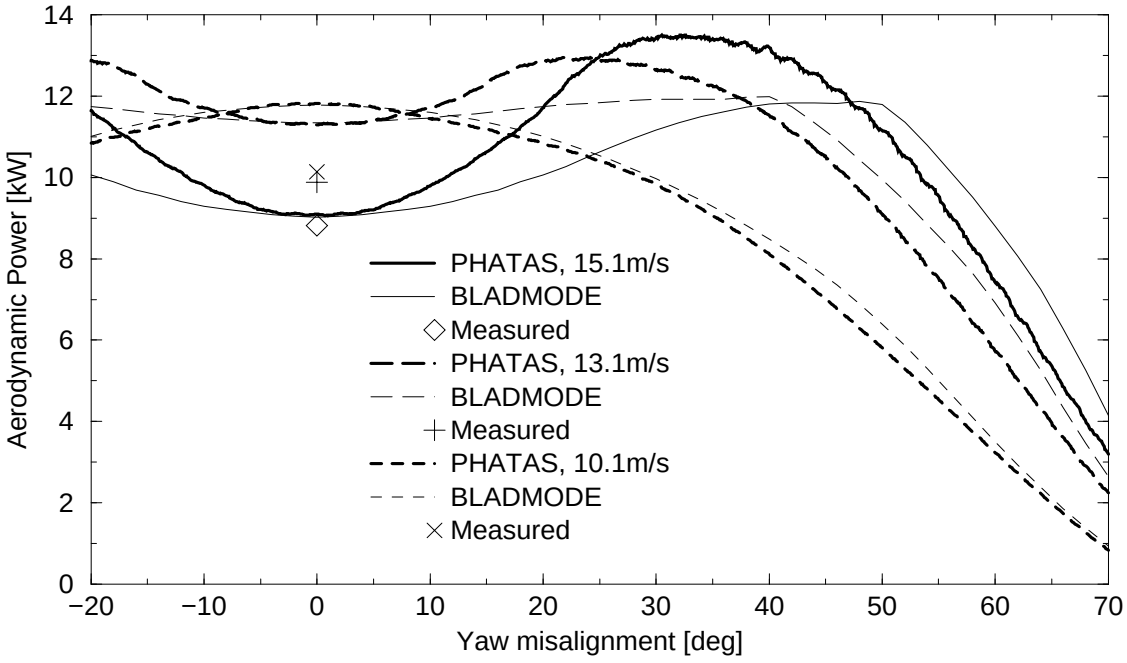

Figure 6.9 *Average aerodynamic power as function of misalignment*

From the PHATAS results in Figure 6.9 it follows that the yaw rate has been small enough to give a 'symmetric response' and thus quasi-stationary behaviour. For the higher wind velocities a yaw misalignment gives an increase in aerodynamic power because then the rotor gets out of stall.

For a series of yaw angles and a wind velocity of 10.1m/s and 15.1m/s the stationary aerodynamic power was also calculated with BLADMODE. For the smaller wind velocity of 10.1m/s the more simplified aerodynamic model in BLADMODE shows a reasonable agreement with the PHATAS results. For the higher wind velocity of 15.1m/s where the wind turbine is in stall the model of BLADMODE shows serious deviations for yawed operation.

7. CONCLUDING REMARKS

Investigations have been performed into the measurements on the UAE phase-VI rotor in the NASA-Ames wind tunnel. On basis of these measurements and on basis of the existing knowledge from literature, the stationary aerodynamics of rotating rotor blades have been investigated. The measurement conditions of the phase-VI rotor do not have a large induced velocity which means that they have little information for investigation of the rotor wake. Still the measurements can be used to investigate the reduction in angle-of-attack towards the blade tip ('tip loss'), where the induced velocity increases as a result of the flow around the blade tips. Expressed in terms of vorticity, this means that near the tips the induced velocity from the tip vortex is large. In fact the downwind average induced velocity was small for the UAE rotor in the NASA-Ames tunnel.

Because of the large amount of data and the complexity of rotor aerodynamics and with regard to the start-up of the IEA Annex-XX work, which also dealt with the analysis of the NASA-Ames measurements, the investigations reported here were limited to the stationary state. This deals with the aerodynamic airfoil coefficients, the effects of rotation, and the implementation of some aspects of the Blade Element Momentum models such as PHATAS. Investigations into the effects of dynamic stall have been postponed to future research (e.g. in Annex-XX) because *investigating dynamic stall only makes sense if the stationary rotating conditions are well-understood*.

7.1 Results

7.1.1 Literature survey

In order not to 'reinvent the wheel' a large number of publications (nearly 400) have been collected and investigated. A lot of insight has been obtained from these publications, which forms a basis for analyses of the measurements and for the development of the improved models.

7.1.2 Improvements of the empirical deep-stall coefficients tool 'StC'

The tool *StC* has been developed at ECN for the prediction of the aerodynamic coefficients in deep stall. On basis of measured aerodynamic coefficients from various publications (mainly on vertical axis wind turbines) the empirical expressions in *StC* have been improved (see section 2.3):

- Add the 'skewness' of the normal-force coefficient with respect to the 90deg angle-of-attack.
- A model for the tangential-force coefficient in deep-stall.

7.1.3 Rotor-aerodynamics analysis tools 'inflow' and 'beminf'

In general measurements have the advantage that they represent the real phenomena. For the aerodynamics of a rotating rotor, measurements may give the real distribution of the normal- and tangential- forces. For a rotating rotor blade the angle-of-attack is hard to obtain because of the strong variations of the induced velocity near and around the rotor. On basis of the assumption that the trailing vorticity is related to the aerodynamic lift on the airfoil, and an assumption for the geometry of the wake vorticity, the program *inflow* has been developed for the calculation (by Biot-Savart integration) of the induced velocities in the rotor plane. By an iterative process for the induced velocities, the aerodynamic angle-of-attack and the lift- and drag- coefficients is obtained. The program *inflow* has been written for general type of rotors of which the blades (in fact their loading) are identical. For model-evaluation of *inflow* a similar tool *beminf* has been developed on basis of an inverse BEM approach. Both these tools have undergone some validation, including a comparison with the vortex-wake based tool 'LSWT' used by Tangler [78]. This comparison showed that in particular for non-stalled operation, the tool *inflow* works well which means that *inflow* can be used for further analyses within the MEXICO project and the IEA Annex-XX project.

7.1.4 Improvements of the BEM-based codes BLADMODE and PHATAS

In general the results from all participants of the Blind Comparison in the fall of 2000 showed a large scatter. The results of the ECN calculations were roughly in the middle of those from the other participants while they were not extremely far off from the measurements.

With the modifications on BLADMODE and PHATAS that were issued within this project, the agreement between measured and calculated rotor performance has been improved. However the spanwise distribution of the blade loads still shows serious differences with the measurements, in particular towards the root and tip regions.

Improvement of the Model for Rotational Effects of Snel et al. :

The correction method on the lift coefficient of Snel, Houwink, and Bosschers [71] for the effects of rotation originally prescribes a decay to the 2D coefficients from 30deg to 45deg angle-of-attack. On basis of comparison between measured and calculated rotor shaft torque for the phase-VI rotor it was found that the decay to the 2D coefficients should be at higher angles-of-attack. For the phase-VI rotor it was shown that a decay to the 2D data at 55deg fits even better with the measurements. The 50deg a.o.a. was chosen for conservatism because it is based on measurements of a single rotor, which has e.g. a relatively low aspect ratio.

Reduction of the lift towards the tip :

For the root and midspan region of the blades, the centrifugal loads on the boundary layer and the separated flow area drives the air in radial direction, which gives a "delay of stall". For the tip region, the radial suction from centrifugal loads and the spanwise pressure gradient is absent while air from the midspan region still enters the boundary layer of the tip region. As a consequence, the pressure distributions for the tip sections will not obtain the negative suction areas compared to the 2D state. In other words, for angles of attack larger than those for laminar flow the lift coefficients are smaller than in the 2D state. An empirical correction model has been formulated that describes this reduction of the lift coefficients near the tip. This empirical correction has been implemented in the programs BLADMODE and PHATAS.

Improved modelling for the tip loss factor :

Both the programs BLADMODE and PHATAS use the well known tip loss factor of Prandtl. Although this factor looks well-defined, it is formulated in terms of the distance between the trailing vortices for which several interpretations are possible. The algorithm for the tip loss factor has been improved by using the average velocities in the wake close behind the rotor. The result is a small reduction of the performance calculated for pitch-to-vane controlled wind turbines, which is stronger for 2-bladed rotors than for 3-bladed rotors.

As a result, the general opinion that *'the calculated performance for 2-bladed rotors is over-predicted*' is partly eliminated. Another reason for the over-predicted performance of 2-bladed rotors is the fact that real rotor blades have higher aerodynamic drag coefficients caused by inaccuracies of the airfoil shape near the leading edge and caused by dirt. With their smaller tip-speed, the performance of 3-bladed rotors is less influenced by (an increased) drag so the mis-prediction due to dirt is smaller.

7.2 Conclusions

7.2.1 Conclusions on the measurements of the UAE phase-VI rotor

Conclusions on the measurements

Tunnel blockage effects :

For the measurement conditions of the UAE rotor in the NASA-Ames wind tunnel the induced velocities in the wake are low. For a wind speed of 10m/s or more they are below 10% of the tunnel wind velocity. For the small rotor-swept area this means that the effects of tunnel blockage are 1% or less, for which corrections do not appear to be necessary. Sørensen reported [75] that for a wind speed of 10m/s the rotor blades just start to stall which is a rather unstable state. For this state small disturbances such as tunnel-blockage effects may have some influence, which is reflected by the over-predictions of the calculated shaft-torque for 10m/s wind.

Reliability of the measurements :

NREL has already been monitoring the quality of the measurements in the NASA-Ames wind tunnel by investigating the repeatability of the same measurements after several days, see Figure 4 and 5 of [26]. This repeatability appeared to be good.

In the analyses of the non-rotating measurements reported here it followed that the aerodynamic coefficients obtained from measurements at 20m/s and at 30m/s were highly similar. This shows that the S809 airfoil is not very sensitive for a Reynolds number variation of about 1.5.

Pitch/Yaw error for the non-rotating conditions :

The 1.0deg discrepancy of the angles-of-attack of the non-rotating aerodynamic coefficients for the S809 airfoil was not resolved. For coefficients obtained from pressure-tap measurements, a deviation can occur if too few pressure taps are used near the leading edge where pressure gradients are large. For the tangential-force coefficients, deviations may also occur with too few pressure taps in the 'cusp' of the airfoil trailing-edge. The aerodynamic coefficients from the rotating measurements however do not show to have such a discrepancy. Therefore it was thought that this discrepancy may be from either a yaw misalignment of the rotor in the wind tunnel, a local deviation of the tunnel wind-direction, or an effect with a similar influence.

Rotating sectional properties of the root and the tip :

The aerodynamic coefficients near the blade-root and near the blade-tip are strongly affected by the radial flow components. In the analysis of the measurements, the coefficients can be 'matched' to some extent by shifting the radii of the root-vortex and the tip-vortex. However, the coefficients for the 30.0% and to a less extent for the 95.0% sections of the phase-VI rotor still show deviations with respect to the 2D values, even for the non-rotating measurements.

Recommendations for modelling the UAE phase-VI rotor

On basis of the findings during the work for the underlying report the following recommendations are given for modelling and investigations within the IEA Annex-XX project.

- Participants of the IEA Annex-XX project should take care of the given definition of the blade pitch angle: the twist distribution as specified has to be increased with +1.775deg.
- The choice of the 'root-vortex-radius' is significant for all analyses in which the induced velocity is involved, such as the reconstruction of the angle-of-attack with e.g. the inverse vortex-wake model of *inflow* or with *beminf*.
- The rotor blades are relatively stiff (Lock number of 1). Because up to now only the stationary conditions were analysed, this high stiffness has little influence. For the investigation into instationary aerodynamics also the blade flexibilities have to be correct, which means that the specified stiffnesses have to be reduced slightly, see also chapter 6 of [39] by Jonkman.
- Mainly because most of the measurements were performed for stalled conditions, the choice of the non-rotating airfoil coefficients file has a strong influence on the calculated results.

7.2.2 Conclusions on deep-stall coefficients

Because the effects of rotation play a dominant role and because most models for the effects of rotation are formulated in terms of a correction on the non-rotating coefficients, these coefficients have to be available for all angles-of-attack. The aerodynamic coefficients are usually available for angles-of-attack up to 20deg, while the coefficients for larger angles-of-attack are added with empirical methods.

From the investigations into the aerodynamic coefficients in deep stall, it was concluded that the influence of the 'Aspect Ratio' of the blade in deep-stall is hard to model, even if it is treated as a flat plate. The findings are:

Drag of a flat object perpendicular to the wind depends on 'vortex shedding' :
For a small aspect ratio, a flat plate perpendicular to the wind (either rectangular, square, or round) has a drag coefficient of about 1.2. A very long or 2D plate has a drag coefficient of about 2.0 which is higher because of periodic vortex shedding. So the 90deg drag coefficient depends on whether vortex shedding takes place or not, which is badly defined for aspect ratios between 10 and 30. (A modern large rotor blade has an aspect ratio of 15 to 20.)

'Vortex shedding' is badly defined for a tapered rotor blade :
For the tapered planform of rotor blades the vortex shedding frequency may be different from the root to the tip. For this geometry periodic vortex-shedding is less likely to occur so that it is expected that the drag coefficients in deep-stall are smaller than for a rectangular planform.

The 90deg drag should be investigated for gust loading :
For the extreme (design-driving) gust loads the occurrence of vortex-shedding has not been investigated.

Nevertheless the influence of the 'Aspect Ratio' is modelled in *StC* with a continuous relation. It is recommended to apply *StC* with a not too small Aspect Ratio, because certification authorities sometimes prescribe a deep-stall drag coefficient of 1.3 to 1.35.

Optional improvements of ATG

At ECN the tool ATG (**A**ero **T**able **G**enerator) has been developed for the generation of the aerodynamic coefficients of any airfoil [9]. The basis of ATG is a database, in which interpolation is applied on basis of airfoil geometry. In practise the tool ATG is applied to retrieve coefficients that are used for the aerodynamic design of rotor blades, e.g. with the tool BOT (**B**lade **O**ptimisation **T**ool). Part of this aerodynamic design is the blade twist distribution, which implies that the aerodynamic coefficients shouldn't have an error in the zero-lift angle-of-attack.

- The improved empirical relations for the deep-stall coefficients that are formulated here can be implemented in the program ATG. (**A**ero **T**able **G**enerator).
- From investigations reported here into the measured and calculated aerodynamic coefficients for the S809 airfoil it was found that the method of Pankhurst can be used successfully to calculate the angle-of-attack for zero-lift. Because this method is based on thin airfoil theory and assumes fully laminar flow, the shape of the trailing-edge of the S809 airfoil (with the finite wedge angle) was somewhat smoothed. The method of Pankhurst also appeared to be suitable for the calculation of the aerodynamic moment coefficient in laminar flow.

  Based on the reasonable agreement for the S809 airfoil and on an even better agreement for other airfoils (NACA-6 series) it is recommended to use the engineering method of Pankhurst in the tool ATG. As a result, the coefficients-files generated with ATG can be used properly for the (optimised) design of the blade twist distribution.

7.2.3 Conclusions on rotational augmentation

Because the aerodynamic loads for a rotating blade play a vital role for the design and analysis of a HAWT, it was given special attention in the investigations reported here.

A complete model has not yet been developed but a lot of insight is obtained from both literature and the measurements on the UAE phase-VI rotor. Centrifugal and Coriolis- effects on the flow of rotating rotor blades result in the following phenomena:

1. The centrifugal loads on the boundary layer and the separation bubbles cause a delay of flow transition to larger angles of attack and a delay (or absence) of leading-edge stall. The latter implies that stall starts at the trailing edge and develops to the leading edge.
   In practise this means that prior to increasing the lift- or normal-force coefficient, some *basic correction* should be applied to the non-rotating coefficients that describes the delay/absence of leading-edge stall.
2. The fact that the centrifugal loads also act on the boundary layer and finally drives the boundary layer to larger radial locations where it gets thinner, implies that *rotating rotor blades have a smaller Reynolds-number dependency than non-rotating blades or wings*. This should be accounted for by the 'basic correction'.
3. Suction on the separated flow area gives an increased normal force (some authors describe an increased lift) for a given separation-point location, while a given separation-point location may occur at a larger angle-of-attack. The first effect is described by many models for rotational augmentation such as the model of Snel e.a. (section 4.4) or the model based on the 'centrifugal pumping' equations (section 4.3). The second effect is described by the correction method of Corrigan-Schillings (section 4.5).
4. The rotational effects on the blade-root region are stronger than what is predicted following the model(s) based on 'centrifugal pumping', which have a linear c/r dependency (section 4.3). The reason is that no air is "injected" from smaller radial locations while the outer locations are still "sucking" air. In the absence of a proper model for this strong local effect near the root, the quadratic c/r dependency of the model of Snel e.a. appears to be a reasonable and practical fit for the spanwise distribution of the rotational effects. Here one should realise that although the lift coefficient near the root is high, the lift itself is of moderate magnitude.
5. The lift coefficients on the tip of a rotating blade are smaller than those on a non-rotating blade. An explanation is that the inboard locations "pump" air towards the tip such that the suction-side of the tip airfoils will never develop very strong negative pressures. For this lift-reduction towards the tip, an empirical model is given in section 4.6. The question 'whether to apply this reduction on the lift- or on on the normal force coefficient' was not investigated.

In addition to the widely known observations of '*delay of stall*' or '*increased maximum lift*' (which is stronger near the root) the following conclusions are drawn here.

Dependency on the local speed ratio On basis of the equations for 'centrifugal pumping' or on basis of the 'boundary-layer equations' [5], it follows that the effects of rotation are proportional to $(\Omega r)^2$ while the aerodynamic coefficients are made dimensionless with ${V_{\text{eff}}}^2$. When one wants to derive Cl(α) polars for a given Ω and (pitch+twist), one can approach this 'speed-ratio dependency' by $(\Omega r/V_{\text{eff}})^2 \approx \lambda_r^2/(1+\lambda_r^2) = (\cos(\theta_{\text{tw}} + \theta_p + \alpha))^2$.

Rotational effect on drag coefficient The delay of stall and the delay/absence of local separation bubbles cause some decrease in drag coefficients for small angles of attack. If the airfoil gets in stall, the centrifugal pumping of air requires energy from the rotor which must in some way lead to an increase of the drag coefficient. This increase was found on the UAE phase-VI rotor and by many other researchers, except by Madsen [48] who reported an increased drag for the NACA63-218 airfoil. However, in a later publication [49] Madsen included graphs with both increased lift and increased drag of a rotating blade with the NACA63-2nn airfoil.
For the (low-cambered) NACA63-218 airfoil a decrease of the lift is likely to occur since rotational effects may suppress its strong leading-edge stall.

Difficulties in modelling rotational augmentation

Some of the difficulties in modelling the stationary flow of a rotating rotor were already described by Tangler in Appendix P of the 'measurement planning document' by Simms e.a. [70].

1. Rotational effects can be predicted easily for T.E. separation, while rotational effects may lead to delay or suppression of L.E. separation and local separation bubbles. This means that the correction models for T.E. separation only give realistic results if the (omission of) effects of L.E. separation bubbles and L.E. -stall are already accounted for.
2. Although an empirical expression is given for the decay of sectional coefficients towards the tip (section 4.6) end-effects of the blade are hard to include on basis of sectional coefficients. See also Appendix P of [70].
3. Correction models apply only to stall of the complete blade for which radial flow can run from the root to the tip. In practise local stall can occur, which appears to be stable for some of the rotating conditions of the phase-VI rotor with the S809 airfoils, see Tangler [78].

Evaluation of Models for Rotational Augmentation

In general most empirical models are formulated as function of the ratio $(chord/radius)$, sometimes called 'local solidity'. On basis of the mechanism of 'centrifugal pumping' this dependency appears to be linear.

For most of the phenomena associated with rotation, it can be derived that they are proportional to the speed ratio $(\Omega r/V_{\text{eff}})^2$. This speed ratio dependency has been added in earlier PHATAS versions to the correction method of Snel et al. such that transitions from non-rotating states to the rotating states can be calculated well. On basis of the spanwise distribution of the maximum lift coefficient and also on basis of the shaft torque calculated for the non-yawed operational conditions of the 'Blind Comparison' the model of Snel e.a. appears to give a realistic approach. Here it is known that the quadratic (c/r) dependency does not apply to the mechanism of 'centrifugal pumping' but it fits well with the high lift coefficient at the blade root and the decrease (or inversion) of rotational augmentation towards the blade tip. As long as the local effects at the root and at the tip are not modelled, the method of Snel et al. shows to be useful.

7.3 Recommendations for Future Investigations

7.3.1 Recommendations for processing sectional blade loads

When retrieving sectional coefficients from pressure measurements on rotating rotors it is recommended in general to:

- Use the drag coefficient at the mid-span location(s) to correct for errors in blade pitch angle or systematic errors in the integration of the surface-pressure distribution. The criterion is that the 'laminar drag bucket' should have a horizontal 'bottom', at least without negative values.
- Next use the drag coefficients of the root and tip sections to find the root and tip vortex locations, also on basis of the 'bottom' of the laminar drag bucket. A complication is that for high blade loading, the radial locations of the tip and root vortices may differ from those for low loading.

7.3.2 Recommendations for investigating rotational augmentation

For a good understanding of the physical phenomena, one should avoid investigations by empirical fitting (such as $(c/r)^n$) because they may depend strongly on the type of rotor while fitting does not provide much insight. In this respect it has to be mentioned that the UAE phase-VI rotor has an aspect ratio (7.2) that is less than half the value for modern large size wind turbines.

For the work within the IEA Annex-XX project it is suggested here to investigate the location of the separation point, similar as the investigations by Schreck [64]. The accuracy may be limited by the finite number of pressure taps.

Avoid empirical fitting of the correction methods for 'tip-loss'

The correction method for tip-loss' (of Prandtl) describes the reduction of the inflow angle towards the end of the blade. This reduction of the inflow angle towards the blade tip depends on the distance between the trailing vortices.

In addition the aerodynamics at the blade tip deviate from the 2D coefficients because:

1. Aerodynamic coefficients (rotating-) are only well-defined for sections that are part of a quasi-infinite long blade.
2. In the rotating state the radial flow in the boundary layer runs towards the blade tip, which is not sucked away by centrifugal loads from outer sections. Instead, the air flows from the aerodynamic pressure side to the suction side, which means that the suction-side flow easily separates. As a result the suction-side of the tip sections will not develop very negative pressures so that the rotating coefficients remain even below the non-rotating values.

Both these effects depend on the (chord/radius) ratio of the blade tip.

On basis of the fact that the reduction in sectional properties and the reduction in inflow angle are different phenomena that depend on different properties of the blade it can be concluded that as long as the reduction in sectional properties is not modelled well, it makes no sense to formulate empirical fits for the tip-loss factor on basis of measured blade load distributions.

Suggestions for short-term follow-up work, e.g. in IEA Annex-XX

The investigations reported here concentrated mainly on the effects of rotation on the aerodynamic properties of a wind turbine rotor. These effects appear to be essential for the performance, the dynamics, and the design loads of wind turbines although modelling appears to be difficult. Based on the fact that the measurements on the UAE phase-VI rotor and also based on the fact that modelling of instationary effects has limited value when the stationary conditions are not known the following (subsequent) investigations are suggested here:

Evaluation of BEM models The 'Blind Comparison' held in the fall of 2000 showed a large scatter between the results calculated by the different participants. This indicates at least that this is either a discrepancy between the input descriptions of the UAE phase-VI rotor, or between the implementations of the BEM theory. At the IEA Annex-XX kick-off meeting it was already discussed to perform a short mutual comparison of the BEM-tools of the different participants for simple conditions and all using the same tables with aerodynamic coefficients. The stationary rotor properties listed in Appendix A.4 calculated with the aerodynamic coefficients in Appendix A.2 already provide a basis for such an evaluation.

Further assessment of the mechanism of centrifugal pumping The investigations reported here were based only on the rotating measurements for a 3deg pitch angle, for which the rotor is in deep-stall for most of the wind velocities. Measurements were also performed for blade pitch angles of 6deg for which the angles-of-attack are smaller. Analysing the measurements for the 6deg pitch cases and combining the results with those obtained for the 3deg cases must give more insight/confidence in the models that are described here. Questions to be solved are:

- What is the "basic" rotating lift and drag curve due to the absence of L.E. separation bubbles or stall. Here it is expected that stall of a rotating blade starts at the trailing edge and can be described with the expressions in section 4.3 derived for 'centrifugal pumping'.
- To what amount do rotational effects lead to a delay of stall to larger angles-of-attack and to an increase of the (normal-force) coefficients. Here it is recommended to base the 'delay-of-stall' part of the rotational effects on the angle-of-attack where "drag-stall" (strong non-linear increase) occurs.

Although these questions are 'too elementary to be challenging', their answers and results are essential to make investigations into instationary aerodynamics realistic.

7.4 State of the Art of Wind Turbine Design Codes

Current status

Based on the results of the Blind Comparison and on the experience with the existing program PHATAS in other joint European research projects, the discrepancies between BEM-based codes such as PHATAS and the aerodynamics of 'real' rotors are as follows.

Lets state first that: '*From investigations into the dynamic loads of wind turbines that are not in stall, most of the discrepancies between the different computer codes result from mistakes in the input files or inaccuracies in the description of the wind turbine*'. These discrepancies can not be reduced by application of a more complicated model for e.g. the structural dynamics.

If serious attention is paid to a proper input description of the wind turbine, it appears that the dynamic response is predicted reasonably well as long as the blades operate at small angles of attack and the rotor doesn't operate in the 'turbulent wake state'.

Within a European research project, see Snel and Schepers [72], models have been developed to describe the effects of instationary rotor disk loading and the asymmetric load distribution for yawed operation. Comparisons of the calculated results with measurements on real wind turbines and on wind tunnel models show that these models for the rotor wake show to be realistic.

For wind turbines operating in or close near stall the calculated power and thrust still show a difference with the measurements. For years this discrepancy has been related to the effect of rotor rotation which gives a delay of stall to larger angles of attack, see also chapter 4. On basis of measurements, empirical formulae have been developed to correct the lift coefficient for the effects of rotation. From the 'Blind Comparison' however it followed that in stall-operation the calculations show a large scatter, even after omission/correction of trivial mistakes such as input errors.

Based on the fact that the effects of rotation are among others a 'delay of stall' to larger angles of attack, it follows that also for pitch-to-vane controlled wind turbines with a relatively high blade loading it is necessary to have realistic values for the aerodynamic properties of the rotational state. In stall, the existence of radial flow on the suction side of the airfoils imply a strong interaction between the neighbouring blade sections (or 'elements'). From these observations it can be concluded that also vortex-wake models (that use tables with aerodynamic airfoil coefficients) will not perform much better than the conventional BEM models.

The discrepancies for the 'turbulent wake state' usually appear at the lower wind speed values which means that they do not contribute much to the overall design loads of a wind turbine.

7.4.1 Possible improvements of BEM codes

Within the assumption/concept of independence of the aerodynamics of neighbouring elements or annuli, the current generation of BEM-based codes can still be improved by:

1.A Root-vortex location

Some of the models in BEM codes already use the radius of the root vortex, such as the model for oblique inflow by Schepers, and the tip-loss models. For the smooth transition between hub-connection and airfoil-shape of modern large-size wind turbines, the location at which the root vortex leaves that blade is badly defined. When working on a realistic definition, the roll-up of the root vortex to a slightly larger radius has to be included.

1.B Root-loss model

In some current BEM codes the Prandtl factor is used for the reduction of the inflow angle to the blade root. Comparison between the 'inverse BEM' method and the vortex-wake method used for analysis of the measurements (see section 4.9) showed that these methods agree reasonably well for the tip region but differ in the root region. It follows thus that the Prandtl factor is not very accurate to describe the 'root loss' effects. Improvements can be verified with a vortex-wake model, and should only be implemented with a realistic definition of the root-vortex radius.

2. Rotor average properties for the wake state

In many BEM codes, the conditions for turbulent wake state, the equations for dynamic inflow, and the correction models for oblique inflow effects are formulated for each annulus. In particular for instationary and/or turbulent loading on the rotor it is more appropriate to use a formulation for these 'wake state' properties for the complete rotor. This would also be more realistic for a difference in blade loading in case of a failure of offset of the pitch of a single blade. Here a strong warning has to be issued that such a rotor-average wake description still has to include the effects of a vertical gradient. The latter effect gives a non-uniform wake state even without yaw misalignment.

3. Describe the rotational effects independent of the blade

At least in the programs BLADMODE and PHATAS the correction for rotational effects is applied similarly on all blades. When looking in more detail, each blade may have another effective velocity V_{eff} and thus also another speed-dependency $(\Omega\, r/V_{\text{eff}})^2$.

A next improvement in the same direction can be done by accounting for the radial flow component over the blade as result of wind direction (yaw misalignment). This is similar to what Harris has been formulating for the aerodynamics of helicopters in forward flight, [32].

4. Model for instationary blade aerodynamics

The program PHATAS has a model for dynamic stall. Modern large size wind turbines however are of the pitch-to-vane controlled type, for which edgewise vibrations are dictating the dynamic behaviour. For a realistic description of the instationary aerodynamic loads it is necessary to describe the influence of the shed-vorticity of of the vibrating airfoils, similar as by Theodorsen, Wagner, and Küssner, see e.g. Garrick [27].

7.4.2 Proposal for a 'Hybrid Vortex-Wake' model

In most wind turbine design codes (or rotor codes in general) the BEM theory is used to calculate the induced velocities in the rotor plane. Some major disadvantages of BEM models are the independence of neighbouring blade elements, the necessity to apply a 'tip loss' correction model, and the absence of the influence of the shed-vorticity on the instationary blade aerodynamics. These disadvantages can be eliminated by a vortex-wake model, which introduces a bad CPU performance resulting from the large number of degrees of freedom.

A model is described here in which the induced velocity is separated in 1) a detailed contribution from the near wake of the blade, and 2) a more global contribution from the far wake of the rotor.

Detailed influence of the near wake

Based on the observations that most of the discrepancies arise from insufficient knowledge of the aerodynamic blade loads and the omission of the interaction between neighbouring blade elements, a useful and realistic improvement of the wind turbine design codes may be based on an vortex-wake model, but with a more global wake description of the far wake in order to reduce CPU time. The description of this local blade wake is similar to a vortex wake model.

Interaction between neighbouring elements
In the conventional BEM models the induced velocities are calculated from the (instationary) momentum equations for all elements in one annulus. Based on the fact that for each element the influence of the neighbouring element is stronger than that of the elements of the other blades, it is acceptable that the aerodynamic interactions of all elements are solved for each of the blades individually. This holds even stronger if the blade elements in the same annulus have a different loading, due to vertical shear and blade-pitch error etc.

Dimension of the 'near wake'
When describing the contribution of the wake with (1) the local detailed influence of the vortex structure and (2) the global influence of the 'far wake' using a cylindrical wake model or with a single concentrated tip vortex, a choice has to be made for the transition between those parts of the wake. The vortex structure of the 'near wake' has its dominant influence in terms of the instationary aerodynamics following Theodorsen. This leads to the requirement that the dimension of this 'local wake' should extend over about 1 or 2 periods of the shed vorticity.

If the intention is that the 'near wake' also gives a realistic representation of the 'tip loss' effects and a realistic description of the wake-influence of the 'preceding' blade, then this local wake should at least extend over half a revolution.

Contribution of the far wake
If for each blade element the local influence of its own wake and of the wake of the neighbouring elements is described, the influence of the far wake has to be added. This far-wake can be described with a cylindrical-wake model, or with a simple model with a single concentrated tip and root vortex only. An example of a wake model on basis of the strength and radius of the tip vortex only was investigated by A. Häggström (thesis), [31] which was presented by B. Montgomerie (FOI) on the 16-th IEA expert meeting on the Aerodynamics of Wind Turbines.

An aerodynamic rotor model with a vortex-wake description for the near wake (in the order of half a revolution) and with a much simpler model for the far wake combines the advantages of describing the interactions between the blade elements and a relatively limited CPU time compared with a full vortex-wake model.

REFERENCES

[1] Abbott, Ira H. and Von Doenhoff, Albert E. ;
‘*Theory of Wing Sections*’.
486-60586-8, Dover publications, Inc., New York, 1959.

[2] Acker, Thomas L. (Northern Arizona univ, Flagstaff), and Hand, Maureen M. (NREL) ;
‘*Aerodynamic performance of the NREL unsteady aerodynamics experiment (phase-IV) twisted rotor*’.
Paper 99-0045, of the ASME Wind Energy Symposium, 1999.

[3] Anderson, M.B., Milborrow, D.J., and Ross, J.N. ;
‘*Performance and Wake Measurements on a 3m Diameter Horizontal-Axis Wind Turbine. Comparison of Theory, Wind Tunnel and Field Test Data*’.
Fourth International Symposium on WIND ENERGY SYSTEMS, pp. 113-136, Stockholm, Sweden, September 1982.

[4] Anderson, John D. Jr. (professor of Aerospace Engineering, Maryland);
‘*FUNDAMENTALS OF AERODYNAMICS*’. second edition
ISBN 0-07-100767-9, McGraw-Hill, Inc, Singapore 1991.

[5] Banks, W.H.H. (Bristol Univ) and Gadd, G.E. (Natl. Physical Lab. Teddington, UK);
‘*Delaying effects of rotation on laminar separation*’.
AIAA Journal Vol.1, No.4, Technical note, pp.941-942.

[6] Barnsley, M.J. and Wellicome, J.F. (Southampton University);
‘*Wind tunnel investigations of stall aerodynamics for a 10m horizontal axis rotor*’.
European Community Wind Energy Conference, Amsterdam, June 1991, pp.8-12.

[7] Bernadett, Dan W. and van Dam, Cees P. (Univ. of California at Davis 95616);
’*Comparison of predictions of airfoil characteristics for the NREL S805 and S809 airfoils*’.
Windpower ’93, San Francisco, CA, pp.290-298.

[8] Bloy, A.W. and Roberts, D.G.
(Department of Engineering (Aero.) University of Manchester England);
‘*Aerodynamic Characteristics of the NACA63$_2$-215 Aerofoil for Use in Wind Turbines*’.
In ”Wind Engineering” Vol.17, No.2, 1993, pp.67-75.

[9] Bot, E.T.G. ;
‘*AËRODYNAMISCHE TABEL GENERATOR, Handleiding*’ (In Dutch).
ECN-C--01-077, Petten, December 2001.

[10] Bramwell, A.R.S. ;
‘*Helicopter Dynamics*’.
Edward Arnold Ltd, London, 1976, ISBN 0 7131 3353 8.

[11] Butterfield, C.P., Simms, D., Musial, W.D., and Scott. G.N. (SERI, Colorado);
’*Spanwise aerodynamic loads on a wind turbine blade*’.
Windpower ’90, Washington DC 1990, pp.65-70.

[12] Cardona, José L. (16-07006 Palma de Mallorca);
’*Flow curvature and dynamic stall simulated with an aerodynamic free-vortex model for VAWT*’. Wind Engineering, Vol.8, no.3, 1984, pp.135-143

[13] Chaviaropoulos, P.K. (CRES) and Hansen, M.O.L. (Risø);
’*Investigating three-dimensional and rotational effects on wind turbine blades by means of a quasi-3D Navier-Stokes solver*’.
Journal of Fluids Engineering, Vol.22, No.2, 2000, pp.330-336.

[14] Corrigan, J.J. and Schillings, J.J. (Bell Helicopter Textron Inc, Fort Worth, Texas);
'*Empirical Model for Stall Delay due to Rotation*'.
American Helicopter Society Aeromechanics Specialists conf, San Francisco CA, Jan. 1994.

[15] Corten, G.P. (PhD dissertation, University of Utrecht);
'*Flow Separation on Wind Turbine Blades*'.
ISBN 90-393-2582-0, NUGI 837, January 2001.

[16] Coton, Frank N., Wang, T, and Galbraith, R.A. McD (univ of Glasgow);
'*An examination of key aerodynamic modeling issues raised by the NREL blind comparison*'.
AIAA-2002-0038, ASME Wind Energy Symposium, 2002, pp.168-178.

[17] Dini, Paolo (Minnesota), Coiro, Domenico P. (Napoli), and Bertolucci, Stefano (Lucca It);
'*Vortex model for airfoil stall prediction using an interactive boundary-layer method*'.
In Proc. of the 16-th ASME Wind Energy Symposium, 1995, pp.143-147.

[18] Du, Zhaohui and Selig, M.S. (Urbana, IL61080, Illinois) ;
'*A 3-D stall delay model for horizontal axis wind turbine performance prediction*'.
AIAA-98-0021, ASME, Reno, 1998, pp.9-19.

[19] Duque, Earl, C.P. van Dam, and Shannon C. Hughes (Univ of Calif, Davis);
'*Navier-Stokes simulations of the NREL combined experiment Phase-II rotor*'.
AIAA-99-0037, pp.143-153.

[20] Durand, W.F. and Lesley, E.P. (NACA) ;
'*Comparison of model propeller tests with airfoil theory*'.
Report no.196.

[21] Dwyer, H.A. (univ of Calif., Davis) and Mc Crosky, W.J. (US Army res lab, Moffett Field);
'*Crossflow and Unsteady Boundary-layer Effects on Rotating Blades*'.
AIAA paper no.70-50, pp.1-15, January 1970.

[22] Eggers, A.J. and Digumarthi, R. ;
'*Approximate Scaling of Rotational Effects of Mean Aerodynamic Moments and Power Generated by the Combined Experiment Rotor Blades Operating in Deep-Stalled Flow*'.
11-th ASME Wind Energy Symposium, Jan. 1992, pp.33-43.

[23] Eppler, Richard (Uni of Stuttgart), and Somers, Dan (Langley Research Center);
'*A Computer Program for the Design and Analysis of Low-Speed Airfoils*'.
NASA Technical Memorandum 80210.

[24] ESDU;
'*Mean fluid forces and moments on cylindrical structures:
Polygonal sections with rounded corners including elliptical shapes*'.
Engineering Sciences Data Item Number 79026, ISBN 0 85679 274 8, 1979,
Specialised Printing Services Limited, 7-9 Charlotte Street London W1P 2ES.

[25] Farell, Cesar and Fedeniuk, S.K. (Univ. of Minnesota));
'*Effect of end plates on the flow around rough cylinders*'
Journal of Wind Engineering and Industrial Aerodynamics 28, 1988, pp.219-230.

[26] Fingersh, Lee Jay and Simms, Dave and Hand, Maureen and Jager, Dave and Cotrell, Jason, and Robinson, Mike, and Schreck, Scott and Larwood, Scott (NREL);
'*Wind tunnel testing of NREL's unsteady aerodynamics experiment*'.
AIAA 2001-0035, pp.194-200.

[27] Garrick, I.E. (NASA) ;
'*On some reciprocal relations in the theory of nonstationary flows*'.
NASA report no.629.

[28] Glauert, H. ;
'*A GENERAL THEORY FOR THE AUTOGYRO*'.
ARC R - M 1111, November 1926.

[29] Sydney Goldstein, M.A. (Ph.D., St. John's College Cambridge);
'*On the vortex theory of screw propellers*'.
Communicated by L. Prandtl, for.Mem.R.S. – Received January 1929.

[30] Hageman, A. ;
'*Catalogue of Aerodynamic Characteristics of Airfoils in the Reynolds number range 10^4 - 10^6*'. R-443-D, July 1980, Wind Energy Group, University of Technology Eindhoven, The Netherlands.

[31] Häggström, Anna (Aeronautics division, FFA, SE-172 90 Stockholm);
'*Connecting thrust and torque with the wake tip vortex geometry - application to wind turbines and propellers*'.
ISSN 1650-1942, Scientific Report RFOI-R--0277--SE, December 2001.

[32] Harris, F.D. (Vertol Division, The Boeing Company, Morton, Pennsylvania);
'*Preliminary study of radial flow effects on rotor blades*'.
Journal of the American Helicopter Society, Vol.11, No.3, pp.1-21, 1966.

[33] Himmelskamp, H. (PhD dissertation, Göttingen, 1945);
'*Profile investigations on a rotating airscrew*'.
MAP Volkenrode, Reports and Translation No.832, Sept. 1947.

[34] Hoerner, S.F. ;
'*Fluid-Dynamic Drag*'. Published by the author, 1965.

[35] Hoerner, S.F. and Borst H.V. ;
'*Fluid-Dynamic Lift*'. Published by Mrs. L. Hoerner, 1985.

[36] Huyer, Stephen A. (Univ of Colorado, Boulder), Butterfield, C.P., and Simms, D. (NREL);
'*Characterisation of dynamic stall phenomena on wind turbine blades using surface pressure measurements*'.
11-th ASME Wind Energy Symposium, 1992, pp.45-46.

[37] Johansen, J., Sørensen, N.N. (Risø), Michelsen, J.A. (TU-Dk), and Schreck, S. (NREL);
'*Detached-eddy simulation on flow around the NREL Phase-IV blade*'.
23-th ASME Wind Energy Symposium, Reno, 2002, pp.106-114.

[38] Johansen, Jeppe, and Sørensen, Niels N. (Risø);
'*Method for Extracting Airfoil Data using 3D CFD Computations*'.
16-th IEA Symposium on the Aerodynamics of Wind Turbines, pp.111-123, NREL, 2003.

[39] Jonkman, Jason Mark ;
'*Modelling of the UAE wind turbine for refinement of FAST_AD*'.
Master of Science thesis, Colorado State University, Fort Collins CO, 2001.

[40] Klimas, Paul C. (Sandia, Albuquerque, NM87185);
'*Three-dimensional stall effects*'.
1-st IEA Symposium on the Aerodynamics of Wind Turbines, London, 1986, pp.80-101.

[41] Kubo, Y. (Kitakyusha, Japan), and Miyazaki, M. (Hiratsuka, Japan), and Kato, K. (Kitakyusha, Japan);
'*Effects of end plates and blockage of structural members on drag forces*'.
Journal of Wind Engineering and Industrial Aerodynamics 32, 1989, pp.392-342.

[42] Leishman, J.G. and Beddoes, T.S. (Westland helicopters Ltd, Yeovil, England);
'*A generalised model for airfoil unsteady aerodynamic behaviour and dynamic stall using the indicial method*'.
42- th annual forum of the American Helicopter Society, Washington, 1986, pp.243-265.

[43] Leishman, J. Gordon (Univ. of Maryland);
'*Challenges in modeling the unsteady aerodynamics of wind turbines*'.
AIAA 2002-0037, ASME Wind Energy Symposium, 2002, pp.141-167.

[44] Lindenburg, C. ;
'*STALL COEFFICIENTS*'. ECN-RX--01-004, Petten, January 2001.
Presented at the 12-th IEA Symposium on the Aerodynamics of Wind Turbines, 2000.

[45] Lindenburg, C. ;
'*BLADMODE, Program for Rotor Blade Mode Analysis*'.
ECN-C--02-050, Petten, July 2003.

[46] Lindenburg, C. ;
'*STATUS OF PHATAS Release "OCT-2002", Unix and Windows version*'.
ECN-I--03-001, Petten, July 2003.

[47] Lindenburg, C. ;
'*PHATAS-IV Release "OCT-2002", User's Manual*'.
ECN-I--03-006, Petten, July 2003.

[48] Madsen, Helge Agaard, and Rasmussen, Flemming (Risø);
'*Derivation of three-dimensional airfoil data on the basis of experiment and theory*'.
Proceedings Windpower '88, Honolulu Hawaii, pp.166-174.
2-nd IEA Symposium on the Aerodynamics of Wind Turbines, Lyngby 1988.

[49] Madsen, Helge Agaard, and Christensen, H.F. (Risø National Laboratories, Riskilde, DK) ;
'*On the relative importance of rotational, unsteady and three-dimensional effects on the HAWT rotor aerodynamics*'.
EWEC conference, Madrid, 1990, pp.227-232.

[50] Mandal, Dr. A.C. (Univ of Bangladesh) and Burton, Dr. J.D. (Univ of reading, UK);
'*The effects of dynamic stall and flow curvature on the aerodynamics of Darrieus turbines applying the Cascade model*'.
Wind Engineering, Vol.18, No.6, 1994, pp.267-282.

[51] Massini*, G., Rossi*, E., D'Angelo**, S.
(*ENEA Rome, **Polytechnic University - Torin);
'*Wind tunnel measurements of aerodynamic coefficients of asymmetrical airfoil sections for wind turbine blades extended to high angles of attack*'.
EC DG-XII Contract number: EN3W - 0018 - I, Conclusive Rapport.
ENEA - Comitato Nazionale per la Ricerca e per lo Sviluppo dell'Energia Nucleare e delle Energie Alternative Viale Regina Margherita, 125 - 00198 Roma.

[52] Michos, A. Bergeles, G., and Athanassiadis, N. (Nat.Techn.Univ.Athens);
'*Aerodynamic Characteristics of NACA0012 Airfoil in Relation to Wind Generators*'.
In *Wind Engineering*, pp.247-261, Vol.7, No.4, 1983.

[53] Miley, S.J. ;
‘*A Catalog of Low Reynolds Number Airfoil Data for Wind Turbine Applications*’.
RFP-3387 UC-60, Department of Aerospace Engineering, Texas A&M University, College Station Texas 77843, February 1982.

[54] Milborrow, D.J. (Central Electricity Generating Board, London);
’*Changes in aerofoil characteristics due to radial flow on rotating blades.*’.
Proceedings of the 7-th BWEA conference, 1985, Edited by A. Garrad.

[55] Milne-Thomson, L.M. ;
’*THEORETICAL AERODYNAMICS*’.
ISBN 0-486-61980-X, Dover Publications Inc, New York, 1958.

[56] Montgomerie, B. ;
’*Drag coefficient distribution on a wing at 90 degrees to the wind*’.
ECN-C--95-061, Petten, February 1996.

[57] Ostowari, C. (Assistant Professor) and Naik, D. (Graduate Research Assistant) ;
‘*Post stall studies of Untwisted Varying Aspect Ratio Blades with an NACA 4415 Airfoil Section - Part I*’.
In ”Wind Engineering” Vol.8, No.3, 1984, pp.176-194.

[58] Ostowari, C. (Assistant Professor) and Naik, D. (Graduate Research Assistant) ;
‘*Post stall studies of Untwisted Varying Aspect Ratio Blades with NACA 44xx Series Airfoil Sections - Part II*’.
In ”Wind Engineering” Vol.9, No.3, 1985, pp.149-164.

[59] Petersen, H. (The Test Station for Windmills, Risø National Laboratory, Denmark);
‘*Benchmark Test on Power Curve Computations on Wind Turbines - A Compendium*’.
Part 1, *Power Curve Computations* (Incomplete Draft, Nov. 86).
Report of C.E.C. contract no. XVII/84/B/7033/11/004/17.

[60] Riberio, José Luis Duarte (Porto Alegre, RS, Brasil);
‘*Fluctuating lift and its spanwise correlation on a circular cylinder in a smooth and in a turbulent flow: a critical review*’.
Wind Engineering and Industrial Aerodynamics, 40, 1992, pp.179-198.

[61] Ronsten, Göran (FFA);
’*Static Pressure Measurements on a Rotating and Non-rotating 2.375m Wind Turbine Blade – Comparison with 2D Calculations*’.
European Community Wind Energy Conference, Amsterdam, June 1991, pp.214-220.

[62] Satran, D. and Snyder, M.H. ;
‘*Two-dimensional tests of GA(W)-1 and GA(W)-2 airfoils at angles-of-attack from 0 to 360 degrees*’.
Wind Energy Report No.1, January 1977. Wind Energy Laboratory, Wichita State University, Wichita, Kansas.

[63] Schreck, S., and Robinson, M. (NREL);
’*Rotational augmentation of horizontal axis wind turbine blade aerodynamic response*’.
AIAA-2002-0029, 23-th ASME Wind Energy Symposium, 2002, pp.70-82.

[64] Schreck, S., and Robinson, M. (NREL);
’*Structures and interactions underlying rotational augmentation of blade aerodynamic response*’.
AIAA 2003-0520, 24-th ASME Wind Energy Symposium, pp.70-82.

[65] Scott, G.N., Butterfield, C.P., Simms, D.A., and Musial, W.D. (NREL);
'*Correlation of flow visualisation and pressure distribution data on a wind turbine blade*'.
contribution to the 11-th ASME Wind Energy Symposium, 1991, pp.115-118.

[66] Sharpe, D. (Kingston Polytechnic);
Measured coefficients for the NACA0012 airfoil.

[67] Sheldahl, Robert E. and Blackwell, Ben F. ;
'*Aerodynamic Characteristics of Four Symmetrical Airfoil Sections through 180 Degrees Angle of Attack at Low Reynolds Numbers (Preliminary Data Report)*'.
VAWT workshop, N.M. 87115, pp. II-73 - II-106, Sandia Laboratories, Albuquerque, 1976.

[68] Shen, W.Z., Mikkelsen, R., and Sørensen, J.N. (TU-Dk), and Bak, C. (Risø) ;
'*Evaluation of tip correction theories*'.
15-th IEA Symposium on the Aerodynamics of Wind Turbines, Athens 2001.

[69] Simms, Dave (NREL);
'*Overview and Status of the NREL Unsteady Aerodynamics Experiment*'.
11-th IEA Symposium on the Aerodynamics of Wind Turbines, ECN Petten, 1997.

[70] Simms, D., Schreck, S., Hand, M., Fingersh, L.J., Cotrell, J., Pierce, K., and Robinson, M.;
'*Plans for Testing the NREL Unsteady Aerodynamics Experiment 10-m Diameter HAWT in the NASA Ames Wind Tunnel*'.
NREL/TP-500-27599, National Renewable Energy Laboratory, Golden CO, October 1999.

[71] Snel, H. (ECN), Houwink, R. (NLR), and Bosschers, J. (NLR) ;
'*SECTIONAL PREDICTION OF LIFT COEFFICIENTS ON ROTATING WIND TURBINE BLADES IN STALL*'.
ECN-C--93-052, Petten, December 1994.

[72] Snel, H. and Schepers, J.G. ;
'*Joint Investigation of Dynamic Inflow Effects and Implementation of an Engineering Method*'. ECN-C--94-107, Petten, April 1995.

[73] Somers, D.M. (NREL);
'*Design and Experimental Results for the S809 Airfoil*'.
NREL/SR-440-6918, Golden CO, Jan. 1997.

[74] Sørensen, Jens Nørkaer ;
'*A new computational model for predicting 3-D stall on a HAT*'.
1-st IEA Symposium on the Aerodynamics of Wind Turbines, London 1986.

[75] Sørensen, N.N. (Risø), Michelsen, J.A. (TU-Dk), and Schreck, S. (NREL);
'*Navier-Stokes predictions of the NREL Phase-IV rotor in the NASA Ames 80-by-120 wind tunnel*'. AIAA-2002-0031, ASME Wind Energy Symposium, 2002, pp.94-105.

[76] Strickland, J.H.
(Assistant Professor, Mechanical Engineering, Texas Tech University, Lubbock, Texas);
'*AERODYNAMICS OF THE DARRIEUS TURBINE*'.
In "Vertical-axis Wind Turbine Technology Workshop", SAND76-5586,
Sandia Laboratories, Albuquerque, New Mexico 87115.

[77] Tangler, J.L. (NREL) and Selig, Michael S. (Univ. of Illinois, Urbana);
'*An evaluation of an empirical model for stall delay due to rotation for HAWTs*'.
In Proceedings Windpower '97, Austin TX, pp.87-96.

[78] Tangler, J.L. (NREL);
'*Insight into a Wind Turbine Stall and Post-Stall Aerodynamics*'.
In Proceedings Windpower '03, Austin TX.

[79] Templin, R.J. and Wickens, R.H. ;
'*Aerodynamic characteristics of the NACA0018 airfoil at high Reynolds numbers and at angles of attack from 0° to 180°*'.
TM-WE-020, National Research Council Canada, July 1984.

[80] Timmer, W.A. ;
'*Measured coefficients for the S809 airfoil at Re=1M*'.
IVW, Technical University of Delft.

[81] Timmer, W.A. (Technical University of Delft);
E-mail correspondence including S809 airfoil coefficients, received on November 6, 2003.

[82] Timmer, W.A. and Rooij, R.P.J.O.M. van (DUWIND, Wind Energy Research Institute);
'*De profielgegevens voor de Aërodynamische Tabel Generator, ATG*' (Dutch).
WE-011079, Delft University of Technology, Fac. of Civil Engineering, November 2001.

[83] Viterna, Larry A. and Janetzke, David C. (NASA Lewis Research Center);
'*Theoretical and experimental power from large horizontal-axis wind turbines*'.
SERI/CP-635-1340, Vol.II pp.265-280, Fifth Biennal Wind Energy Conference and Workshop, Washington DC, 1981.

[84] Vries, O. de (NLR);
'*Fluid dynamic Aspects of Wind Energy Conversion*'.
AGARDograph No. 243, AGARD, 1978.

[85] Whale, J., Fisichella, C.J., and Selig, M.S. (Univ. of Illinois, Urbana, IL 61801) ;
'*Correcting inflow measurements from HAWTs using lifting-surface code*'.
In AIAA Journal, AIAA-99-0040, pp.175-185.

[86] Wolfe, Walter, P. (SANDIA) and Ochs, Stuart S. (Iowa State Univ, Ames, IA) ;
'*CFD Calculations of S809 Aerodynamic Characteristics*'.
In AIAA Journal, AIAA-97-0973, pp.341-348.

[87] Xu, Guanpeng and Sankar, Lakshmi N. (Georgia Institute of Technology, Atlanta, GA);
'*Application of a viscous flow methodology to the NREL phase-IV rotor*'.
ASME Wind Energy Symposium, Reno 2002, AIAA-2002-0030, pp.83-93.

[88] Yang, S.L., Chang, Y.L., and Arici, O. (Michigan T.U., Houghton, MI) ;
'*Post-stall Navier-Stokes computations of the NREL airfoil using $k-\omega$ turbulence model*'.
In Proc. of the 16-th ASME Wind Energy Symposium, 1995, pp.127-136.

[89] Zhang, Shijie and Yuan, Xin, and Ye Dajun (Tsinghua University, Beijing China);
'*Analysis of turbulent separated flows for the NREL airfoil using anisotropic two-equation models at higher angles of attack*'.
Wind Engineering Vol.25, No.1, pp.41-53.

APPENDIX A. MODELLING OF THE UAE PHASE-VI TURBINE

A.1 Introduction

The following descriptions are partly from Fingersh et al. [26].

NASA-Ames wind tunnel
The National Full-Scale Aerodynamic Complex (NFAC) of NASA started in 1944 with a closed-loop wind tunnel, having a 12.2m x 24.4m test section. In 1987 an open-loop test section was added to this complex. This extension has a 24.4m x 36.6m cross section that required an upgrade of the tunnel fan power. The upgraded system has 6 turbofans with 15 blades, each driven by an electric motor of 16800kW. Both the speed and the pitch of the fans can be controlled which allows tunnel wind velocities in the test section up to 50 m/s.

The measurements in the UAE phase-VI turbine in the spring of 2000 dealt with more than 1700 different turbine configurations. These measurements yielded more that 2200 data sets the amount up to 100Gb f data. By measuring the tunnel free-stream velocity with and without the UAE phase-VI turbine, an estimate can be made of the wake blockage. This method showed that the wake blockage was no more than 3% and often much less.

Unsteady Aerodynamic Experiment program
Between 1988 and 1999 the Department of Energy's (DOE) National Renewable Energy Laboratory (NREL, formerly SERI) operated a research wind turbine at the National Wind Technology Center (NWTC) in Golden, Colorado. This heavily instrumented turbine was based on the Grumman Wind Stream 33 and has a 19.8kW asynchronous generator with a 72rpm rotor speed. This turbine was called Unsteady Aerodynamics Experiment (formerly the Combined Experiment) and was meant to investigate the aerodynamic performance of wind turbines, for which the hub can be configured with fixed blade connection (while allowing different cone angles), blade flapping hinges or a teeter hinge.

Since 1988 the following measurement phases were performed, each with a different configuration:

	Phase-II	Phase-III	Phase-IVa, IVb	Phase-V	Phase-VI
Period	May - July '90	March '96	April - May '96	Spring '98	Spring 2000
Blades	3 untwisted	3 twisted	3 twisted	2 twisted	2 twist + taper
10-min data sets	29	20	92	92	
Data collected	290min	230min	950 + 750min	730min	260min
Press. tap sections	4	5	5	5	5
LFA sensors	4 flags	4 flags	5 probes	5 probes	5 probes
Pitch angles	8, 12	3	-3, +3, +8	-9, -3, 3, 8, 12	various

The 3-bladed untwisted Phase-I rotor was used for system validation.

The sectional loads obtained from measurements on the Phase-II rotor were reported by Butterfield et al. [11]. Later flow visualisations of the Phase-II rotor were presented by Scott et al. [65]. More extensive investigations of the blade aerodynamics in stall for stationary conditions at different wind speed and yaw angles were reported by S. Huyer, D. Simms, amd M. Robinson citeHUYER92. Duque, Van Dam, & Shannon performed Navier-Stokes analyses of the complete Phase-II turbine [19]. Eggers and Digumarthi [22] used the power and blade root flapping moment measured on the Phase-II rotor for scaling of the models for rotational effects.

The rotor performance and the normal-force coefficients of the measurements on the twisted Phase-IV rotor were presented by Acker and Hand [2].

Following is the model description of the 10m diameter UAE phase-VI turbine as used for calculations with PHATAS [47] and with BLADMODE [45]. This input file is mainly based on the documents from the web-site `http://wind.nrel.gov/amestest` .
Initially this file was composed for the Blind Comparison calculations in the fall of 2002. In the winter of 2002 this modelling was refined using the data obtained at NREL.

A description of the phase-VI rotor was also included in the MSc thesis of J.M. Jonkman [39].

A.2 Aerodynamic Modelling

A.2.1 Blade geometry

The blade is modelled from the rotor centre to the blade tip, which has a radius of 5.029m.
The specified chord distribution appears to be linear over a large part of the span.
This linear distribution is defined with a chord of 0.7366m (= 29in) at r = 1.2573m (= 49.5in) to a chord of 0.3808m = (14.992in) at r = 4.7797m (= 188.179in).

The blade axis runs through the 30% chord locations which means that the 25% chord location (aerodynamic centre) is 5% in front of the leading edge, which has a negative sign in the BLADMODE and PHATAS input.

The blade can have 2 different tips, with which the radii are 5.029m and 5.532m. The measurements in the NASA-Ames wind tunnel were performed with the shorter blade tips. These replaceable tips have a rounded chord distribution at the leading edge, of which the radius was measured from the 'smoke-tip' as 0.086m (by C. Lindenburg, Febr. 2002). Compared with a straight tapered planform towards the tip, the rounded planform gives a 0.0016m^2 reduction in blade area. This reduction in blade area was modelled in PHATAS by cutting the chord linearly from r = 4.945m to a chord of 0.3175m at the tip (instead of the linearised 0.3556m). For the straight trailing edge the aerodynamic centreline is correspondingly 0.0108m aft of the blade axis.

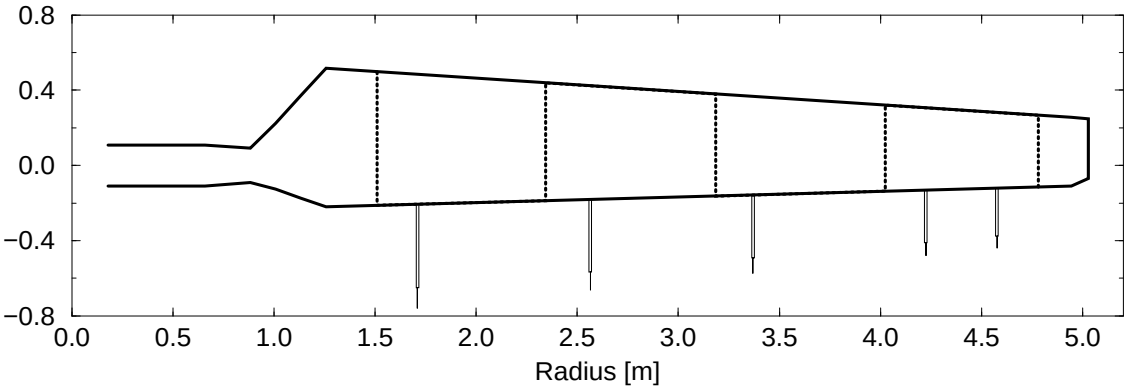

Figure A.1 *Modelled geometry of the UAE phase-VI rotor blade*

The dotted lines in Figure A.1 indicate the instrumented sections at 1.510m, 2.343m, 3.185m, 4.032m, and 4.780m. Figure A.1 also shows the pitot-tubes at 34%, 51%, 67%, 84%, and 91% radius.

A.2.2 Twist distribution

The twist distribution in the description from the web-site has a value of -1.775deg at r = 5m and 21.8deg at the largest chord r = 1.2753m. In the measurement campaigns the blade pitch angle was given as the orientation of the r = 5m location. To use the same twist in the calculations as in the measurements the twist distribution as listed was increased with 1.775deg.

Some values of the twist distribution were skipped, which leaves an input table with 22 records.

A.2.3 Airfoil distribution

The rotor blades of the UAE have the 20.95% thick S809 airfoils, from r = 1.2573m (= 49.5in) to the tip. The blade root is circular up to a radius r = 0.883m, where a linear transition starts towards the S809 shape at r = 1.2573m. For the analysis with PHATAS and with BLADMODE the blade root was modelled with the drag coefficient of a cylinder, for which 1.0 was chosen. Depending on the roughness and turbulence this drag can be between 0.35 (rough) and 1.2 (smooth).

Since the characteristics of the transition area between r = 0.883m and r = 1.2573m may deviate well from the S809 airfoil one may consider to model the radius of the root vortex closer to the start of the S809 shape. Still it was decided for simplicity to model half of this transition area with the drag of a cylinder and half with the coefficients of the S809 airfoil. This means that the for the analyses with the tool *inflow*, see appendix B, the radius of the root vortex is 1.07m. On basis of this choice the S809 airfoil coefficients were assigned to locations with a radius larger than r = 1.07m. In the models of PHATAS and of BLADMODE this radius is also used as the location of the 'root vortex'.

Reynolds number distribution

For the instrumented locations, the Reynolds numbers were calculated for a rotor speed of 72rpm and for some wind speed values. These calculations were done for the local chord and for a viscosity of $1.5{\cdot}10^{-5}$. In this calculation the contribution of the induced velocities in the rotor plane were omitted, which are already small.

Location	rel.	Chord	(c/r)	10m/s	15m/s	20m/s
1.510m	30.0%	0.711m	0.4709	$0.72{\cdot}10^6$	$0.89{\cdot}10^6$	$1.09{\cdot}10^6$
2.343m	46.6%	0.627m	0.2676	$0.85{\cdot}10^6$	$0.97{\cdot}10^6$	$1.12{\cdot}10^6$
3.185m	63.3%	0.542m	0.1701	$0.94{\cdot}10^6$	$1.02{\cdot}10^6$	$1.13{\cdot}10^6$
4.023m	80.0%	0.457m	0.1137	$0.97{\cdot}10^6$	$1.03{\cdot}10^6$	$1.11{\cdot}10^6$
4.780m	95.0%	0.381m	0.0797	$0.95{\cdot}10^6$	$0.99{\cdot}10^6$	$1.05{\cdot}10^6$

The c/r values listed here are calculated with the linearised relation for the chord. Knowing that most of the measurements were performed for a wind velocity near 15m/s, it follows that aerodynamic coefficients for a Reynolds number of $1{\cdot}10^6$ are acceptable. This table also contains the (c/r) ratios that can be used in models for rotational augmentation.

All aerodynamic coefficients files for the S809 airfoil that were available at the web-site were copied and investigated. Later comparisons were made with the aerodynamic coefficients calculated by Dan Bernadett & C.P. van Dam [7], see chapter 3. The aerodynamic coefficients that were finally used for the calculations were the measurements by Somers in the TU-Delft wind tunnel for a Reynolds number of $1{\cdot}10^6$. For the larger angles of attack, the data from the Ohio State University were added with an angle-of-attack shift of -0.53deg. Finally the coefficients for deep stall were added using the empirical tool *StC* (chapter 2) for an aspect ratio of 7. The assessment of the S809 airfoil characteristics is also described in section 3.4.

The following table contains the most significant part of the aerodynamic coefficients of the S809 airfoil that are used to analyse the NASA-Ames campaigns with BLADMODE and PHATAS.

```
−45.0  −0.7592  0.7757  0.1818
−40.0  −0.7847  0.6776  0.1644
−35.0  −0.7903  0.5739  0.1462
−32.0  −0.7827  0.5100  0.1348
−30.0  −0.7726  0.4670  0.1271
−28.0  −0.7584  0.4241  0.1192
−26.0  −0.7414  0.3813  0.1111
−25.0  −0.7376  0.3597  0.1065
−24.0  −0.7378  0.3379  0.1016
−22.0  −0.7478  0.2943  0.0906
−20.0  −0.7661  0.2510  0.0785
−18.0  −0.7873  0.2087  0.0657
−16.730 −0.80000 0.182600  0.05743
−14.630 −0.79000 0.079300  0.04428
−12.630 −0.70000 0.054700  0.03176
−10.730 −0.63000 0.040100  0.01986
 −8.730 −0.58000 0.026600  0.00734
 −6.730 −0.61000 0.019300 −0.00518
 −4.630 −0.40000 0.012700 −0.01832
−2.630 −0.16000 0.009000 −0.03085
−1.040  0.01510 0.008530 −0.04080
−0.010  0.13400 0.008450 −0.04350
 1.020  0.25330 0.008540 −0.04620
 2.050  0.37240 0.008680 −0.04870
 3.070  0.49130 0.008630 −0.05140
 4.100  0.61010 0.008710 −0.05380
 5.130  0.72930 0.008980 −0.05600
 5.640  0.78700 0.009100 −0.05654
 6.160  0.84240 0.009170 −0.05710
 6.410  0.86810 0.009260 −0.05551
 6.670  0.88250 0.010190 −0.05385
 6.920  0.89210 0.011420 −0.05226
 7.180  0.90250 0.012560 −0.05060
 8.200  0.94410 0.016840 −0.04390
 9.210  0.97280 0.021455 −0.03740
 9.570  0.96524 0.023100 −0.03824
10.200  0.95200 0.026307 −0.03970
10.670  0.94972 0.028700 −0.03728
11.210  0.94710 0.033074 −0.03450
11.670  0.97393 0.036800 −0.03788
12.230  1.00660 0.046116 −0.04200
12.770  1.02007 0.055100 −0.04200
13.220  1.03130 0.061600 −0.04200
13.670  1.04168 0.068100 −0.04196
14.230  1.05460 0.069444 −0.04190
14.670  1.05782 0.070500 −0.04186
15.230  1.0615  0.080300 −0.04180
15.670  1.05301 0.088000 −0.04331
16.220  1.04300 0.096965 −0.04520
16.670  1.01361 0.104300 −0.04547
17.200  0.97900 0.120907 −0.04579
17.570  0.90000 0.132500 −0.04896
18.190  0.83236 0.197262 −0.05440
18.670  0.78000 0.247400 −0.05993
 20.0   0.7736  0.2695 −0.0756
 22.0   0.7622  0.3042 −0.0982
 24.0   0.7520  0.3406 −0.1187
 25.0   0.7486  0.3596 −0.1279
 26.0   0.7470  0.3791 −0.1362
 28.0   0.7512  0.4197 −0.1496
 30.0   0.7643  0.4621 −0.1589
 32.0   0.7743  0.5045 −0.1677
 35.0   0.7818  0.5678 −0.1805
 40.0   0.7764  0.6704 −0.2007
 45.0   0.7511  0.7675 −0.2197
 50.0   0.7089  0.8573 −0.2375
 55.0   0.6524  0.9383 −0.2541
 60.0   0.5840  1.0097 −0.2698
 70.0   0.4201  1.1214 −0.2982
 80.0   0.2326  1.1895 −0.3233
 90.0   0.0341  1.2136 −0.3454
```

A.2.4 Element distribution

In the program PHATAS the aerodynamics and also the structural dynamics of the blade are described for a number of elements of equal size. For the 'Blind Comparison' the aerodynamic sectional loads had to be given for the five instrumented sections, which are at the relative radii: 30.0%, 46.6%, 63.3%, 80.0%, and 95.0%. For the calculations performed in the fall of 2000 the blade was modelled with 17 blade elements, starting from a 'root radius' of 0.2m. With this discretisation the spanwise discrepancy between the middle of the elements and the instrumented sections was 0.031m for the 30.0% section, 0.0385m for the 95.0% section, and not larger than 0.014m for the other sections. In the model of PHATAS the aerodynamics of the 'outer element' are calculated after this element is split into 2 elements of half the size. This is done for a more detailed description of the reduction of the blade loads towards the tip. The 95.0% location corresponds with the centre of the inner half of the 'split element'.

For later work the blade was also modelled with 17 elements, but starting from a 'root radius' of 0.19m. With this element distribution the spanwise discrepancy was 0.038m for the 30.0% and the 95.0% section, 0.019m for the 46.6% location, and not larger than 0.01m for the other locations. The error for the 30.0% and 95.0% section was accepted because these locations also have some radial flow due to the end-effects for which reason modelling on basis of BEM theory is already inaccurate. For the 30.0% section the accuracy of the measurements is even worse because of the low dynamic pressure, the vicinity of the root vortex, the disturbances from the boxes mounted to the hub, the stall characteristics which are rather severe for this small radius, etcetera.

A.3 Structural Modelling

A.3.1 Rotor model

The structural properties of the rotor blades were copied to a large extent from a description on basis of which the blade was built. Table A.9 of this description contains the spanwise distribution of the mass, mass centreline, cross-sectional inertias, and the bending and torsional stiffnesses.

With this mass distribution the total rotor inertia (without hub inertia) is 786kgm^2, which is not far from to the inertia given in the description on the web-site: 949kgm^2. The remaining difference of 163kgm^2 was modelled as hub inertia.

A detailed description of the phase-VI rotor was not available for which reason the modelling was based on the non-tapered phase-V rotor. In chapter 6 of his thesis [39] J.M. Jonkman made an attempt to approach a realistic blade mass and stiffness distribution. For the investigations reported here the blade properties were used without modification.

The locations of the mass centreline listed in table A.9 are negative. It was assumed that a negative location is towards the trailing edge.

The distribution of the bending and torsional stiffnesses in table A.9 of the blade specification, shows a large variation up to r = 1m, which means that the blade frequencies depend strongly on the detailed stiffness distribution. Figure 4 of the PDF file from the web-site gives the diameter of the pitch shaft as 0.079m. The bending stiffness of this pitch shaft is 0.4MNm^2, which is slightly less than the specified 0.416MNm^2 in table A.9. When measured from the centre of the outer bearing in Figure A.4 of the PDF file from the web-site, the free length of the 0.079m diameter shaft is 0.111m. The distance between the centre of the pitch bearings is 0.189m. The bending stiffness of a shaft supported by two bearings can be approximated with an elongation of the shaft with 1/3 of the distance between the bearings, which gives an effective shaft length of 0.111m + 0.063m = 0.174m. This shaft length is modelled from r = 0.281m until r = 0.455m, after which the stiffness is increased to the high value of 10.0MNm^2.

Because the gear of the pitch mechanism is attached to the blade at r = 0.46m, the 0.079m diameter blade shaft does not carry the torsional moment so its torsional flexibility is not modelled as blade torsional stiffness. The models prepared for the analyses with PHATAS and with BLADMODE have a very large torsional stiffness. In reality the flexibility of the pitch servo has to be added. The spanwise distribution of the blade bending stiffness is plotted in Figure A.2 From Figure A.2

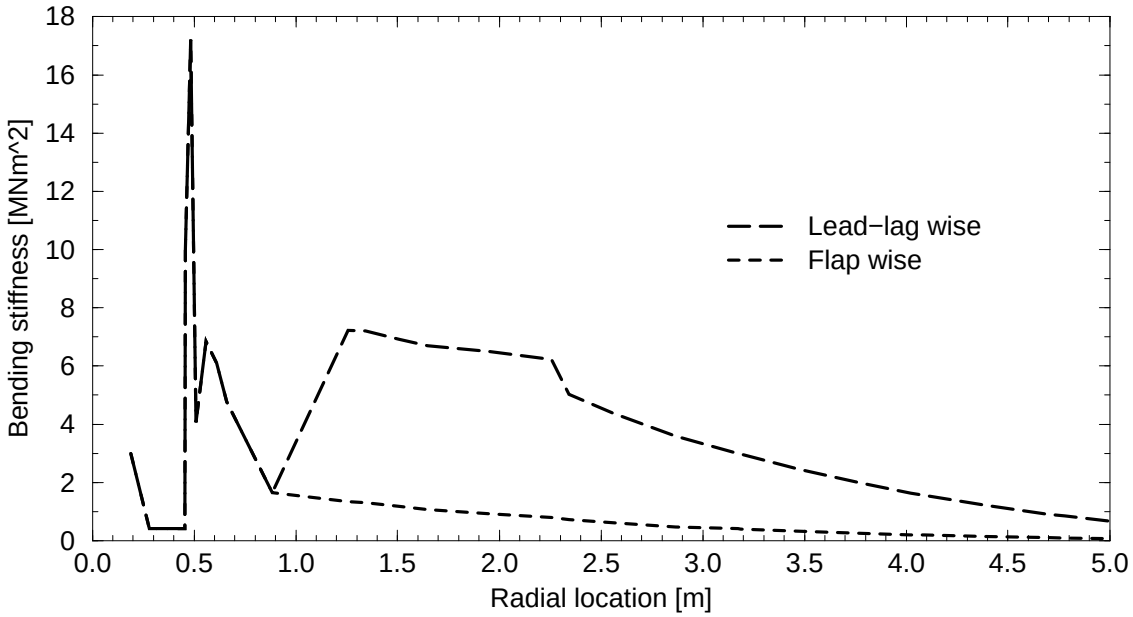

Figure A.2 *Blade bending stiffness distribution*

it follows that the bending stiffness has very strong variations near the blade root. The small bending stiffness near r = 0.4m is for the strain-gauge location.

With the resulting stiffness distribution the flapwise and edgewise bending frequencies were calculated with PHATAS as 8.12Hz and 10.28Hz (non-rotating) and with BLADMODE as 8.17Hz and 10.37Hz. These frequencies are higher than those mentioned in the documentation on the website: 7.31Hz and 9.06Hz. These over-estimations are most likely caused by the flexibility in the hub construction which is not modelled.

Investigations with PHATAS into the influence of the number of blade elements show well-defined bending frequencies for 10 blade elements or more while for a 'stable' blade torsional frequency of the UAE phase-VI rotor one needs at least 15 blade elements, see Figure A.3.

The Lock number for the first flapping mode is 0.985 calculated with PHATAS and 0.96 calculated with BLADMODE, which is small for a rotor blade. A small Lock number indicates little aerodynamic damping for structural dynamics, here blade flapping. As long as the blade loads are measured directly from the aerodynamic pressure distribution this has little effect on the aerodynamic analyses.

A.3.2 Turbine model

Nacelle

The nacelle mass is 1332kg which is the specified value of 1712kg minus 379.7kg hub mass.
The nacelle yawing inertia has the specified value of 3798kg*m^2.
The hub mass was increased to 412.8kg such that the total rotor mass of 576.3kg is matched.

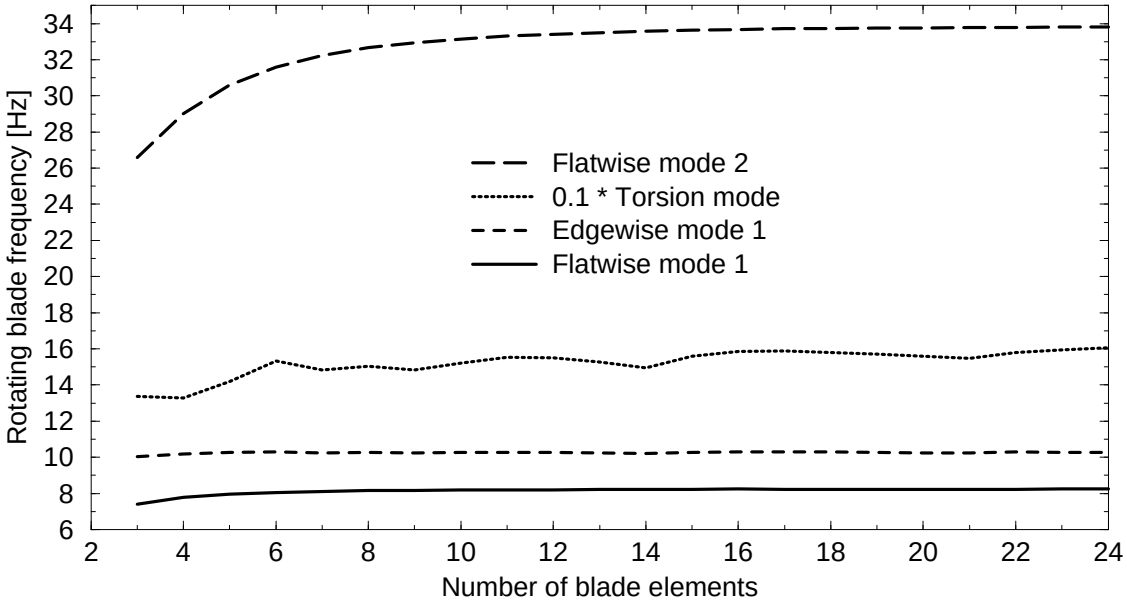

Figure A.3 *Blade bending frequencies for different no. of elements*

Generator

The generator is described as an asynchronous generator with a nominal rotor speed of 72.838rpm and a nominal power of 19.8kW, which gives a nominal torque of 2.5958kNm. With the nominal slip of 1.69% the slope of the torque-speed relation follows as 20.14kNm/(rad/s).

The time constant τ = 0.025s for the generator torque is used as:

$$Q_{\mathrm{gen}} + \tau\, \partial Q_{\mathrm{gen}}/\partial t = Q_{\mathrm{gen(stationary)}} \,.$$

In PHATAS the rotational direction is opposite to that of the UAE rotor. This is compensated by changing the sign of the yaw angles and also of some of the output properties where needed.

Losses

The drive train efficiency was reported as 78%. Calculation of the expression for full-load operation gives an efficiency of 81.32%. With the specified relation for the efficiency, the loss of power was calculated at full load and at 50% partial load. From these values the linear expression for the loss of torque was derived. The drive train lossed were modelled with 16% of the shaft torque plus a constant part of 163.7Nm. This linearised approximation was fitted to the loss between a power of 8kW and 12kW.

Transmission

The transmission ratio is 25.13. The generator inertia 143kgm^2/(25.13)^2 = 0.22644kgm^2 was modelled at the fast shaft. The shaft torsional stiffness k_{sh} was given as the value of the lumped drive train flexibility of 199kNm/rad. The total drive train inertia should be between 144 and 179kgm^2. With 143kgm^2 for the generator, the slow shaft inertia was chosen at 17kgm^2.
For a disconnected generator the frequency is 6.07Hz while for normal operation the drive train inertia is 2.277Hz.

The shaft was modelled with the given lumped stiffness of all flexible elements; 199kNm/rad.

The specified drive train frequency is 5.78Hz while the drive train frequency calculated with BLADMODE for an idling generator is 5.94Hz.

A.3.3 Tower model

The 11.5m long tower was described with tubular sections in terms of diameter and wall thickness while the material properties are those for steel. The material density of the steel tower was increased to 9000kg/m^3.
In the documentation the wall thickness of the upper-part has a typing error. Following the 'Frequently Asked Questions' web-page the wall-thickness of the lower part is 0.0175m and of the upper part is 0.0214m. The conical section in between has a wall thickness of 0.0214m.

For this tower the total mass was calculated as 2917kg while the specified value is 3317kg.
The difference may be from the flanges at the root, and the lifting eyes at the top etcetera.

The model for tower dynamics in PHATAS is based on a modal description following the method of R.R. Craig Jr (univ. of Texas) and M.C.C. Bampton (the Boeing company). For the tower of the UAE turbine, this model has 3 internal elastic modes. The first fore-aft bending frequency (assuming a rigid rotor) was calculated as 1.71Hz, which differs not much from the 1.695Hz in the documentation on the web-site.

The drag coefficient of the tower (used for the strength of the tower wake) is 0.35, based on a Reynolds number between $0.4 \cdot 10^6$ and $0.7 \cdot 10^6$. For the load cases with 7m/s wind speed the Reynolds number is $0.28 \cdot 10^6$ in which case the tower drag coefficient was estimated at 1.0.

A.4 Stationary Aerodynamic Rotor Properties

In the Blind Comparison held in the fall of 2000, see also chapter 6, it appeared that the results calculated with most BEM-based codes show serious differences, even for the low wind-speed values where the blades are not in stall. At the Blind Comparison it was already suggested that part of the differences may be caused by the choice of the aerodynamic coefficients, which was also shown by Figure 6.5 in section 6.3.

A.4.1 Idealised aerodynamic properties for the UAE phase-VI rotor

As one of the first tasks within the ongoing IEA Annex-XX framework project, it was discussed to investigate the reasons for the difference in the Blind Comparison on basis of the calculated aerodynamic rotor properties for simplified/idealised conditions. These simplified conditions imply among others that all structural dynamics are excluded and that the same table of airfoil coefficients are used.

As onset for comparison by other IEA Annex-XX partners, the aerodynamic rotor characteristics were calculated with PHATAS for the 3.0deg blade pitch angle as was also used for the Blind Comparison. The simplifications/idealisations for these calculations are:

- The rotor blades and turbine were modelled rigid;
- The rotor speed was constant at 72.0rpm;
- The aerodynamic tower influence was excluded;
- The air density was constant, 1.23kg/m^3;
- TU-Delft based airfoil coefficients with deep-stall data from *StC* (see section A.3);
- No corrections for rotational effects or reduction near the tip was applied;
- The blade root has no aerodynamic loads (the S809 airfoil data start at r = 1.044m);
- No correction for 'root loss': Calculations were done without and with tip-loss.

The calculations with tip-loss were performed with the factor of Prandtl.

The results of these calculations are:

	Without tip- and root- loss factor				With Prandtl factor for tip-loss			
Wind speed [m/s]	Power coeff	Thrust coeff	Shaft torque [kNm]	Root moment [kNm]	Power coeff	Thrust coeff	Shaft torque [kNm]	Root moment [kNm]
5.0	0.4143	0.5896	0.337	1.085	0.3655	0.5487	0.297	0.989
6.0	0.4330	0.5833	0.607	1.540	0.3795	0.5408	0.532	1.398
7.0	0.4157	0.5438	0.925	1.971	0.3643	0.5068	0.811	1.796
8.0	0.3532	0.4588	1.173	2.196	0.3180	0.4391	1.056	2.068
9.0	0.2910	0.3871	1.376	2.334	0.2668	0.3771	1.261	2.252
10.0	0.2207	0.3196	1.431	2.394	0.2172	0.3199	1.409	2.373
11.0	0.1654	0.2729	1.428	2.495	0.1600	0.2694	1.381	2.441
12.0	0.1213	0.2329	1.359	2.527	0.1186	0.2314	1.329	2.498
13.0	0.0839	0.1994	1.195	2.502	0.0874	0.2005	1.245	2.519
14.0	0.0528	0.1725	0.940	2.443	0.0614	0.1763	1.092	2.530
15.0	0.0298	0.1532	0.652	2.416	0.0428	0.1577	0.938	2.545
16.0	0.0227	0.1419	0.604	2.512	0.0299	0.1435	0.794	2.580
17.0	0.0193	0.1333	0.614	2.635	0.0228	0.1334	0.726	2.664
18.0	0.0166	0.1262	0.630	2.772	0.0174	0.1249	0.657	2.750
19.0	0.0147	0.1204	0.652	2.924	0.0149	0.1190	0.665	2.892
20.0	0.0132	0.1156	0.684	3.089	0.0133	0.1141	0.692	3.051
21.0	0.0121	0.1116	0.724	3.269	0.0121	0.1100	0.727	3.223
22.0	0.0112	0.1081	0.772	3.459	0.0111	0.1065	0.770	3.406
23.0	0.0105	0.1050	0.826	3.660	0.0103	0.1035	0.817	3.600
24.0	0.0099	0.1023	0.885	3.869	0.0097	0.1008	0.870	3.803
25.0	0.0093	0.0999	0.947	4.083	0.0092	0.0984	0.930	4.016

The number of digits is not representative for the accuracy of the results.

In this table the 'Root moment' is the blade root flap-bending moment at 0.432m radius and in a direction that differs 3deg from the rotor plane. This means that the definition corresponds with the moment from the strain gauge measurements.

It is remarkable that for wind velocities from 13m/s through 17m/s the blade root flapping moment and the shaft torque are larger if the tip-loss factor of Prandtl is used. The explanation is that due to the tip-loss factor (that account for the flow around the blade tips) stalling of the tip takes place at larger wind velocities.

A.4.2 Stationary properties for the phase-VI rotor in the NASA-Ames tunnel

For less theoretical but a more practical evaluation/comparison with the model of PHATAS, the aerodynamic properties are also calculated modelling all listed items that were excluded for the aerodynamic characteristics in the previous table. Here the rotor-speed was solved with the asynchronous generator torque-speed relation and transmission losses described in this appendix. The wind-speed was the ambient velocity measured in the NASA-Ames wind tunnel, while the air density was 1.245kg/m^3 for a wind velocity up to and including 10m/s, and 1.225kg/m^3 for the larger wind velocities.

The results of these calculations are:

Wind speed [m/s]	Air density [kg/m^3]	Rotor speed [rpm]	Power coeff	Thrust coeff	Aerod. power [kW]	Shaft torque [kNm]	Root moment [kNm]	Tip torsion [deg]
5.04	1.245	71.685	0.3597	0.5537	2.278	0.304	0.995	-0.0007
6.02	1.245	71.779	0.3750	0.5450	4.046	0.539	1.394	-0.0005
7.01	1.245	71.892	0.3626	0.5139	6.178	0.821	1.789	-0.0000
8.07	1.245	72.007	0.3208	0.4511	8.340	1.106	2.098	0.0006
9.01	1.245	72.098	0.2780	0.3966	10.057	1.332	2.285	0.0011
10.06	1.245	72.188	0.2336	0.3436	11.763	1.555	2.446	0.0013
11.04	1.225	72.190	0.1804	0.2945	11.810	1.562	2.481	0.0011
12.05	1.225	72.186	0.1378	0.2554	11.730	1.552	2.548	0.0006
13.05	1.225	72.167	0.1051	0.2231	11.366	1.505	2.579	-0.0001
14.08	1.225	72.111	0.0759	0.1960	10.315	1.367	2.586	-0.0010
15.09	1.225	72.046	0.0544	0.1741	9.093	1.206	2.568	-0.0021
16.12	1.225	71.987	0.0391	0.1582	7.969	1.058	2.608	-0.0034
17.10	1.225	71.950	0.0299	0.1461	7.265	0.965	2.669	-0.0045
18.11	1.225	71.956	0.0255	0.1372	7.373	0.979	2.794	-0.0056
19.09	1.225	71.961	0.0221	0.1299	7.466	0.992	2.927	-0.0066
20.13	1.225	71.965	0.0190	0.1234	7.559	1.004	3.078	-0.0077
21.13	1.225	71.971	0.0167	0.1181	7.670	1.019	3.237	-0.0086
22.07	1.225	71.978	0.0149	0.1139	7.800	1.036	3.396	-0.0095
23.21	1.225	71.986	0.0131	0.1094	7.962	1.056	3.599	-0.0105
24.11	1.225	71.994	0.0119	0.1064	8.103	1.075	3.767	-0.0114
25.11	1.225	72.004	0.0107	0.1033	8.279	1.099	3.963	-0.0123

For wind velocities larger than 20m/s the calculated elastic torsional deformation of the blade tip was -0.01deg or stronger. For wind velocities up to 15m/s the elastic tip torsional deformation was smaller than -0.002deg, of which the influence is assumed small and may be omitted. However, in the calculations with PHATAS the elastic blade torsional deformation was included.

APPENDIX B. THE PROGRAMS *INFLOW* AND *BEMINF*

In the spring of 2000 NREL performed an extensive series of measurements on the UAE phase-VI turbine in the wind tunnel of NASA-Ames. Part of these measurements were done for the stationary (non-rotating) conditions which were used to investigate the stationary aerodynamic coefficients of the S809 airfoil. Because of the finite length of the blade and because of the twisted geometry, the blade loading is not uniform over the span, even for the non-rotating conditions. The effects of the blade-loading on the air has an influence on the inflow distribution, especially on the rotor wake for the rotating conditions. The spanwise blade load distribution is related to a trailing-vortex structure in the wake, which can be used to calculate the local inflow conditions.

For the inflow distribution of a blade of which the load [N/m] was given for a number of spanwise locations (as for the UAE blade) the program *inflow* has been written. The initial version of the program *inflow*, see section B.1, was based on Prandtl's lifting-line theory for finite wings, which is described in chapter 5.3 of [4], and in chapter 11 of [55]. The final version was extended for the helical wake geometry of a rotating rotor, assuming that all blades behave identical, see section B.2. Finally a version *beminf* has been developed based on the BEM method, see section B.3. This version applies only to the rotating state, and was developed for verification of *inflow*. Because the results for the rotating measurements of the UAE phase-VI rotor were rather surprising, and because it was expected that future work will be performed within the IEA Annex-XX project, special attention was paid to the verification of *inflow*, which is reported in section B.4.

Another program LSIM (Lifting Surface Inflow correction Method) has been developed by Whale, Fisichella, & Selig [85] and applied for the un-tapered phase-III rotor. In the investigations of Whale et al. the relation between angle-of-attack and the inflow angles from the pitot-tubes was corrected for the finite-length (3D geometry) of the blades. Later Tangler used the similar tool LSWT (Lifting-Surface Prescribed Wake) inflow correction method for reconstruction of the angle-of-attack distribution of the UAE phase-VI rotor. A description of this method was given by Whale, Selig, and Tangler in Appendix O of the discussion-document for planning the NASA-Ames tests, edited by D. Simms e.a. [70].

B.1 Model for the Vortex Wake of a Non-Rotating Blade/Wing

For the calculations of the local inflow conditions of a non-rotating rotor or wing, the 'downwash' in the wake of the blade or wing is described in terms of a vortex structure. In this description, each part of air having some momentum compared to the outer fluid is enclosed by vorticity, from which one can easily understand that vortices cannot have a free end (Helmholz's theorem). The flow velocity in any point can be integrated straightforward from the vortex-description with the Biot-Savart law, where one must realise that vortices may *not* be seen as elements in the fluid having an acting force.

B.1.1 Vortex description of the blade lift distribution

The non-uniform loading on the blade/wing is described for a set of sections, having aerodynamic loads normal and tangential to the blade chord, and an aerodynamic moment m per unit span. These spanwise forces can be decomposed in lift f_l and drag f_d that are by definition 'perpendicular to' and 'in the direction of' the local flow. When describing the flow in terms of vorticity, the blade/wing has a bound vorticity distribution $\Gamma_{(r)}$ of which the strength is related to the lift with $\Gamma_{(r)} = f_{l(r)}/(\rho\, V_{\mathrm{eff}(r)})$, where $V_{\mathrm{eff}(r)}$ is the relative velocity perpendicular to the vortex at spanwise location r. For a non-rotating blade or wing, $V_{\mathrm{eff}} = U_{\mathrm{wind}}$. The flow around the (bound) vortex has an 'upflow' upwind of the vortex and a 'downwash' downwind of the vortex, while mathematically the flow has a singularity in the vortex center or 'core'. Here the local relative

flow direction is defined as the direction of the flow without the influence of the 'bound-vortex' itself, which can also be calculated from the average of the velocity a short distance upwind and the same distance downwind of the vortex Γ. The latter approach is sometimes used to obtain the angle-of-attack from the Navier-Stokes calculations.

Expressions for the (induced) inflow conditions

For a model of the blade/wing in terms of a lifting-line with vortex strength Γ, the trailing vorticity must be equal to its spanwise derivative: $\partial\Gamma/\partial r$.

Assumption 1. Use a finite number of blade segments

For practical applications such as the analysis of the measurements on the UAE rotor, the blade loading is known at a *finite number of locations* for which reason the vortex structure is described with a set of discrete trailing vortices that have a half-infinite length, see Figure B.1.

The Biot-Savart rule gives for any point the 'contribution' $\mathrm{d}\vec{V}$ to the local velocity related to a vortex-segment $\Gamma\,\mathrm{d}\vec{s}$ with vector-length $\mathrm{d}\vec{s}$. (It is tried to avoid words such as 'induced'.)

$$\vec{V} = \int_s \mathrm{d}\vec{V} = \int_s \Gamma\,\mathrm{d}\vec{s} \times \vec{p}/(4\,\pi\,|p|^3)\ .$$

Here $\vec{p}$ is the distance towards the vortex segment $\Gamma\,\mathrm{d}\vec{s}$ and $\vec{s}$ the length of the vortex segment.

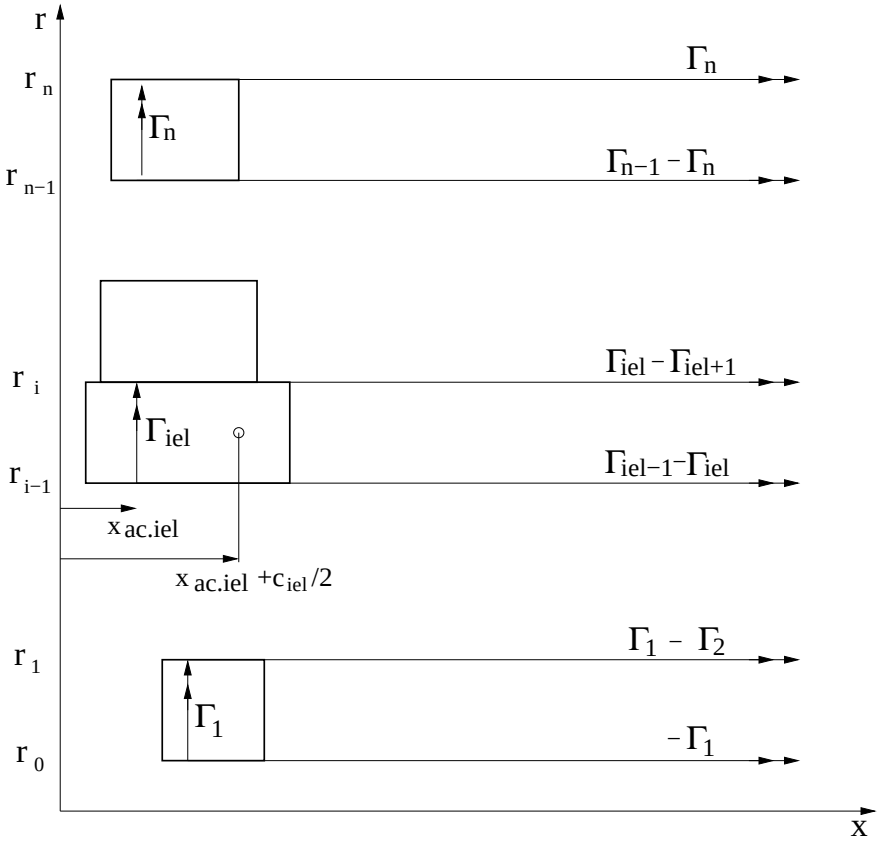

Figure B.1 *Vortex representation of a blade/wing with lifting segments*

Assumption 2. Assume a flat vortex wake geometry

The wake of the blade/wing has some downwash. For the description of the local velocities related to the wake structure the 'induced' velocity distribution at the blade/wing is calculated as if *the geometry of the wake is in a flat plane* through the x and r axes (downwind and spanwise). This means that the local velocity distribution has a normal component w only.

The vortex structure of a blade/wing contains bound vortices and semi-infinite trailing vortices. In the program *inflow* the blade/wing is divided in N sections, each with a constant bound vorticity, which gives $N+1$ trailing vortices, numbered from 0 at the root to N at the tip.

Assumption 3. Omit the contribution of the aerodynamic moment

For attached flow around flat airfoils without camber, the resulting lift force acts on the 25% chord location. Due to camber and flow separation the resulting force can act at a slightly different chordwise location, which is represented by the aerodynamic moment around the 25% chord location. In the program '*inflow*' *the contribution of the aerodynamic moment is omitted.*
In the 25% chord location of the mid-span of each of the elements, indicated with subscript iel, the vertical component of the 'induced' velocity is calculated from the contributions of the semi-infinite trailing vortices and the bound vortices for all elements.

Integration of the Biot-Savart law for the contribution to the vertical velocity in the origin, for a straight vortex Γ at a distance r from the x-axis ranging from x_1 to x_2 gives:

$$\Delta w = \frac{\Gamma}{4\pi r}\left(\frac{x_2}{\sqrt{{x_2}^2+r^2}} - \frac{x_1}{\sqrt{{x_1}^2+r^2}}\right) .$$

If x_2 goes to infinite and x_1 goes to minus infinite, the velocity becomes $\Gamma/(2\pi r)$ which is always directed radial to the vortex. It follows that integration of the radial velocity around an infinite vortex gives the vortex strength Γ.

B.1.2 Solution of the inflow distribution

For the integration of the contribution of all vortices in the wake of the blade/wing, the wake structure is described in terms of U-shaped (or 'horse-shoe') vortex systems for each of the elements iel. The vertical component w_i of the inflow velocity at the 25% chord location of the midspan of each element iel (with coordinates: $x_p = x_{ac.iel}$ and $r_p = (r_{i-1}+r_i)/2$) is integrated from the contribution of these U-shaped vortex systems:

$$w_i = \sum_{j=1}^{j=n} \frac{\Gamma_j}{4\pi}\,\frac{1}{(r_p - r_j)}\left(1 + \frac{x_p - x_{ac.j}}{\sqrt{(x_p - x_{ac.j})^2 + (r_p - r_j)^2}}\right)$$

$$- \sum_{j=1}^{j=n} \frac{\Gamma_j}{4\pi}\,\frac{1}{(r_p - r_{j-1})}\left(1 + \frac{x_p - x_{ac.j}}{\sqrt{(x_p - x_{ac.j})^2 + (r_p - r_{j-1})^2}}\right)$$

$$+ \sum_{j=1,\ j\neq i}^{j=n} \frac{\Gamma_j}{4\pi}\,\frac{1}{(x_p - x_{ac.j})}\left(\frac{r_p - r_j}{\sqrt{(x_p - x_{ac.j})^2 + (r_p - r_j)^2}} - \frac{r_p - r_{j-1}}{\sqrt{(x_p - x_{ac.j})^2 + (r_p - r_{j-1})^2}}\right)$$

In the last summation, describing the contribution of the bound vortices, the element iel itself is excluded. The contribution in this last summation is not evaluated if $(x_p - x_{ac.j})$ approaches zero, in order to avoid numerical errors. For these cases the physical contribution is also zero.

With the resulting vertical velocity the angle-of-attack at element i follows from $\alpha_{iel} = w_i/V$. This angle-of-attack is used to calculate the lift- and drag- forces from the normal- and tangential-force distribution.

Iterative solution method

The expressions described above can be used in a straightforward manner if the spanwise lift distribution is known. However, because the 'lift' is by definition perpendicular to the local flow direction, the measured (normal- and tangential-) blade loads can not directly be translated to lift and drag. In the program *inflow* the induced velocities are solved iteratively where in each iteration the normal force and tangential force distribution are decomposed in the lift and drag distribution using the angle-of-attack from the latest solution of the flow-field:

$f_{\mathrm{l},i} = f_{\mathrm{n},i} \cos\alpha_{i,\mathrm{eff}} + f_{\mathrm{t},i} \sin\alpha_{i,\mathrm{eff}}$;

$f_{\mathrm{d},i} = f_{\mathrm{n},i} \sin\alpha_{i,\mathrm{eff}} - f_{\mathrm{t},i} \cos\alpha_{i,\mathrm{eff}}$.

Here α_{eff} is the sum of the geometric angle of attack and the direction of the flow field $\alpha_i = w_i / U_{\mathrm{wind}}$.

For the measurements on the UAE rotor it appears that convergence of the solution is obtained after 4 iterations. To be conservative for slow converging conditions, 8 iterations are performed.

With the final solution of the flow velocity the aerodynamic coefficients of the airfoil are made dimensionless with $(\rho/2)\, c\, U_{\mathrm{wind}}^2$ with U_{wind} the undisturbed relative wind velocity. Formally the local vertical velocity w_i has to be included in the relative flow velocity on the blade element iel. However, because the geometry of the wake is assumed to be flat the longitudinal induced velocity is also omitted. Knowing that for a conservative flow, a vortex does not have a force in the flow-direction and thus will not change the dynamic pressure of the flow, the resulting velocity (including the 'induced velocity' components) must be equal to the undisturbed velocity. Note however that this only holds without pressure differences: Bernoulli's law.

B.1.3 Correction of the 2D a.o.a. for flow curvature

For airfoils the aerodynamic lift and drag coefficients are defined (provided- and used-) as the coefficients for stationary 2-dimensional flow. Without the local influence of its own circulation, the undisturbed flow for a long 2D airfoil is uniform and parallel. For this flow the angle-of-attack is the angle between the chord and the local relative flow direction.

For a finite blade/wing (which may also be rotating) the relative flow is curved, which is related to the semi-infinite trailing vorticity. Even for this curved flow the lift force is by definition still perpendicular to the flow direction in the location of the resulting lift. In the research for vertical-axis wind turbines the aerodynamics of an airfoil in curved flow are compared with an airfoil with additional 'virtual camber' in a uniform flow (see figure 5.4), for which a different set of aerodynamics have to be used, see also Cardona [12] and Mandal & Burton [50]

For attached flow around thin airfoils it can be shown on basis of thin airfoil theory that the effect of an additional camber is a shift in angle-of-attack for zero lift and an additional aerodynamic moment. For a uniform additional camber the shift in angle-of-attack is equal to the direction of the camberline at the 3/4 chord location. This shift in angle-of-attack (which in fact corrects for the 'virtual camber') is implicitly accounted for if the direction of the inflow condition is calculated at the 3/4 chord location, see also section 5.4. In this calculation, the contribution of the bound-vorticity of the airfoil to the flow at the 3/4 chord location has to be subtracted as if this is an infinitely long 2D lifting line.

For the inflow conditions including the 'virtual camber correction for flow curvature' the vertical velocity is calculated in: $x_{\rm p} = x_{{\rm ac},i} + c/2$ and $r_{\rm p} = (r_{i-1} + r_i)/2$. The contribution of all U-shaped vortex systems to the vertical velocity in $(x_{\rm p},\ r_{\rm p})$ gives:

$$
\begin{aligned}
w_i = & \sum_{j=1}^{j=n} \frac{\Gamma_j}{4\,\pi}\ \frac{1}{(r_{\rm p} - r_j)} \left(1 + \frac{x_{\rm p} - x_{{\rm ac},j}}{\sqrt{(x_{\rm p} - x_{{\rm ac},j})^2 + (r_{\rm p} - r_j)^2}} \right) \\
& - \sum_{j=1}^{j=n} \frac{\Gamma_j}{4\,\pi}\ \frac{1}{(r_{\rm p} - r_{j-1})} \left(1 + \frac{x_{\rm p} - x_{{\rm ac},j}}{\sqrt{(x_{\rm p} - x_{{\rm ac},j})^2 + (r_{\rm p} - r_{j-1})^2}} \right) \\
& + \sum_{j=1}^{j=n} \frac{\Gamma_j}{4\,\pi}\ \frac{1}{(x_{\rm p} - x_{{\rm ac},j})} \left(\frac{r_{\rm p} - r_j}{\sqrt{(x_{\rm p} - x_{{\rm ac},j})^2 + (r_{\rm p} - r_j)^2}} - \frac{r_{\rm p} - r_{j-1}}{\sqrt{(x_{\rm p} - x_{{\rm ac},j})^2 + (r_{\rm p} - r_{j-1})^2}} \right) \\
& + \frac{\Gamma_i}{2\,\pi\,(x_{\rm p} - x_{{\rm ac},i})}\ .
\end{aligned}
$$

The first two summations are similar to those for the flow velocity at the 25% chord location. The very last term in this expression is opposite to the influence of the 'downwash' at the 3/4 chord location of element iel itself as if this element is part of an infinitely long 2D lifting line.

The angle-of-attack of element i for which the 2D aerodynamic coefficients are expressed follows from $\alpha_{\rm curved,2D} = w_i / U_{\rm wind}$. Note that this angle-of-attack is not used for the decomposition of the normal forces and tangential forces into lift and drag, which is still done following section B.1.2.

With the program *inflow* the calculation of the induced velocities, and thus the angle-of-attack, can be done following the approach to correct for the flow curvature, such as described above, or simply at the 1/4 chord location, which is also used to calculate the lift and drag from the normal- and tangential- force. The user can chose between those methods with the input item '**chord_effects**', see section B.4.

B.2 Model for the Helical Vortex Wake of a Rotating Rotor

With the initial version of the program *inflow* for the induced velocity of a non-rotating blade the aerodynamic coefficients can be retrieved reasonably well, see chapter 3. However for wind turbine rotors the aerodynamic coefficients are needed for the rotating case, for which empirical models have been derived, see section 4.3 through 4.5. For the verification of the empirical models with the measurements on the UAE phase-VI turbine in the NASA-Ames wind tunnel, the program *inflow* was improved to describe the helical wake structure of a rotating blade.

Because of the geometrical complexity of the helical wake structure the induced velocities of this vortex structure are integrated numerically using the Biot-Savart law. For this integration the wake is still described with discrete trailing vortices that leave the blade at the intersections of the blade elements. This implies that the bound vorticity of the rotating blade is assumed to be constant over each blade element, where the blade-element intersections are modelled between the locations where the blade loads are given: the instrumented blade sections.

B.2.1 Velocities of the helical wake structure

For the integration of the induced velocities on the rotor blades the helical wake geometry is assumed continuous in downwind direction. This means that effects associated with wake expansion are not included, but that the downwind-distance between the trailing vortex sheets is included using the induced velocities short downwind of the rotor disk.

In general the deformation of the wake is characterised by a radial expansion, and a longitudinal contraction in downwind direction, while the wake also has some rotation which is in balance with the torque on the rotor. The induced velocities in the rotor plane have the strongest influence from the wake vorticity short behind the rotor plane. So for the sake of simplicity, the velocities short behind the rotor plane are used to describe the downwind geometry of the wake structure. Short behind the rotor the average axial induced velocity $\bar{U}_{\text{i.an}}$ is half of the value for the loss of axial momentum. The tangential induced velocity short behind the rotor plane is $2\ \bar{V}_{\text{i.an}}$, which is the complete loss of tangential momentum because no torque is acting downwind of the rotor.

Using the angle θ_{eff} for the sum of the blade pitch angle and the local twist angle, the annulus-average induced velocities apply to the momentum equations:

$$B\, f_{\text{l}}\, \cos(\theta_{\text{eff}} + \alpha)\, \Delta r = \rho\, 2\, \pi\, r\, \Delta r\, (U_{\text{wind}} - \bar{U}_{\text{i.an}})\, 2\, \bar{U}_{\text{i.an}}\ .$$

$$B\, f_{\text{l}}\, \sin(\theta_{\text{eff}} + \alpha)\, \Delta r\, /\, \cos\alpha_{\text{c}} = \rho\, 2\, \pi\, r\, \Delta r\, (U_{\text{wind}} - \bar{U}_{\text{i.an}})\, 2\, \bar{V}_{\text{i.an}}\ .$$

These equations may be compared with (5.1) and (5.2) and hold for small values of the induced velocity of a B bladed rotor, $\bar{U}_{\text{i.an}} << U_{\text{wind}}$ (so not in the 'turbulent wake state').
The lift per unit span f_{l} follows from the 'measured' load distribution: $f_{\text{l}} = f_{\text{n}}\, \cos\alpha + f_{\text{t}}\, \sin\alpha$.
Here Δr is the width of an annulus in radial direction, which is related to the length of a blade element by $\Delta r = \Delta s\, \cos\alpha_{\text{c}}$. Remind that (as explained in section 5.2) the induced velocities from the aerodynamic drag should *not* be included for the description of the trailing vortex structure short behind the rotor disk.

The annulus-average axial induced velocity follows directly from (see also section B.3):

$$\bar{U}_{\text{i.an}} = 0.5\, U_{\text{wind}}(\, 1 - \sqrt{1 - B\, f_{\text{l}}\, \cos(\theta_{\text{eff}} + \alpha)/(\pi\, \rho\, r\, U_{\text{wind}}^{\,2})}\,)\ .$$

Next the annulus-average tangential-induced velocity follows from:

$$\bar{V}_{\text{i.an}} = B\, f_{\text{l}}\, \sin(\theta_{\text{eff}} + \alpha)\, /(\rho\, 4\, \pi\, \rho\, r\, \cos\alpha_{\text{c}}\, (U_{\text{wind}} - \bar{U}_{\text{i.an}}))\ .$$

These induced velocities are properties of the annular streamtubes and thus related to the blade elements. The trailing vortices are in between these annular streamtubes. On basis of the so-called 'roller-bearing' analogon, the trailing vortices move with the averages of the velocities of the neighbouring annular streamtubes.

B.2.2 Geometry of the helical wake structure

The integration of the induced velocity in the program *inflow* is performed for blade 1, which is assumed in the vertical position. For a time $t_j = j\, \Delta t$ in the 'wake history', the vortex leaving node $inod$ of blade ibl is at position (with respect to the rotor centre):

$$\vec{P}(j,\, ibl,\, inod) = \begin{pmatrix} s_{inod}\ \sin\alpha_{\text{c}} + (U_{\text{wind}} - (\bar{U}_{\text{i.an}}(iel) + \bar{U}_{\text{i.an}}(iel{+}1))/2)\, t_j \\ r_{inod}\ \sin(\,(\Omega + (\bar{V}_{\text{i.an}}(iel) + \bar{V}_{\text{i.an}}(iel{+}1))/r_{inod})\, t_j + 2\, \pi\, (ibl - 1)/B\,) \\ r_{inod}\ \cos(\,(\Omega + (\bar{V}_{\text{i.an}}(iel) + \bar{V}_{\text{i.an}}(iel{+}1))/r_{inod})\, t_j + 2\, \pi\, (ibl - 1)/B\,) \end{pmatrix}\ .$$

Node $inod$ (ranging from 0 to N) is between blade element iel and $iel + 1$, with N the number of blade elements. Inside of the wake (iel = 0) and outside of the wake (iel = N+1) the average induced wake velocities are zero.

The direction of a vortex-segment Δt follows from the derivative of the location with respect to the down-wind time coordinate:

$$\vec{r} = \frac{\partial \vec{P}(j,\, ibl,\, inod)}{\partial t} = \begin{pmatrix} (U_{\rm wind} - (\bar{U}_{\rm i.an}(iel) + \bar{U}_{\rm i.an}(iel{+}1))/2) \\ r_{inod}\,(\Omega + (\bar{V}_{\rm i.an}(iel) + \bar{V}_{\rm i.an}(iel{+}1))/r_{inod})\cdot \\ \cos(\,(\Omega + (\bar{V}_{\rm i.an}(iel) + \bar{V}_{\rm i.an}(iel{+}1))/r_{inod})\,t_j + 2\,\pi\,(ibl-1)/B\,) \\ -r_{inod}\,(\Omega + (\bar{V}_{\rm i.an}(iel) + \bar{V}_{\rm i.an}(iel{+}1))/r_{inod})\cdot \\ \sin(\,(\Omega + (\bar{V}_{\rm i.an}(iel) + \bar{V}_{\rm i.an}(iel{+}1))/r_{inod})\,t_j + 2\,\pi\,(ibl-1)/B\,) \end{pmatrix} .$$

B.2.3 Numerical integration

Similarly as for the initial ('non-rotating') version of *inflow* the induced velocities, the aerodynamic lift coefficients, and the strength of the bound- and trailing- vortices are solved in an iterative procedure. In this procedure the induced velocities are calculated at the 1/4 chord locations of the blade elements, which is done by integration of the influence of the wake vortex structure using the Biot-Savart law.

This integration is done for a finite distance of the wake in downwind direction. Because vortex systems must be closed structures (Helmholz theorem), the trailing vorticity at the down-wind end of the wake structure was 'closed' by the 'initial shed-vorticity' such that the vortex system still represents a consistent state of flow. The truncation of the wake, together with the contribution of the artificial 'shed-vorticity' means in fact that the influence of the far downwind part of the wake is omitted. This omission was compensated in the program *inflow* with the analytical expressions of the axial induced velocity of a far downwind cylindrical wake on the form of:

$$U_{\rm i.far} = (\,1 + \arctan((U_{\rm wind} - U_{\rm i.an})\,t_{\rm end}, R)\,)\,\bar{U}_{\rm i.an}\ .$$

In fact the radial distribution of the annular induced velocities in the wake is integrated. The contribution of the far wake to the tangential induced velocity is zero.

The integration of the induced velocities starts at the downwind end of the wake and ends near the rotor so that the largest contributions are added last and the numerical round-off errors are minimised. Also for the minimisation of the numerical round-off errors, the integration starts with blade number B and ends with blade number 1, where the last is the blade for which the induced velocities are integrated.

B.3 Version based on the inverse BEM method

In the practise of wind turbine engineering the Blade Element Momentum method (BEM) is used to calculate the velocities at the rotor plane and the corresponding angle-of-attack distribution of the rotor blades. The BEM method has the advantage that it is relatively fast and that it is accurate for rotors with a not too small tip-speed ratio at zero or moderate yaw angles.

In the BEM approach the flow is distributed in annular streamtubes for which the blade loads are equated to the loss of axial and tangential momentum. Instead of solving the blade loads and inflow conditions that fit to the aerodynamic coefficients, the momentum equations of the BEM method were applied here to solve the aerodynamic coefficients and angles-of-attack from the blade loads. This application is called 'inverse BEM' approach, and is the basis for the version '*beminf*' of the program *inflow*. The version '*beminf*' has nearly the same input structure, with an additional input item **tip_losses** with which one can chose to apply the factor of Prandtl to correct for the flow around the root and tip, or not. The program *beminf* includes the effects of cone angle. The loss of momentum due to aerodynamic drag is not included for the calculation of the induced velocity at the rotor plane, for reasons explained in section 5.2.

Solution method

In *beminf* the inflow conditions are described with the annulus average axial and tangential induced velocities $\bar{U}_{\mathrm{i.an}}$ and $\bar{V}_{\mathrm{i.an}}$. Because the current version of *'beminf'* uses only the lift for the induced velocities at the rotor disk, an iterative solution is applied. After initialising the induced velocities on zero, this iteration proceeds as follows:

1. Assign the inflow angle: $\phi_{\mathrm{inf}} = \arctan(\,(U_{\mathrm{wind}} - U_{\mathrm{i}})\cos\alpha_{\mathrm{c}}/(\Omega\, r\, +\, V_{\mathrm{i}})\,)$.
2. Assign the effective angle-of-attack: $\alpha_{\mathrm{eff}} = \phi_{\mathrm{inf}} - \theta_{\mathrm{twist}} - \theta_{\mathrm{pitch}}$.
3. Assign the axial force coefficient: $C_{\mathrm{d.ax}} = B\,(f_{\mathrm{n}}\,\cos\alpha_{\mathrm{eff}} + f_{\mathrm{t}}\,\sin\alpha_{\mathrm{eff}})\,\cos\phi_{\mathrm{inf}}/(\pi\,\rho\,r\,U_{\mathrm{wind}}^{\,2})$.
4. Solve the annulus-average axial induced velocity: $\bar{U}_{\mathrm{i.an}} = 0.5\,U_{\mathrm{wind}}\,(\,1 - \sqrt{1 - C_{\mathrm{d.ax}}}\,)$.
   For turbulent wake state ($C_{\mathrm{d.ax}} > 0.9424$) use: $\bar{U}_{\mathrm{i.an}} = U_{\mathrm{wind}}\,(C_{\mathrm{d.ax}} - 0.5776)/0.96$.
5. Assign the annulus-average tangential induced velocity:
   $\bar{V}_{\mathrm{i.an}} = B\,(f_{\mathrm{n}}\,\cos\alpha_{\mathrm{eff}} + f_{\mathrm{t}}\,\sin\alpha_{\mathrm{eff}})\,\sin\phi_{\mathrm{inf}}/(\,4\,\pi\,\rho\,r\,\cos\alpha_{\mathrm{c}}\,(U_{\mathrm{wind}} - \bar{U}_{\mathrm{i.an}})\,)$.
6. Assign the Prandtl factors for root and tip-loss.
   For tip loss this is: $F_{\mathrm{tip}} = 2/\pi\,\arccos(e^{-\pi(R-r)/d})$.
   For root loss this is: $F_{\mathrm{root}} = 2/\pi\,\arccos(e^{-\pi(r-r_{\mathrm{root}})/d})$.
   Here d is the trailing-vortex distance:
   $d = (2\,\pi\,r/B)\cdot(U_{\mathrm{wind}} - 0.5\,\bar{U}_{\mathrm{i.an}})/(\,(\Omega\,r + \bar{V}_{\mathrm{i.an}})^2 + (U_{\mathrm{wind}} - 0.5\,\bar{U}_{\mathrm{i.an}})^2\,)$.
7. Assign the induced velocities at the blades: $U_{\mathrm{i}} = \bar{U}_{\mathrm{i.an}}/(F_{\mathrm{tip}}\,F_{\mathrm{root}})$ and $V_{\mathrm{i}} = \bar{V}_{\mathrm{i.an}}/(F_{\mathrm{tip}}\,F_{\mathrm{root}})$.

Realise that for zero blades ($B = 0$) the induced velocities are zero.
After 8 iterations (fairly sufficient) the aerodynamic coefficients are calculated:

$c_{\mathrm{l}} = (f_{\mathrm{n}}\,\cos\alpha_{\mathrm{eff}} + f_{\mathrm{t}}\,\sin\alpha_{\mathrm{eff}})/(\,0.5\,\rho\,c((\cos\alpha_{\mathrm{c}}(U_{\mathrm{wind}} - U_{\mathrm{i}}))^2 + (\Omega\,r + V_{\mathrm{i}})^2)\,)$.
$c_{\mathrm{d}} = (f_{\mathrm{n}}\,\sin\alpha_{\mathrm{eff}} - f_{\mathrm{t}}\,\cos\alpha_{\mathrm{eff}})/(\,0.5\,\rho\,c((\cos\alpha_{\mathrm{c}}(U_{\mathrm{wind}} - U_{\mathrm{i}}))^2 + (\Omega\,r + V_{\mathrm{i}})^2)\,)$.
$c_{\mathrm{m}} = m_{\mathrm{aero}}/(\,0.5\,\rho\,c^2((\cos\alpha_{\mathrm{c}}(U_{\mathrm{wind}} - U_{\mathrm{i}}))^2 + (\Omega\,r + V_{\mathrm{i}})^2)\,) + 0.39\,\sin\alpha_{\mathrm{c}}\,\cos\phi_{\mathrm{inf}}\,(c/r)$.

While the non-rotating angle-of-attack is:

$\alpha = \alpha_{\mathrm{eff}} + \sin\alpha_{\mathrm{c}}\,\cos\phi_{\mathrm{inf}}\,(c/2 + y_{\mathrm{ac}})/r$.

Comparison with the vortex-wake version

Using *beminf* for the non-rotating measurements on the UAE phase-VI rotor in the NASA-Ames wind tunnel gives aerodynamic coefficients that are similar as those obtained with the vortex-wake based method *inflow*. The largest discrepancies occur for the angles-of-attack of the 30.0% section, while the lift coefficients obtained with both programs are high (2.3 with *inflow* and 2.5 with *beminf*). For the midspan and outer sections the coefficients from *beminf* and *inflow* have small differences, which shows among others that the Prandtl factor in the BEM approach is not bad.

As can be expected from the assumptions of the BEM approach, the accuracy of *beminf* for non-rotating cases but also for very low tip-speed ratios is bad. Using *beminf* to retrieve the aerodynamic coefficients from the non-rotating measurements on the UAE phase-VI rotor show that the induced angles-of-attack are about half of that from the vortex-wake version *inflow*.

B.4 Using the Programs *inflow* and *beminf*

The program *inflow* is a so-called 'batch oriented' program that is invoked by typing its name `inflow` followed by up to 3 `CHARACTER*64` arguments for the names of the files:

1. Input file with blade properties. If is not specified *inflow* looks for a file named '*inflow.in*';
2. Measured properties. This argument will override the input value for **input_table** ;
3. Output file. If this name is not specified *inflow* writes its output to file '*inflow.out*'.

Similarly *beminf* is invoked by typing `beminf` followed by the same arguments.

B.4.1 Input file

The input file of *inflow* is read as `CHARACTER*80` records. The input items are to be defined with a 'key-name value' structure. Comments can be written in this file when starting with one of the three characters `<` `#` `/` .

Following is a description of the input items in alphabetic order, containing:

- the **key-name** in **bold face** ;
- the `type` in `typewriter` in accordance with the FORTRAN variable type ;
- the (default values) between ordinary ( ) brackets ;
- if applicable, the [unit] between square [ ] brackets ;
- if applicable, the <allowable range> between angled <> brackets ;
- an explanation in normal font .

The input items with a grey bar in the margin do not apply to the initial version of *inflow* which is for the wake of a non-rotating rotor or wing.

cone_angle `REAL` (0.0) [deg] $< -80.0 .... 80.0 >$
Cone angle of the rotor blades.

chord_effects `LOGICAL` ('*OFF*')
If '*ON*' the inflow velocity distribution is calculated at the 75% chord location and next corrected for the downwash at this location following the 2D flow of the local vorticity as if the blade/wing is infinitely long.
For the version *beminf* a correction for the 'virtual camber' is applied on the angle-of-attack, such as described in section 5.4. This correction is not used to decompose the normal and tangential forces into lift and drag.
If '*OFF*' the inflow velocity distribution is calculated directly for the 25% chord locations.

input_table `CHARACTER*64` ('*measured.in*')
The name of the file with measured properties. If a second command line argument is given, this will override the name specified by **input_table**.

nr_blades `INTEGER` (1) <0, ..., 4>
Number of blades on the rotor. The induced velocities are integrated for the vortex structure of '**nr_blades**' equally loaded rotor blades. This means that if '**nr_blades**' is set to '0', the aerodynamic coefficients are calculated *without* the induced velocities.
For the version *beminf* the loss of momentum is equated to the aerodynamic loads of **nr_blades** blade elements which has no maximum.

pitch_error `REAL` (0.0) [deg] <0.0, ...>
Error in the measured pitch angles. In the program *inflow* the value for '**pitch_error**' is subtracted from the pitch angle in the file with the measured properties.

root_radius `REAL` (0.0) [m] <0.0, ...>
Spanwise coordinate of the root of the blade/wing.
This is used for the origin r_0 of the most inner trailing vortex.

tip_radius `REAL` (1.0) [m] <**root_radius**, ...>
This is used for the spanwise location at which the tip trailing vortex leaves the blade/wing. The value of **tip_radius** should be larger than that of **root_radius**.

tip_losses `LOGICAL` (*'OFF'*) [m] <**root_radius**, ...>, Only for *beminf*!
If *'ON'* the loss factor of Prandtl is used to account for the flow around the tip and the root, using **root_radius** and **tip_radius**.

wake_geometry `LOGICAL` (*'OFF'*), Not for *beminf*!
If *'ON'* use a wake geometry of which the distance between the vortex-sheets is calculated with the induced velocities short behind the rotor. These induced velocities are calculated with an 'inverse BEM method'. This option does *not* improve the accuracy for non-rotating conditions.
If *'OFF'* use a 'fixed' vortex wake geometry independent of the induced velocities.

sectional_data `TABLE`
Contains the spanwise distribution of cross sectional properties, from root to tip for a maximum of 16 locations. The key-name **sectional_data** is to be followed by a table with on each row 4 `REAL` numbers for:

- Spanwise location [m] for the properties;
- Blade chord [m];
- Blade twist [deg];
- Chord-wise location of the aerodynamic centre (usually 25% chord line) [m].

Reading of this table is continued as long as the records end with a 'comma' and as long as the input file is not empty. The spanwise locations must form an increasing series and must all be within the range < **root_radius** ..... **tip_radius** >.

The input item **sectional_data** should be the last one in the input file which means that specifications following this item are not read.

```
/  'inflow' input file for the rotating measurements
/  on the UAE phase-VI rotor in the NASA-Ames tunnel.
/
/  Edited by  C. Lindenburg;  June 3,  2003.
/
input_table    rot_meas.in
/
root_radius    1.1    < [m]  Root-vortex radius used in PHATAS.
/
tip_radius     5.029  < [m]  Outer radius of wing or blade.
/  Following begin and end point approach the trailing vortices.
tip_radius     4.97   < [m]  Gives realistic drag coeff's at the tip.
/
nr_blades      2
chord_effects  ON
wake_geometry  ON
/
/  Following is a table with the geometrical
/  properties for which the sectional loads are given.
/  Span  Chord   Twist    Xac
/   [m]   [m]    [deg]    [m]
sectional_data
  1.510  0.711 16.067  -0.03555,
  2.343  0.627  6.49   -0.03135,
  3.185  0.542  2.89   -0.0271,
  4.023  0.457  1.394  -0.02285,
  4.780  0.381  0.306  -0.01905
/
```

Figure B.2 *Example of input file for the program 'inflow'*

B.4.2 File with measured properties

The second command-line argument of *inflow* or *beminf* is the name of the file with the sectional loads for a series of conditions. These conditions can be for e.g. increasing wind velocities or for 'pitch sweeps'. This file should contain a table of which the columns contain the REAL numbers:

1. Density of the air [kg/m^3] < 0.0001 .... >[kg/m.
2. The undisturbed wind velocity [m/s] <1.0E-7, ...>.
3. The pitch angle [deg], defined as for rotor blades.
4. Rotational speed of the rotor [rpm] <0.0, ...>
   This is used for the geometry of the vortex wake structure.
5. Normal force [N/m] for the 1-st section specified under **section_data**.
   This normal force is defined perpendicular to the local chord.
6. Tangential force [N/m] for the 1-st section specified under **section_data**.
   This tangential force is defined positive to the leading edge.
7. Aerodynamic moment [Nm/m] for the 1-st section specified under **section_data**.
   This tangential force is defined positive to the leading edge.

The last three columns have to be repeated for each instrumented section (each record) specified under '**sectional_data**'. This means that if the geometric properties for 5 sections are specified, the file with measured properties should contain 4 + (5 * 3) = 19 columns.

B.4.3 Output file with aerodynamic coefficients

The output file of the program '*inflow*' contains a heading of 3 records, followed by a table with the aerodynamic coefficients for all locations. The records in this table contain:

1. Angle of attack [deg] for the aero. coefficients for the 1-st section specified under **section_data**.
2. Aerodynamic lift coefficient for the 1-st section specified under **section_data**.
3. Aerodynamic drag coefficient for the 1-st section specified under **section_data**.
4. Aerodynamic moment coefficient for the 1-st section specified under **section_data**.

These four properties are repeated for each of the sections specified under **section_data**.

B.5 Verification

The program '*inflow*' plays a crucial role in the processing of the measured data to (rotating) aerodynamic coefficients. To verify its proper functioning, several checks have been performed. A number of these checks were addressed to the *consistency* of the program, which includes:

- For the non-rotating measurements, shifting the blade description 10m;
- For the non-rotating measurements, using a 'mirrored' blade description;
- For the rotating measurements, adding a section with zero-loads at the root and tip.
- For the non-rotating and for the rotating measurements, scaling the dimensions 10x;
- For the rotating measurements, scaling the loads and air density 10x;
- Without using chord-related effects, exchanging normal force and tangential force and adding 90deg to the twist. This gave 90deg shifted aerodynamic coefficients.
- Initialising the induced velocities in *inflow* on 30% of the wind instead of zero.

For the fourth verification, the rotor-speed was decreased 10x and the blade loads were increased 10x (aero-moments 100x). The last verification was done to see whether different solutions could be possibly found. The consistency for "increasing wind velocity and blade loads" was implicitly verified by the good correlation between the coefficients from the non-rotating cases at 20m/s and 30m/s wind and by the verification for a 10x increased air density. For the non-rotating measurements a verification was done by comparing the results with the initial version of '*inflow*', which is based on an analytical solution following 'wing theory'. Because the latter solution

holds for a flat wake, this verification was done with '**wake_geometry** OFF' and showed a good agreement between both codes.

Verification with the BEM model in PHATAS

The global function of the program '*inflow*' is in fact the inverse of what is done with wind turbine analysis codes such as PHATAS. This means that if both PHATAS and '*inflow*' are correct, the blade load distribution calculated with PHATAS can be used as input for '*inflow*' which should reproduce the tables with aerodynamic coefficients that were input of PHATAS.

This approach was used in the following verification. Since the flow around the blade tips is described by PHATAS with the Prandtl factor in the BEM model and by '*inflow*' with a (non-expanding) vortex-wake model an identical result is not expected. Because this exercise was addressed to verification of the model in '*inflow*' the blade deformation, the aerodynamic tower stagnation and the rotational effects on the aerodynamic coefficients were eliminated. With PHATAS the normal- and tangential- forces [N/m] are calculated for the 5 radial locations [m] that are close to the instrumented sections of the UAE phase-VI rotor:

```
 1.4709  2.3249  3.1788  4.0327  4.8155 .
```

The aerodynamic lift coefficients calculated with '*inflow*' for the two inner and the two outer locations are shown in Figure B.3, together with the non-rotating S809 coefficients that were input for the PHATAS calculation. The root and tip vortices used for *inflow* were 1.07m and 5.029m.

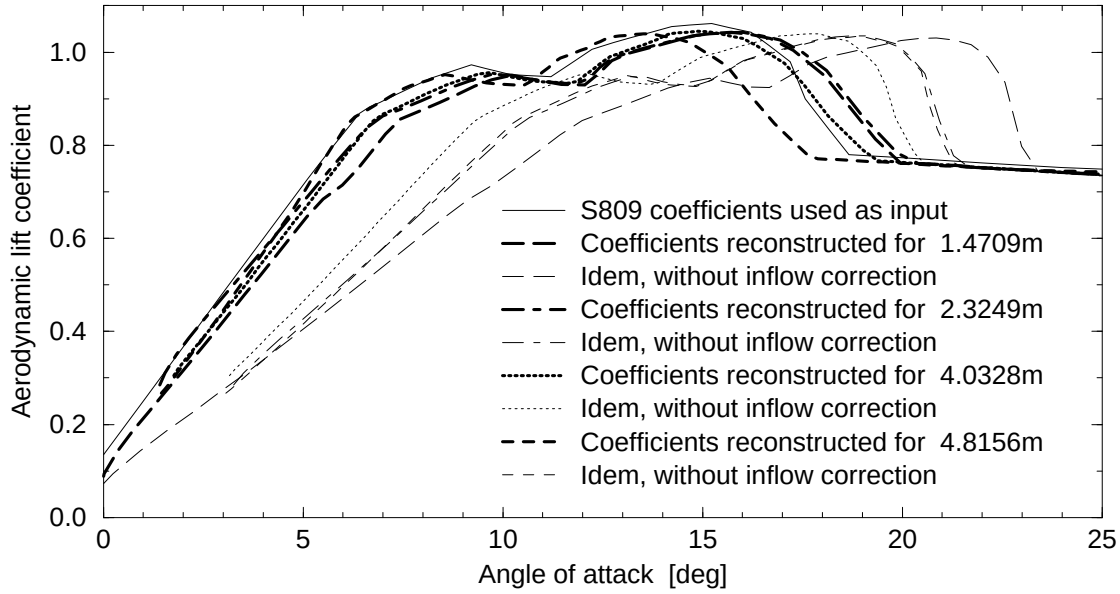

Figure B.3 *Aerodynamic lift coefficients reconstructed from PHATAS blade loads*

Figure B.3 shows that without correcting for the induced velocities the angles-of attack are too large. With the corrections as modelled in '*inflow*' the angles-of-attack appear to be quite realistic except for the stall region of the root and the tip sections. Although not plotted, the lift coefficients for the 3.1788m section are about the same as for the 4.0327m section, which both have a slope of the lift-curve that is a little too small.
The discrepancy for the outer section (near 4.8155m) shows that for large tip-vortex distances the factor of Prandtl differs from the tip-flow described with a vortex-wake model.

Application of '*inflow*' with the smaller root vortex radius of 1.0m gives a slightly more realistic lift curve near the root. This indicates the importance of the influence of the root vortex, not only for reconstructing aerodynamic coefficients but also in BEM codes for wind turbine analyses.

The aerodynamic coefficients reconstructed with *beminf* come very close to those in the original file, which again shows that the procedure in *beminf* is the inverse of that in PHATAS.

Verification for a model with more segments

Questions have arisen to what extent the number of sections have an influence on the aerodynamic coefficients retrieved with *inflow*. This was also investigated by the using the blade load distribution from the PHATAS calculation as in the previous exercise, but then for the locations:

```
1.1863 1.4709 1.7556 2.3249 3.1788 4.0327 4.6020 4.8155 4.9578 .
```

These locations coincide with the middle of the blade elements in the PHATAS model. From the blade loads (normal- and tangential- force) distribution was used to retrieve the aerodynamic coefficients with *inflow*. For the locations 1.4709m, 2.3249m, and 4.6020m these coefficients are plotted in Figure B.4 together with the coefficients obtained with the loads from 5 sections.

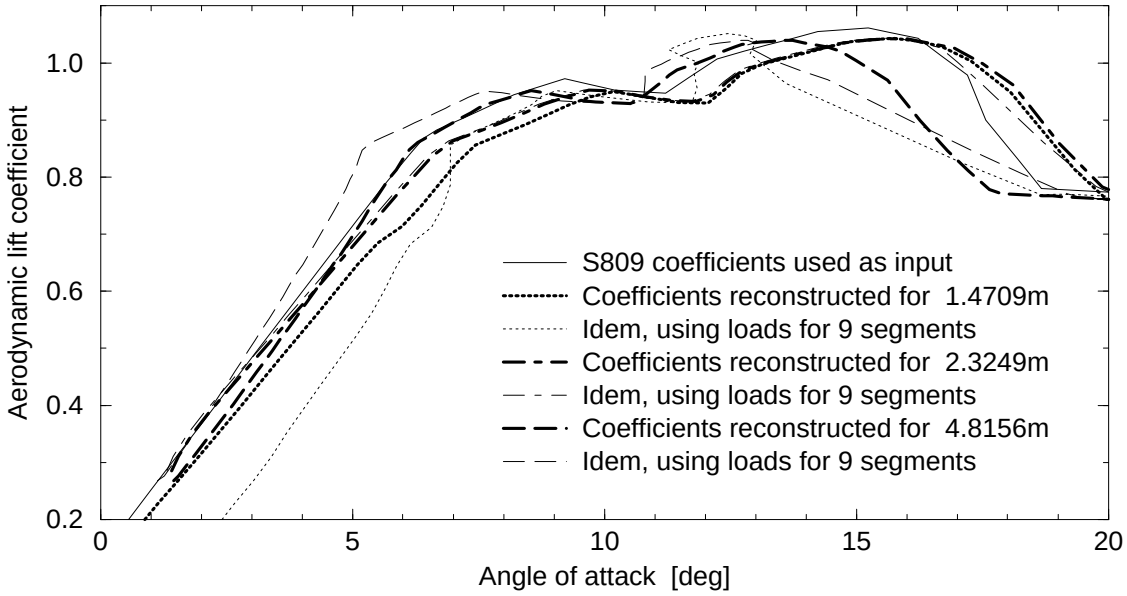

Figure B.4 *Aerodynamic lift coefficients reconstructed with different sections*

From Figure B.4 it follows that with blade loads for 9 sections the aerodynamic coefficients for r =1.4709m are less realistic than the coefficients retrieved with loads for 5 sections. This shows that the number of sections have a large influence on the coefficients retrieved with *inflow*. In general it may be concluded that using a BEM code with the Prandtl factor for the tip-flow (and root-flow) effects differs from a vortex-wake description.

For more thorough evaluation of the tool *inflow* it is suggested to perform a similar exercise where the blade load distribution is generated with e.g. the vortex-wake code *AWSM*.

EXECUTIVE SUMMARY

Goal

The project *NASA-Ames Rotorblad Aerodynamica* (Dutch) aims at reducing the uncertainty in the design programs for the aerodynamic (also aero-elastic) behaviour of horizontal axis wind turbines, HAWT's. This was done by participation in the so-called 'Blind Comparison', and by exploration of the measurements on the experimental 'UAE' rotor of NREL in the NASA-Ames wind tunnel. The latter was supported by a literature survey on wind turbine aerodynamics.

Introduction

In the spring of 2000 the NWTC ('**N**ational **W**ind **T**echnology **C**enter') of NREL ('**N**ational **R**enewable **E**nergy **L**aboratory') in Golden, Colorado, placed their 10m diameter 2-bladed UAE ('**U**nsteady **A**erodynamic **E**xperiment') test turbine in the 24m x 36m wind tunnel of NASA-Ames in California. For the period of a month measurements were collected that include the aerodynamic pressure distributions from 5 fully instrumented sections. In the fall of 2000 NREL organised a so-called 'Blind Comparison' for which wind turbine research institutes (worldwide) were invited to calculate the aerodynamic loads for some stationary conditions. ECN participated in this Blind Comparison with their program PHATAS (**P**rogram for **H**orizontal **A**xis wind **T**urbine **A**nalysis and **S**imulation). Although the results calculated with PHATAS also deviated from the measurements, they were roughly in the middle of the results calculated by the other participants of the Blind Comparison.

The aerodynamics of wind turbine rotors are difficult to model because of:
- the complex geometry of the wake structure, compared with e.g. the wake of an aircraft wing;
- the instationary nature of the aerodynamics, that are dominated by the turbulent wind;
- the effects of rotation on rotor aerodynamics;
- the fact that the design loads have to be calculated for various conditions.

Work Approach

The aerodynamics of wind turbine rotor blades involves various aspects such as the lack of aerodynamic coefficients in deep stall, the effects of rotation, instationary aerodynamics, and yawed operation. The rotor aerodynamics are also investigated within the joint IEA project annex-XX which is also based on the investigation of the measurements on the UAE rotor. Knowing that this IEA annex-XX project is in fact a 'follow-up' of the work reported here, and knowing that within this project ECN has planned to focus on the instationary aerodynamics, emphasis was given here on an accurate and reliable description of the UAE phase-VI rotor, while the investigations were addressed to the stationary rotor-blade aerodynamics. This dealt with the non-rotating conditions and later with the rotating conditions. Based on the insight obtained from the literature and from the NASA-Ames measurements, the models for the BEM-based codes BLADMODE and PHATAS have been improved.

Results

Non-rotating aerodynamic coefficients in deep stall

The aerodynamic coefficients of most airfoils are measured up to stall. For the estimation of the aerodynamic coefficients in deep stall on basis of the global airfoil geometry, the program *StC* ('**St**all **C**oefficients') has been developed earlier. Within the project 'NASA-Ames Rotorblad Aerodynamica' the empirical relations in *StC* (for normal- and tangential- force) were improved by comparison with measured deep-stall coefficients from various publications, esp. for VAWTs.

Aerodynamic coefficients of the S809 airfoil

For the S809 airfoil the 2D-dimensional coefficients from several wind tunnel tests and from some airfoil design codes were collected and compared. On basis of this information and the discussions with airfoil aerodymicists, a table with non-rotating aerodynamic coefficients of the S809 airfoil has been defined for a Reynolds number of $1{\cdot}10^6$. For deep stall the coefficients were added using the improved program *StC*. Finally serious effort was spent on an accurate aerodynamic modelling of the UAE phase-VI rotor blade.

Models for the effects of rotation on blade aerodynamics

The increased lift coefficients of rotating blades compared to non-rotating blades is referred to as 'rotational augmentation' or 'stall delay'. A literature survey was carried-out into other investigations and models dealing with the effects of rotation on blade aerodynamics. Three models for rotational augmentation have been investigated and compared qualitatively. One of these models (based on 'centrifugal pumping') was formulated within this project and has strong similarities with some other models. Although the existing model of Snel et al. has been improved and the 'centrifugal pumping' model also shows quite realistic, still some questions remain that are formulated as recommendations for future work within the IEA annex-XX project.

Modelling of blade tip aerodynamics

The current aerodynamic models still show an over-prediction of the loads near the blade tip, in particular for 2-bladed rotors. Within this project, the implementation of the tip-loss factor of Prandtl has been improved (so not the Prandtl factor itself) while an empirical model has been derived for the reduction of the sectional loads towards the blade tip.

Improved wind turbine design programs BLADMODE and PHATAS

The improved modelling of the tip-loss factor, the models for rotational augmentation, and for the reduction in aerodynamic coefficients near the blade tip are implemented in the BEM-based design programs BLADMODE and PHATAS. Although it was not planned within this project, the accuracy of the blade bending model in PHATAS has also been improved. These improvements lead to a far better agreement of the calculated loads with the 'NASA-Ames measurements'.

Aerodynamic analysis tools *inflow* and *beminf*

In addition to the recommendations for the follow-up work within the IEA annex-XX project, the analysis tool *inflow* has been developed to solve the angle-of-attack distribution from the measured sectional blade loads. With regard to the work within the IEA annex-XX project and similar work within the MEXICO project, serious attention was paid to the validation of this analysis tool *inflow*, which is based on a vortex-description of the wake. Also for the purpose of validation, a similar but simpler analysis tool *beminf* was developed based on the BEM equations. The differences between those tools are relatively small.